REPORT DOCUMENTATION PAGE

Form Approved OMB NO. 0704-0188

1. REPORT DATE (DD-MM-YYYY)	2. REPORT TYPE	3. DATES COVERED (From - To)
10-03-2015	Final Report	15-Jun-2011 - 14-Jun-2014

4. TITLE AND SUBTITLE
Final Report: Participation in CAPPS/IUCRC

5a. CONTRACT NUMBER
W911NF-11-2-0047

5b. GRANT NUMBER

5c. PROGRAM ELEMENT NUMBER
633001

6. AUTHORS
Steven J. Schwartz

5d. PROJECT NUMBER

5e. TASK NUMBER

5f. WORK UNIT NUMBER

7. PERFORMING ORGANIZATION NAMES AND ADDRESSES
Ohio State University
1960 Kenny Road

Columbus, OH 43210 -1016

8. PERFORMING ORGANIZATION REPORT NUMBER

9. SPONSORING/MONITORING AGENCY NAME(S) AND ADDRESS (ES)
U.S. Army Research Office
P.O. Box 12211
Research Triangle Park, NC 27709-2211

10. SPONSOR/MONITOR'S ACRONYM(S)
ARO

11. SPONSOR/MONITOR'S REPORT NUMBER(S)
60060-LS.18

12. DISTRIBUTION AVAILIBILITY STATEMENT
Approved for Public Release; Distribution Unlimited

13. SUPPLEMENTARY NOTES
The views, opinions and/or findings contained in this report are those of the author(s) and should not contrued as an official Department of the Army position, policy or decision, unless so designated by other documentation.

14. ABSTRACT
This project involved an Industry/University Cooperative Research Center consortium between The Ohio State University, the University of California, Davis, and North Carolina State University to assist in advancing food processing and packaging technology and will greatly benefit the US food industry and military personnel. This industry driven consortia center, CAPPS - Center for Advanced Processing and Packaging Studies, focuses on industrial relevant research directed toward coupling microbial life sciences with process and package engineering.

15. SUBJECT TERMS
Participation in CAPPS/IUCRC

16. SECURITY CLASSIFICATION OF:			17. LIMITATION OF ABSTRACT	15. NUMBER OF PAGES	19a. NAME OF RESPONSIBLE PERSON
a. REPORT	b. ABSTRACT	c. THIS PAGE			Steven Schwartz
UU	UU	UU	UU		19b. TELEPHONE NUMBER: 614-292-2934

Report Title

Final Report: Participation in CAPPS/IUCRC

ABSTRACT

This project involved an Industry/University Cooperative Research Center consortium between The Ohio State University, the University of California, Davis, and North Carolina State University to assist in advancing food processing and packaging technology and will greatly benefit the US food industry and military personnel. This industry driven consortia center, CAPPS - Center for Advanced Processing and Packaging Studies, focuses on industrial relevant research directed toward coupling microbial life sciences with process and package engineering.

Enter List of papers submitted or published that acknowledge ARO support from the start of the project to the date of this printing. List the papers, including journal references, in the following categories:

(a) Papers published in peer-reviewed journals (N/A for none)

Received		Paper
03/08/2015	17.00	Rohan V. Tikekar, Mateo Hernandez, Donald P. Land, N. Nitin. “Click chemistry” based conjugation of lipophilic curcumin to hydrophilic ?-polylysine for enhanced functionality, Food Research International, (11 2013): 0. doi: 10.1016/j.foodres.2013.06.004
08/21/2012	6.00	Rohan V. Tikekar, N. Nitin. Effect of physical state (solid vs. liquid) of lipid core on the rate of transport of oxygen and free radicals in solid lipid nanoparticles and emulsion, Soft Matter, (07 2011): 8149. doi: 10.1039/c1sm05031a
08/21/2012	5.00	Juming Tang, V.M. Balasubramaniam, Rockendra Gupta, Galina Mikhaylenko. Combined pressure–temperature effects on the chemical marker (4-hydroxy-5-methyl- 3(2H)-furanone) formation in whey protein gels, LWT Food Science and Technology, (12 2011): 2141. doi: 10.1016/j.lwt.2011.05.007
08/21/2012	1.00	Gulsun Akdemir Evrendilek, V.M. Balasubramaniam. Inactivation of Listeria monocytogenes and Listeria innocua in yogurt drink applying combination of high pressure processing and mint essential oils, Food control, (08 2011): 1435. doi: 10.1016/j.foodcont.2011.03.005
08/21/2012	4.00	S de Lamo-Castellví, W Ratphitagsanti, VM Balasubramaniam, AE Yousef. Inactivation of Bacillus amyloliquefaciens spores by a combination of sucrose laurate and pressure-assisted thermal processing, Journal of Food Protection, (11 2010): 2043. doi:
08/21/2012	7.00	Rohan V. Tikekar, N. Nitin. Distribution of Encapsulated Materials in Colloidal Particles and Its Impact on Oxidative Stability of Encapsulated Materials, Langmuir, (06 2012): 9233. doi: 10.1021/la301435k
09/23/2013	16.00	Alyson E. Mitchell, Jihyun Lee. Pharmacokinetics of Quercetin Absorption from Apples and Onions in Healthy Humans, Journal of Agricultural and Food Chemistry, (04 2012): 0. doi: 10.1021/jf3001857
09/23/2013	13.00	Jihyun Lee, Susan E. Ebeler, Jerry A. Zweigenbaum, Alyson E. Mitchell. UHPLC-(ESI)QTOF MS/MS Profiling of Quercetin Metabolites in Human Plasma Postconsumption of Applesauce Enriched with Apple Peel and Onion, Journal of Agricultural and Food Chemistry, (08 2012): 0. doi: 10.1021/jf302637t
09/23/2013	14.00	Sung Hee Park, V.M. Balasubramaniam, Sudhir K. Sastry, Jiyoung Lee. Pressure–ohmic–thermal sterilization: A feasible approach for the inactivation of Bacillus amyloliquefaciens and Geobacillus stearothermophilus spores, Innovative Food Science & Emerging Technologies, (07 2013): 0. doi: 10.1016/j.ifset.2013.03.005
09/23/2013	15.00	Eunyoung Park, Chang Soo Lee, Wannasawat Ratphitagsanti, R.-Y. Amos Wu, Jiyoung Lee. High-throughput detection of spore contamination in food packages and food powders using tiered approach of ATP bioluminescence and real-time PCR, LWT - Food Science and Technology, (04 2012): 0. doi: 10.1016/j.lwt.2011.09.003

TOTAL: 10

Number of Papers published in peer-reviewed journals:

(b) Papers published in non-peer-reviewed journals (N/A for none)

Received Paper

TOTAL:

Number of Papers published in non peer-reviewed journals:

(c) Presentations

Dr. Katrina Cornish - Assessment and improvement of the physico-chemical properties of bio-based composites for food packaging

Dr. Katrina Cornish Production, assessment and improvement of bio-derived and bio-degradable blown films for food packaging application

Jane Caldwell - Mitochondrial DNA as molecular indicators of thermal processing efficacy

Dr. Bala Balasubramaniam Impact of pressure based alternative technologies on nutrient stability of model liquid beverage systems

Dr. Chris Simons Improving hedonic assessment data using immersive technologies

Dr. Josip Simunovic Acoustically and mechanically enhanced cooling presentation

Dr. Farnaz Maleky Structured lipids with improved barrier characteristics

Dr. N. Nitin Engineering release of encapsulated materials

Drs. Balasubramaniam/Sandeep Development of a superior high pressure processing fluid

Dr. Mary Ann Lila Binding health protective, immune-enhancing bioactive compounds from fruits and vegetables in a shelf stable food ingredient for combat rations.

Number of Presentations: 10.00

Non Peer-Reviewed Conference Proceeding publications (other than abstracts):

Received Paper

TOTAL:

Number of Non Peer-Reviewed Conference Proceeding publications (other than abstracts):

Peer-Reviewed Conference Proceeding publications (other than abstracts):

Received Paper

TOTAL:

Number of Peer-Reviewed Conference Proceeding publications (other than abstracts):

(d) Manuscripts

Received Paper

TOTAL:

Number of Manuscripts:

Books

Received		Book
09/23/2013	2.00	H.Q. Zhang, G. Barbosa-Canovas, V.M. Balasubramaniam, P. Dunne, D. Farkas, J. Yuan. Handbook of Nonthermal Processing Technologies for Food, Chicago: IFT Press, Wiley-Blackwell Publishing, (2011)
09/23/2013	3.00	Rockendra Gupta, V.M. Balasubramaniam. High Pressure Processing of Fluid Foods, in Novel and Non-thermal Technologies for Fluid Foods, San Diego, CA: Elsevier, (2011)
09/23/2013	12.00	Graves RH, Szemplenski T, David JRD. The handbook of aseptic processing and packaging, Boca Raton, FL: CRC Press, (02 2013)

TOTAL: **3**

Received	Book Chapter

TOTAL:

Patents Submitted

Patents Awarded

Awards

Graduate Students

NAME	PERCENT_SUPPORTED	Discipline
Sunny Modi	0.50	
Melissa Limbaugh	0.50	
Ron Bancuyo	0.50	
Bing Yan	0.50	
Elizabeth Horton	0.50	
Kaitlyn Casulli	0.50	
Santosh Dhakal	0.50	
FTE Equivalent:	**3.50**	
Total Number:	**7**	

Names of Post Doctorates

NAME	PERCENT_SUPPORTED
Sunghee Park	1.00
Wyatt Musnick	1.00
FTE Equivalent:	**2.00**
Total Number:	**2**

Names of Faculty Supported

NAME	PERCENT_SUPPORTED	National Academy Member
Steven Schwartz	0.10	No
FTE Equivalent:	**0.10**	
Total Number:	**1**	

Names of Under Graduate students supported

NAME	PERCENT_SUPPORTED
FTE Equivalent:	
Total Number:	

Student Metrics

This section only applies to graduating undergraduates supported by this agreement in this reporting period

The number of undergraduates funded by this agreement who graduated during this period:	5.00
The number of undergraduates funded by this agreement who graduated during this period with a degree in science, mathematics, engineering, or technology fields:.....	0.00
The number of undergraduates funded by your agreement who graduated during this period and will continue to pursue a graduate or Ph.D. degree in science, mathematics, engineering, or technology fields:.....	1.00
Number of graduating undergraduates who achieved a 3.5 GPA to 4.0 (4.0 max scale):.....	0.00
Number of graduating undergraduates funded by a DoD funded Center of Excellence grant for Education, Research and Engineering:.....	0.00
The number of undergraduates funded by your agreement who graduated during this period and intend to work for the Department of Defense	0.00
The number of undergraduates funded by your agreement who graduated during this period and will receive scholarships or fellowships for further studies in science, mathematics, engineering or technology fields:	0.00

Names of Personnel receiving masters degrees

NAME
Total Number:

Names of personnel receiving PHDs

NAME	
Jessica Cooperstone	
Total Number:	**1**

Names of other research staff

NAME	PERCENT_SUPPORTED
Ken Riedl	0.05
FTE Equivalent:	**0.05**
Total Number:	**1**

Sub Contractors (DD882)

Inventions (DD882)

Scientific Progress

Technology Transfer

A Final report submitted to

Center for Advanced Processing and Packaging Studied (CAAPS)

By

N. Nitin, Ph.D.

University of California- Davis

Enhanced Antioxidant Properties of Interface and Reduced Mobility of Encapsulated Lipid Carriers to Limit Oxidation of Encapsulated Products in Emulsions and Particles

April 17th, 2013

This final report is divided into four sub-objectives. The results of these sub-objectives are summarized below:

Objective I: Evaluate the influence of lipid core design in influencing oxidation of encapsulated products

Key Results:

(a) Nanostructured lipid carriers with a mix of solid and liquid lipids is significantly more effective than solid lipid particles in limiting oxidation reactions
(b) Nanostructured lipid carriers can limit the exclusion of encapsulated materials in SLNs
(c) The composition of NLCs with 10% liquid lipid fraction provided the optimal reduction in radical permeation rates and improved the stability of bioactives
(d) The results of this study also highlight the potential impact of lipid core design on release of materials

Objective II: Evaluate the influence of localized antioxidants and physical properties of the interface in limiting transport of free radicals

Key Results:

(a) Physical state of the emulsifier has significant influence on permeation of free radicals
(b) Localization of antioxidants at the interface is significantly more effective than their presence in the bulk phase
(c) Combination of engineering physical properties and controlling localization of antioxidants can be an effective approach to limit oxidation processes

Overall, these findings complement based on engineering interface complements the results of our previous report focused on engineering lipid core of the particles.

Objective III: Role of Antioxidant activity of emulsifiers to improve oxidative stability of encapsulated bioactives

Key Results:

(a) Selection of emulsifiers with antioxidant properties is an effective approach to improve oxidative stability of encapsulated bioactives
(b) This approach may have significant cost benefits as compared to exogenous addition of antioxidants

(c) This approach also indicates that localization of antioxidants at the interface is also an effective approach as it increases the localized concentration of the antioxidant

Objective IV: Role of protein core design in influencing oxidation of encapsulated bioactives.

Key Results:

(a) Zein particles provide a significantly improved barrier to oxidation as compared to emulsions
(b) The rate of oxygen diffusion in zein particles is not significantly higher than the emulsion core itself, indicating the porosity of the protein core was sufficient for oxygen diffusion
(c) The rate of radical permeation in zein particles was significantly slower than the emulsion lipid core

Objective I: Evaluate the influence of lipid core design in influencing oxidation of encapsulated products

Key Results:

(e) Nanostructured lipid carriers with a mix of solid and liquid lipids is significantly more effective than solid lipid particles in limiting oxidation reactions
(f) Nanostructured lipid carriers can limit the exclusion of encapsulated materials in SLNs
(g) The composition of NLCs with 10% liquid lipid fraction provided the optimal reduction in radical permeation rates and improved the stability of bioactives
(h) The results of this study also highlight the potential impact of lipid core design on release of materials

Overall, these findings complement based on engineering interface complements the results of our previous report focused on engineering lipid core of the particles.

DETAILED REPORT:

INTRODUCTION

Solid lipid nanoparticles (SLNs) and nanostructured lipid carriers (NLCs) are lipid based encapsulation and delivery systems. SLNs are prepared using a single lipid component, while NLCs are prepared using a blend of solid and liquid lipids[1]. The unique advantages of SLN and NLCs based formulations are: (a) ability to encapsulate a range of hydrophobic bioactive agents; (b) relative ease of scale up of encapsulation process from a laboratory to an industrial scale; (c) biocompatibility and (d) no use of hazardous and toxic organic solvents during synthesis [2-4]. Based on these distinct advantages, SLN and NLC formulations are commonly used in pharmaceutical, food and cosmetic industries.

Successful development and application of encapsulation technologies requires: (a) high encapsulation efficiency; (b) desired release profile over a target period of time; and (c) oxidative stability of encapsulated materials[3-5]. In previous studies, SLNs and NLCs have been evaluated and compared based on encapsulation efficiency; [6-8] and release profile[9-12]. The results of these studies highlight significant differences in the encapsulation efficiency and the rate of release of encapsulated materials from SLNs and NLCs. These differences in the release rate and the encapsulation efficiency are attributed to the differences in intra-particle

distribution of encapsulated material between SLNs and NLCs [1, 4, 8, 13, 14]. To evaluate this difference in intra-particle distribution, prior studies [15-18] have used spectroscopy methods (NMR, ESR etc.). The results of these studies suggest that extensive "exclusion" of encapsulated material occurred in SLNs as compared to NLCs. Additionally these studies indicated that the encapsulant was present in distinct liquid lipid rich domain, while the solid lipid contained little or no encapsulated material. Currently, there is a lack of direct visualization of differences in the intra-particle distribution of encapsulated materials between SLNs and NLCs. This direct visualization approach can complement the spectroscopy based measurements in characterizing the heterogeneous distribution of encapsulated material in colloidal lipid particles.

Oxidative stability of a selected material in encapsulating matrix is a critical factor for an optimal design of encapsulation process for food, pharmaceutical and cosmetic industries. Despite significant applications of SLNs and NLCs in these diverse industries, there is no study to the best of our understanding that directly compares the distribution of encapsulated materials in SLNs and NLCs and its influence on oxidative stability of encapsulated material. Free radicals such as hydroxyl, peroxyl and superoxide radicals trigger oxidation of encapsulated materials[19-21]. Prior studies show that these radicals are generated either in the aqueous phase or at the oil-water interface due to presence of various initiators such as metal ions, light and oxygen [22, 23]. These free radicals transport across the oil-water interface and into the lipid phase where they trigger oxidative reactions with encapsulated materials. These oxidation processes are propagated by subsequent generation of chain of free radicals in the presence of oxygen. The physical state of lipid core material and localization of encapsulated material within the core region can significantly influence the rate of these oxidation reactions[24, 25] by limiting the interactions of encapsulated material with free radicals and oxygen.

Thus, the overall objectives of the present study were- (a) direct visualization and quantitative characterization of intra-particle distribution of encapsulated material in SLNs and NLCs and (b) evaluate the influence of intra-particle distribution of encapsulated material on its relative susceptibility to oxidation in SLNs and NLCs. For fluorescence imaging measurements, a lipid soluble fluorescent dye (nile red) was used as a model encapsulant. Distribution of encapsulated material was characterized using a combination of wide-field and confocal fluorescence imaging. Susceptibility of encapsulant in SLNs and NLCs to oxidation reactions was directly and independently measured based on its reaction with (a) free radicals (peroxyl radical) generated in the aqueous phase and (b) atmospheric oxygen dissolved in the aqueous phase. To accomplish this, changes in the fluorescence of oxygen and peroxyl radical sensitive

dyes encapsulated in the lipid phase of these particles upon interaction with oxygen and free radicals were measured[26, 27]. Direct measurement of susceptibility of encapsulant to free radicals and oxygen has a unique advantage as these measurements provide a quantitative assessment of the barrier properties of the encapsulating lipid matrix. These quantitative measurements are independent of the differences in susceptibility of various bioactive compounds to either oxygen or free radicals. Overall, this study illustrates a comprehensive approach to evaluate the influence of distribution of encapsulated material within colloidal particles on its oxidative stability.

MATERIALS AND METHODS

Chemicals

Eicosane, glyceryl trioctanoate (GT), bile salts, nile red, sodium azide, 2,2'-azobis-2-methyl-propanimidamide dihydrochloride (AAPH) were obtained from Sigma Aldrich (Saint Louis, MO). High melting lecithin (Phospholipon® 80 H) was a gift from American Lecithin Inc (Oxford, CT). Nile red was used as a model lipid soluble encapsulant for imaging measurements. To measure the susceptibility towards peroxyl radicals, BODIPY® 665/676 dye (Invitrogen Inc., Carlsbad, CA) with $\lambda_{excitation}$= 620 nm and $\lambda_{emission}$=675 nm was selected. The dye has high specificity to react with peroxyl radicals and shows a decrease in fluorescence intensity upon reaction with peroxyl radicals. Oxygen sensitive fluorescent dye tris (4,7-diphenyl-1,10-phenanthroline) ruthenium bis (hexafluorophosphate) complex (Santa Cruz Biotechnology Inc., Santa Cruz, CA) with $\lambda_{excitation}$=455 nm and $\lambda_{emission}$=615 nm was used for characterization of diffusion of dissolved oxygen from the aqueous phase to lipid phase of SLN and NLCs . The oxygen sensitive dye shows a maximum fluorescence in the absence of oxygen, and the fluorescence intensity of the dye decreases with an increase in oxygen concentration.

SLN and NLC preparation for imaging

Fluorescence imaging was conducted to characterize the distribution of encapsulated nile red within lipid matrix of both SLNs and NLCs. The emulsion droplets generated using homogenization process were significantly smaller ($d_{0.5}$ ~ 110-200 nm) than the resolution of fluorescence microscopy. Additionally, it was difficult to visualize and measure the distribution of the dye in such small particles based on their fluorescence intensity. To overcome these limitations, coarse SLN and NLC particles were prepared for imaging purposes. Aqueous phase was prepared by dissolving high melting lecithin (HML) (1% w/v of aqueous phase) and bile salt

(0.5% w/v of aqueous phase) in ultrapure water. Total lipid content was set at 5% (w/v) of aqueous phase. For SLNs, lipid phase consisted of 100% eicosane. In 1% NLC, lipid phase consisted of 99% eicosane and 1% GT, while in 10% NLC, lipid phase consisted of 90% eicosane and 10% GT. The lipid phase was heated up to 70 ºC to ensure complete melting of eicosane. Nile red dye was mixed with the lipid phase at a concentration of 12 µg/g of lipid phase. The aqueous phase was also heated up to at least 70 °C to prevent solidification of eicosane during emulsification. The coarse particles were prepared by mixing aqueous and lipid phase using a hand-held disperser (Ultra-Turrax model T25, IKA Works, Wilmington, NC) set at 9000 rpm for 2 minutes. Immediately after mixing, the SLN and NLC suspensions were diluted 2-3 times with ultrapure water and approximately 50 µL of the sample volume was mounted on the glass slide. The glass slide was then covered with a cover slip and immediately placed in a 4 ºC chamber for 30 minutes to ensure adequate cooling and solidification of eicosane in the particles. After 30 minutes of storage, the samples were imaged using either a wide-field microscope or a laser scanning confocal microscope.

SLN and NLC preparation for measurement of oxidative stability of encapsulated material

In contrast to imaging experiments where micron (10-20 µm) size particles were prepared, nanometer ($d_{0.5}$ ~ 110-200 nm) size SLN and NLC particles were prepared for measuring oxidative stability of encapsulated material. This was done to achieve extended stability of colloidal particles during the course of measurements (~15 hours). Fine SLN and NLC samples were prepared using the identical composition as used for imaging experiments, except for the use of nile red. In these samples, nile red was substituted by either oxygen sensitive dye (~10 µg/g lipid phase prepared in chloroform) or peroxyl radical sensitive dye (~3 µg/g lipid phase prepared in chloroform). The coarse particles were prepared by mixing aqueous and lipid phase using a hand-held disperser (Ultra-Turrax model T25, IKA Works, Wilmington, NC) set at 9000 rpm for 2 minutes. The premix was subsequently passed five times through a single stage homogenizer operating at 800 bar to generate sub-micron lipid droplets. The samples were added with 0.05% sodium azide and stored at 4 ºC for 12 hours to enable solidification of eicosane in SLNs or NLCs.

Particle size measurement

The hydrodynamic sizes of SLN and NLC particles were measured using a particle size analyzer (Model: Microtrac 3500, Montgomeryville, PA). The settings for the analyzer were- flow rate 50%, run-time 30 s, particle refractive index=1.15, type of particle: transparent, shape of

particle: irregular. The data were analyzed using a number based average of individual particle diameter.

Differential scanning calorimetry (DSC)

DSC (Model: Pyris 1, Perkin Elmer, Waltham MA) was performed to identify the melting and solidification temperatures of eicosane in SLNs and NLCs. Approximately 5 mg of sample was weighed and placed in an aluminum pan for DSC measurements. An empty aluminum pan was used as a control in this experiment. The sample was heated from 25 °C to 50 °C and then cooled to 2 °C at the rate of 5 °C /min. This process was repeated twice to ensure consistency in measurements of melting and solidification temperatures.

Fluorescence imaging and imaging data analysis

Confocal microscopy was conducted using a Zeiss LSM 510 Meta confocal microscope. Confocal images of SLN and NLC particles were obtained using a 63x oil objective with a numerical aperture of 1.4. The samples encapsulating nile red dye (as described above) were imaged using a 543 nm laser excitation. The fluorescence emission signal was collected using a long pass 560 nm filter. To characterize the distribution of encapsulated dye in SLNs and NLCs, the samples were optically sectioned using a z-scanning mode. The z- scans of samples were acquired with a z-spacing of 1.0 μm. The 3-d reconstruction of images was performed using a 'montage' function in Metamorph® image processing software (Molecular devices Inc., Carlsbad, CA).

Fluorescence intensity profile along the diameter of representative particles was plotted using the 'intensity profile' function in ImageJ (National Institutes of Health, Bathesda, MD). The 'intensity profile' function measures the fluorescence intensity along the line drawn on the object. The fluorescence intensity was converted to the relative fluorescence intensity using Eq. (1)-

$$\textit{Relative fluorescence intensity} = \frac{\textit{Fluorescence intensity at a point on the line}}{\textit{maximum fluorescence intensity along that line}} \quad (1)$$

In order to measure – (a) the extent of localization of dye and (b) reduction in exclusion of dye into aqueous phase, the ratio of maximum fluorescence intensity in the particle to the background fluorescence intensity in the aqueous phase was also calculated. This ratio is based on the assumption that the fluorescence intensity within a pixel is directly proportional to the amount of dye present in that region. The background fluorescence indicates the amount of dye that is excluded out from the lipid particles into the aqueous phase.

In order to illustrate differences in the distribution pattern of encapsulated dyes in NLC particles, fluorescence intensity distribution across the image plane (2-d distribution) of individual particles was also quantified for 1% NLC and 10% NLC particles. This quantification was accomplished using the 'histogram' function in the ImageJ software which provided the number of pixels in a given particle with a particular value of fluorescence intensity (intensity range was 0-85 relative units). The absolute number of pixels was converted into the percentage of total pixels at a particular intensity by using Eq. (2)-

$$\%\ \boldsymbol{particles\ with\ fluorescence\ intensity\ x} = \frac{\boldsymbol{A}}{\boldsymbol{T}} \qquad (\mathbf{2})$$

Where, **A=** Number of particles with intensity x and **T=** total number of pixels

The intensity values were grouped together as 1-20, 21-40, 41-60 and 61-85 relative units and the percentage of total pixel numbers within each group of relative intensity values were calculated to obtain a histogram.

Confocal imaging measurements and data analysis was complemented by wide field fluorescence imaging measurements. The experimental details for the wide-field fluorescence microscopy are described in the supporting supplementary information.

Measurement of susceptibility of encapsulated material to peroxyl radical

Peroxyl radicals were generated in the aqueous phase of SLNs and NLCs using AAPH. 40 mM AAPH was dissolved in ultrapure water. 1 mL of SLN or NLC sample was then mixed with 1 mL of AAPH solution to achieve a final concentration of 20 mM AAPH. Immediately after addition of AAPH, the samples were placed in the plate-reader (Spectramax M5, Molecular Devices, Carlsbad CA) and fluorescence intensity was measured at a regular time interval of 20 minutes for a total time period of 13 hours. SLN and NLC samples mixed with equal volume of ultrapure water were used as controls. The excitation and emission wavelengths for fluorescence measurements were 620 nm and 675 nm respectively. The relative fluorescence intensity was calculated using Eq. (3)-

$$\boldsymbol{Relative\ fluorescence\ intensity} = \frac{\frac{\boldsymbol{I_{t\ AAPH}}}{\boldsymbol{I_{0\ AAPH}}}}{\frac{\boldsymbol{I_{t\ control}}}{\boldsymbol{I_{0\ control}}}} \times \mathbf{100} \qquad (\mathbf{3})$$

Where, $I_{t\ AAPH}$= Fluorescence intensity of sample after 't' minutes of exposure to AAPH, $I_{0\ AAPH}$= Fluorescence intensity of sample immediately after addition of AAPH, $I_{t\ control}$= Fluorescence intensity of control sample after time 't' minutes, $I_{0\ control}$= Fluorescence intensity of control sample at time t=0 minute. The data was normalized with respect to the relative fluorescence of control samples in order to account for changes in fluorescence intensity induced by evaporation during the course of measurement (~15 hours).

Measurement of susceptibility of encapsulated material to oxygen

After homogenization, SLNs and NLC samples were transferred to three aluminum foil wrapped plastic bottles (5 mL each) and purged with nitrogen for three hours to remove traces of air. Efficient removal of oxygen provides a large dynamic range to measure changes in fluorescence upon exposure to oxygen. After purging, the samples were exposed to atmosphere by pipetting 200 µL of sample/well in a 96 well black costar plate optimized for fluorescence measurement. SLN and NLC samples were exposed to ambient air within a plate reader. Loss in fluorescence intensity as a result of exposure to atmospheric oxygen was measured using a plate-reader (Model: M5, Molecular Devices, Carlsbad CA). The excitation and emission settings for the plate- reader were 485 nm and 615 nm respectively. The plate-reader was set at 23 °C for both SLNs and NLC samples. Changes in fluorescence intensity as a function of time were recorded at a regular interval of 15 s for 10 minutes. The relative fluorescence intensity was calculated using the following equation-

$$\mathit{Relative\ fluorescence\ intensity} = \frac{(I_t - I_\infty)}{(I_0 - I_\infty)} \times 100 \qquad (4)$$

Where, I_t= Fluorescence intensity at time 't' s after exposure to atmospheric oxygen I_∞= Fluorescence intensity at equilibrium oxygen concentration, I_0= Fluorescence intensity in the absence of oxygen (nitrogen purged sample at t= 0 s)

RESULTS AND DISCUSSION

Particle size distribution

Particle size distribution of SLNs and NLCs encapsulating radical and oxygen sensitive dye was measured using dynamic light scattering (DLS). Particle size distribution was characterized based on the average particle size ($d_{0.5}$) and the particle size corresponding to 90th percentile ($d_{0.9}$) of total particles. Based on these measurements, the particle size distribution of SLN, 1% NLC and 10% NLCs containing BODIPY 665/676 dye (peroxyl radical

sensitive dye) were: $d_{0.5}$ =115 nm, $d_{0.9}$=179 nm; $d_{0.5}$=210 nm, $d_{0.9}$= 277 nm; and $d_{0.5}$ =111nm, $d_{0.9}$=179 nm respectively. These results clearly illustrate that both SLNs and NLCs encapsulated with peroxyl radical sensitive dye had similar particle size distribution. Incubation with 20 mM AAPH (peroxy radical generator) marginally increased the average particle size across all the samples. Nevertheless, more than 90% of the SLNs and NLC particles were less than 400 nm in size, suggesting no significant aggregation and flocculation of particles was induced by approximately 15 hours of AAPH treatment. Particle size distribution of SLN and NLC particles containing ruthenium based oxygen sensitive dye was also measured using DLS. Based on these measurements, the particle size distribution of SLNs and 1% NLC and 10% NLC were $d_{0.5}$ = 143 nm, $d_{0.9}$=233 nm; $d_{0.5}$ = 122 nm, $d_{0.9}$=195 nm; and $d_{0.5}$ = 109 nm; $d_{0.9}$=165 nm respectively. Overall, these particle size measurements clearly demonstrate that both SLNs and NLCs had similar particle size distribution.

Differential scanning calorimetry (DSC) for SLNs and NLCs

Differential scanning calorimetry (DSC) was used for thermodynamic characterization of melting and solidification temperatures and measurement of enthalpy of phase change in SLN and NLC particles. **Figures 1a and 1b** show the melting and the solidification curves for SLN, 1% NLC and 10% NLC. These results demonstrate that: (a) solid lipid fraction was present in both SLN and NLC (1 and 10% GT) formulations, (b) the fraction of solid eicosane decreased with an increase in percentage of GT fraction (liquid lipid); and (c) emulsified eicosane showed a significant super-cooling in both SLN and NLC formulations. This is evident from the fact that emulsified eicosane melted at 35-37 ^{o}C while it solidified between 18-20 ^{o}C. Super-cooling of emulsified alkanes is a known phenomenon and is attributed to homogenous nucleation mechanism[28]. DSC scan performed on 100% GT emulsion did not show melting or solidification peaks indicating that the emulsified GT remains in the liquid state between the temperature range of 2-50 ºC (data not shown).

Table 1 shows the average initiation and termination temperatures for melting and solidification of eicosane in SLNs, 1% NLC and 10% NLC. These results show that the melting point of solid lipid particles decreased with the addition of liquid lipid fraction in NLCs. It also suggests broadening of the melting peak with the addition of liquid lipid fraction in NLCs. These results are consistent with the results from previous studies where similar trends in the melting curves of NLCs were observed [9, 29].

Based on DSC measurements, the latent heat of melting for emulsified lipids in SLNs, 1% NLCs, 10% NLCs was calculated by integrating area under the melting curve of the thermogram. The average values for latent heat of melting for SLN, 1% NLC and 10% NLC were 134.78, 121.1, 80.2 J/g respectively. Based on the ratio of the latent heat of melting of NLCs with respect to SLNs, the relative liquid lipid fraction in NLCs was calculated. The results show that 1% NLC contained approximately 11% liquid lipid fraction, while 10% NLCs contained approximately 40% liquid lipid fraction. Similar values (10.2 and 27% for 1% and 10% NLC respectively) of liquid lipid fraction were obtained based on the latent heat of solidification. These results are in agreement with an earlier study that has demonstrated a non-linear decrease in the latent heat of solidification with an increase in liquid lipid fraction in NLCs [17].

Visualization of encapsulated material (nile red) in SLNs and NLCs

Due to differences in compositions of SLN and NLC particles, the spatial distribution of encapsulated material in SLN and NLC cores is expected to be significantly different [16, 30]. These differences in distribution of encapsulated material in SLN and NLCs can impact the oxidative stability of encapsulated products. In this study, direct visualization approach based on a combination of wide-field fluorescence and confocal microscopy was used for characterization of distribution of the encapsulated nile red dye.

SLNs

Figures 2a and **2b** show fluorescence and fluorescence-DIC overlaid images of individual confocal sections of SLNs with a z-spacing of 1 μm and a fluorescence intensity profile across the diameter of a representative SLN particle respectively. **Figure 2c** shows confocal sections of a single SLN particle (magnified view) obtained at a z-scale interval of 1 μm. Confocal images (**Figure 2a** and **Figure 2c**) show a significant exclusion of the encapsulated dye from the core of SLN particles. **Figure 2b** shows that the fluorescence intensity at the center of the lipid droplet was indeed lower than the average background fluorescence intensity ($p<0.05$), further confirming the exclusion of nile red into the aqueous phase. These results are consistent with results obtained using wide-field fluorescence imaging (discussed in supplemental information section). In our earlier study, we have demonstrated a similar exclusion of another dye, BODIPY 665/676 that has a significantly different chemical structure than the nile red dye [31]. We also observed exclusion of nile red from SLNs prepared using Trilaurin- a lipid previously used for synthesis of SLNs[3]. These results suggest that the phenomenon of exclusion is not restricted to nile red-eicosane system.

To further characterize SLN particles, X-ray diffractograms of pure eicosane, SLN with nile red and SLN without nile red were compared (details are presented in the supplementary section). The results showed that crystallite size of eicosane in SLNs without nile red (22.1 nm) was significantly lower than that in pure eicosane (23.9 nm), suggesting that emulsification process decreased the crystallite size of eicosane. However, crystallite size of eicosane in SLNs containing nile red (21. 8 nm) was only marginally lower than SLNs not containing nile red (22.1 nm). These measurements indicate that the presence of nile red did not significantly affect the crystallization process within SLNs. It is expected that the excluded compound from the eicosane matrix will not have significant influence on the properties of eicosane. These results are in agreement with imaging measurements of SLNs that clearly illustrates exclusion of encapsulated nile red dye.

1% NLC

Confocal imaging results (**Figures 3a** and **3b**) show that nile red dye was predominantly distributed within the core of individual NLC particles. Quantitative analysis based on fluorescence intensity profile across the diameter of a selected particle (**Figure 3b**) shows presence of multiple peaks within the core of NLC particle. This intensity profile of 1% NLCs was significantly different from that of SNLs, where the highest fluorescence intensity was observed at the edges of individual particles. These results indicate that incorporation of small amount of liquid lipid (GT) to solid lipid (eicosane) significantly reduced the exclusion of encapsulated nile red. The ratio of maximum fluorescence intensity within the particle to the background fluorescence was 7.4 in 1% NLCs. This ratio was significantly higher than that in SLNs (2.37) ($p<0.05$), further confirming that 1% NLC was able to reduce the exclusion of nile red dye.

In order to illustrate the distribution of encapsulated dye in NLC particles, a 3-dimensional projection image was reconstructed from individual confocal sections of a single particle (**Figures 3c**). The reconstructed image clearly demonstrates the presence of fluorescent channels within the core of NLC particles surrounded by solid lipid (eicosane) domains with significantly reduced fluorescence intensity. It is important to note that these channels travel across the depth of the particle and up to the surface of the droplets.

10% NLC

Confocal measurements (**Figures 4a** and **4b**) show that nile red dye was predominantly distributed within the core of individual NLC particles. The ratio of maximum fluorescence intensity to background fluorescence was 13.14. Based on the statistical analysis, this ratio was significantly higher than both 1% NLC (7.4) and SLNs (2.37) suggesting that the dye was concentrated at discrete locations within the core of 10% NLC particles.

In order to illustrate the distribution of encapsulated dye in 10% NLC particles, 3-dimensional projection image was reconstructed from individual confocal sections (**Figures 4c**). **Figure 4c** demonstrates that the nile red dye was localized in the core as a continuous region that was partially encapsulated by solid lipid fraction. This is in contrast to 1% NLC where the dye was located within multiple 'channels' surrounded by solid lipids. In order to further quantify the differences in the distribution of nile red between 1% NLC and 10% NLCs, histograms of fluorescence intensity profiles within 1% and 10% NLC particles were quantified as shown in **Figure 5.** These quantitative results show that 1% NLC particles contained a significantly higher percentage (83.6%) of pixels with fluorescence intensity of < 20 relative units as compared to that in 10% NLC (66.7%) ($p < 0.05$). On the other hand, 10% NLC particles contained a significantly higher proportion of pixels (7.8%) with fluorescence intensity of 60-85 relative units (highest intensity level in these images) as compared to 1% NLC (0.14%). Assuming that both 1% and 10% NLC particles have similar encapsulation efficiency, the higher fraction of pixels at lower fluorescence intensity (<20) in 1% NLC suggests that the fluorescent dye was distributed over a larger surface area in 1% NLC as compared to 10% NLC. Furthermore, a higher proportion of pixels in the high intensity region (60-85) for 10% NLC as compared to 1% NLC suggest that the dye was localized within the concentrated regions in 10% NLC as compared to 1% NLC. Combined together, these quantitative results derived from imaging measurements show a significant difference in the distribution pattern of encapsulated dye between 1% and 10% NLCs.

Susceptibility of encapsulated materials to oxidation within SLNs and NLCs

Based on the imaging results, we hypothesized that the reduced exclusion of encapsulated material in NLCs as compared to SLNs will result in reduced susceptibility of encapsulated material to react with free radicals and ambient oxygen. Furthermore, based on differences in the distribution of fluorescent dye in 1% and 10% NLCs, we hypothesized that 10% NLC will offer better protection to the encapsulated materials from oxidizing species (free radicals and oxygen) as compared to 1% NLC. To test these hypotheses, susceptibility of

encapsulated materials towards free radicals and oxygen was directly measured using the peroxyl radical and oxygen sensitive fluorescent dye encapsulated in SLNs and NLCs respectively. This approach has been described in detail in the material and methods section and our previous publications[26, 27, 31].

Susceptibility to peroxyl radical

Figure 6 shows the rate of loss of fluorescence of peroxyl radical sensitive dye encapsulated in SLNs and NLCs as a function of time after addition of 20 mM AAPH (a peroxyl radical generator) in the aqueous phase. The relative fluorescence intensity remained at 100% for up to 300 minutes in both SLNs and NLCs. This is consistent with the results of our prior study where we observed a similar shoulder in SLNs and liquid state emulsions [31]. This suggests that the presence of shoulder is independent of the physical state of lipid and depends on the chemical nature of the emulsifier. After 300 minutes, the relative fluorescence intensity decreased in both SLNs and NLCs. However, the rate of decay of relative fluorescence intensity for NLCs was significantly lower than that for SLNs. After 800 minutes of incubation, the % relative fluorescence intensity for SLN, 1% NLC and 10% NLC were 20.13%, 46.13% and 64.33% respectively. Statistical t-test showed that the relative fluorescence intensity in 10% NLC was significantly higher than 1% NLC ($p<0.05$) after 800 minutes of incubation with AAPH. Similarly, the fluorescence intensity for 1% NLC was significantly higher than SLN ($p<0.05$) after 800 minutes of incubation with AAPH. Thus, the relative rate of decay of fluorescence intensity induced by free radicals was SLN> 1% NLC > 10% NLC ($p<0.05$). It is important to note that the eicosane and GT are saturated compounds and cannot participate in propagating free radical based on a chain reaction. Thus, the fluorescence decay of peroxyl radical sensitive was induced by interaction of encapsulated dye with peroxyl radicals transported from the aqueous phase to the lipid phase.

A significant difference in the fluorescence decay rate of peroxyl radical sensitive dye between SLNs and NLCs suggest that fluorescent dye encapsulated within NLCs was less susceptible to oxidation by peroxyl radicals as compared to that in SLNs. In SLNs, the peroxyl radical sensitive dye was predominantly located at the lipid-water interface of SLN particles due to the ‘exclusion’ of encapsulated dye. As a result, the solid lipid core of SLN did not offer any significant barrier to the interaction of peroxyl radicals with the radical sensitive dye. On the contrary, the peroxyl radical sensitive dye in NLCs was located inside the particle with only a small fraction of dye present at the surface. Thus, the effective surface area of exposure of

encapsulated dye in NLCs was significantly smaller than SLNs. Consequently, peroxyl radical sensitive dye was more effectively shielded from peroxyl radicals in NLCs as compared to SLNs.

The difference in the fluorescence decay rate between 1 and 10% NLCs can be explained based on the differences in the relative distribution of encapsulated material in 1 and 10% NLCs. As discussed earlier, the fluorescent dye in 1% NLC was mainly located in channels that run up to the surface of the droplets while in case of 10% NLC the dye was mainly located in continuous 'pool' like regions. Distribution of encapsulated material in small channels (as observed in case of 1% NLC) can provide a large surface area as compared to concentrated localization of encapsulated material (10% NLC). The higher surface area of exposure can significantly increase the rate of reaction between the free radicals and the encapsulated dye.

Susceptibility to oxygen

Oxygen is required for propagation of many of the radical induced oxidation reactions [32]. The aim of this experiment was to evaluate the differences in in the susceptibility of oxygen sensitive dye encapsulated within SLNs and NLCs towards oxygen dissolved in the aqueous phase. Based on differences in the distribution of encapsulated materials between SLNs and NLCs, we hypothesized that the rate of exposure of encapsulated material to oxygen will be lower in NLCs as compared to that in SLNs.

In order to test this hypothesis, SLNs and NLCs were formulated using a lipid soluble oxygen sensitive dye. This oxygen sensitive dye is quenched with an increase in concentration of oxygen and the quenching process can be reversed by reducing the concentration of oxygen. Prior to exposure to atmospheric oxygen, the SLNs and NLCs were purged with nitrogen for an extended period as described in the material and methods section to remove dissolved oxygen. **Figure 7** shows the rate of loss of fluorescence for the oxygen sensitive dye encapsulated in nitrogen purged SLNs and NLCs as a function of time of exposure to atmosphere. Results show that susceptibility of encapsulated dye towards oxygen was not significantly different among SLN, 1% NLC and 10% ($p>0.05$). This suggests that the differences in intra-particle distribution of encapsulated material did not influence the rate of interaction of encapsulated material (oxygen sensitive dye) with oxygen. This can be explained based on the facts that oxygen is a more stable molecule relative to peroxyl radicals and it can efficiently and rapidly diffuse through small imperfection in NLC particles (nanoscale cracks and crevices formed in NLCs, Figures 5c and 7c). Due to relatively high stability of oxygen as compared to reactive radicals, it is not

quenched upon its interaction with materials. These results highlight that simply reducing the surface area of exposure of encapsulated material to oxygen is not sufficient to inhibit the transport of oxygen in NLC particles. This result also indicates that controlling the distribution of encapsulated material such that it is completely encapsulated by solid lipids may be a necessary condition to limit exposure of encapsulated material to oxygen.

CONCLUSIONS

Wide-field and confocal imaging results clearly demonstrate significant differences in the distribution of the encapsulated material (nile red) between SLNs and NLCs. In SLNs, the encapsulated dye was 'excluded' out into aqueous phase due to solidification of lipids. Presence of a small amount of liquid lipid significantly reduced the expulsion of encapsulated dye and re-arranged the dye within the liquid lipid domains surrounded by the solid lipid fraction. The difference in the distribution of encapsulated materials resulted in reduced susceptibility of encapsulated material to peroxyl radicals in NLCs as compared to SLNs. The results also suggest that small imperfections (channels or cracks) at the surface were sufficient to enable rapid transport of oxygen into the core of lipids. Overall, these results suggest that differences in distribution pattern of encapsulated materials within SLNs and NLCs can significantly impact stability of encapsulated material. Further research is needed to investigate the impact of these differences in distribution pattern on release kinetics and digestibility of encapsulants. Research is also needed to evaluate the effect of compositional differences in lipid matrix on exclusion and distribution pattern of encapsulant.

ACKNOWLEDGEMENTS

This research was supported by funding from ACS-PRF (award # 51459-DNI5); NSF-CAPPS and UC-Davis. Authors thank Dr. Zhorro Nikolov and Centralized Research Facilities (CRF) at Drexel University for their assistance with X-ray diffraction experiments. Authors also acknowledge assistance from UC-Davis food science teaching laboratory for fluorescence spectroscopy measurements.

REFERENCES

1. Muller, R. H.; Radtke, M.; Wissing, S. A., Solid lipid nanoparticles (SLN) and nanostructured lipid carriers (NLC) in cosmetic and dermatological preparations. *Advanced Drug Delivery Reviews* **2002,** 54, S131-S155.
2. Mehnert, W.; Mader, K., Solid lipid nanoparticles - Production, characterization and applications. *Advanced Drug Delivery Reviews* **2001,** 47, (2-3), 165-196.
3. zur Muhlen, A.; Schwarz, C.; Mehnert, W., Solid lipid nanoparticles (SLN) for controlled drug delivery - Drug release and release mechanism. *European Journal of Pharmaceutics and Biopharmaceutics* **1998,** 45, (2), 149-155.
4. Wissing, S. A.; Kayser, O.; Muller, R. H., Solid lipid nanoparticles for parenteral drug delivery. *Advanced Drug Delivery Reviews* **2004,** 56, (9), 1257-1272.
5. Muller, R. H., *Introduction*. CRC Press: Boca Raton, FL, 1991.
6. Jenning, V.; Gohla, S., Comparison of wax and glyceride solid lipid nanoparticles (SLN (R)). *International Journal of Pharmaceutics* **2000,** 196, (2), 219-222.
7. Souto, E. B.; Wissing, S. A.; Barbosa, C. M.; Muller, R. H., Development of a controlled release formulation based on SLN and NLC for topical clotrimazole delivery. *International Journal of Pharmaceutics* **2004,** 278, (1), 71-77.
8. Yuan, H.; Wang, L. L.; Du, Y. Z.; You, J.; Hu, F. Q.; Zeng, S., Preparation and characteristics of nanostructured lipid carriers for control-releasing progesterone by melt-emulsification. *Colloids and Surfaces B-Biointerfaces* **2007,** 60, (2), 174-179.
9. Jenning, V.; Thunemann, A. F.; Gohla, S. H., Characterisation of a novel solid lipid nanoparticle carrier system based on binary mixtures of liquid and solid lipids. *International Journal of Pharmaceutics* **2000,** 199, (2), 167-177.
10. Thatipamula, R. P.; Palem, C. R.; Gannu, R.; Mudragada, S.; Yamsani, M. R., Formulation and in vitro characterization of domperidone loaded solid lipid nanoparticles and nanostructured lipid carriers. *Daru-Journal of Pharmaceutical Sciences* **2011,** 19, (1), 23-32.
11. Fang, Y. P.; Lin, Y. K.; Su, Y. H.; Fang, J. Y., Tryptanthrin-Loaded Nanoparticles for Delivery into Cultured Human Breast Cancer Cells, MCF7: the Effects of Solid Lipid/Liquid Lipid Ratios in the Inner Core. *Chemical & Pharmaceutical Bulletin* **2011,** 59, (2), 266-271.
12. Fang, J. Y.; Fang, C. L.; Liu, C. H.; Su, Y. H., Lipid nanoparticles as vehicles for topical psoralen delivery: Solid lipid nanoparticles (SLN) versus nanostructured lipid carriers (NLC). *European Journal of Pharmaceutics and Biopharmaceutics* **2008,** 70, (2), 633-640.
13. Muller, R. H.; Radtke, M.; Wissing, S. A., Nanostructured lipid matrices for improved microencapsulation of drugs. *International Journal of Pharmaceutics* **2002,** 242, (1-2), 121-128.

14. Pardeike, J.; Hommoss, A.; Muller, R. H., Lipid nanoparticles (SLN, NLC) in cosmetic and pharmaceutical dermal products. *International Journal of Pharmaceutics* **2009,** 366, (1-2), 170-184.
15. Jores, K.; Mehnert, W.; Mader, K., Physicochemical investigations on solid lipid nanoparticles and on oil-loaded solid lipid nanoparticles: A nuclear magnetic resonance and electron spin resonance study. *Pharmaceutical Research* **2003,** 20, (8), 1274-1283.
16. Jores, K.; Mehnert, W.; Drechsler, M.; Bunjes, H.; Johann, C.; Mader, K., Investigations on the structure of solid lipid nanoparticles (SLN) and oil-loaded solid lipid nanoparticles by photon correlation spectroscopy, field-flow fractionation and transmission electron microscopy. *Journal of Controlled Release* **2004,** 95, (2), 217-227.
17. Teeranachaideekul, V.; Boonme, P.; Souto, E. B.; Muller, R. H.; Junyaprasert, V. B., Influence of oil content on physicochemical properties and skin distribution of Nile red-loaded NLC. *Journal of Controlled Release* **2008,** 128, (2), 134-141.
18. Jores, K.; Haberland, A.; Wartewig, S.; Mader, K.; Mehnert, W., Solid lipid nanoparticles (SLN) and oil-loaded SLN studied by spectrofluorometry and raman spectroscopy. *Pharmaceutical Research* **2005,** 22, (11), 1887-1897.
19. Mei, L. Y.; McClements, D. J.; Wu, J. N.; Decker, E. A., Iron-catalyzed lipid oxidation in emulsion as affected by surfactant, pH and NaCl. *Food Chemistry* **1998,** 61, (3), 307-312.
20. Cao-Hoang, L.; Fougere, R.; Wache, Y., Increase in stability and change in supramolecular structure of beta-carotene through encapsulation into polylactic acid nanoparticles. *Food Chemistry* **2011,** 124, (1), 42-49.
21. Gonnet, M.; Lethuaut, L.; Boury, F., New trends in encapsulation of liposoluble vitamins. *Journal of Controlled Release* **2010,** 146, (3), 276-290.
22. Mei, L. Y.; Decker, E. A.; McClements, D. J., Evidence of iron association with emulsion droplets and its impact on lipid oxidation. *Journal of Agricultural and Food Chemistry* **1998,** 46, (12), 5072-5077.
23. Ries, D.; Ye, A.; Haisman, D.; Singh, H., Antioxidant properties of caseins and whey proteins in model oil-in-water emulsions. *International Dairy Journal* **2010,** 20, (2), 72-78.
24. Saupe, A.; Gordon, K. C.; Rades, T., Structural investigations on nanoemulsions, solid lipid nanoparticles and nanostructured lipid carriers by cryo-field emission scanning electron microscopy and Raman spectroscopy. *International Journal of Pharmaceutics* **2006,** 314, (1), 56-62.

25. Weiss, J.; Decker, E. A.; McClements, D. J.; Kristbergsson, K.; Helgason, T.; Awad, T., Solid lipid nanoparticles as delivery systems for bioactive food components. *Food Biophysics* **2008,** 3, (2), 146-154.
26. Tikekar, R. V.; Johnson, A.; Nitin, N., Real-time measurement of oxygen transport across an oil-water emulsion interface. *Journal of Food Engineering* **2011,** 103, (1), 14-20.
27. Tikekar, R. V.; Johnson, A.; Nitin, N., Fluorescence imaging and spectroscopy for real-time, in-situ characterization of interactions of free radicals with oil-in-water emulsions. *Food Research International* **2011,** 44, (1), 139-145.
28. Ghosh, S.; Peterson, D. G.; Coupland, J. N., Effects of droplet crystallization and melting on the aroma release properties of a model oil-in-water emulsion. *Journal of Agricultural and Food Chemistry* **2006,** 54, (5), 1829-1837.
29. Hu, F. Q.; Jiang, S. P.; Du, Y. Z.; Yuan, H.; Ye, Y. Q.; Zeng, S., Preparation and characterization of stearic acid nanostructured lipid carriers by solvent diffusion method in an aqueous system. *Colloids and Surfaces B-Biointerfaces* **2005,** 45, (3-4), 167-173.
30. Lin, X. H.; Li, X. W.; Zheng, L. Q.; Yu, L.; Zhang, Q. Q.; Liu, W. C., Preparation and characterization of monocaprate nanostructured lipid carriers. *Colloids and Surfaces a-Physicochemical and Engineering Aspects* **2007,** 311, (1-3), 106-111.
31. Tikekar, R. V.; Nitin, N., Effect of physical state (solid vs. liquid) of lipid core on the rate of transport of oxygen and free radicals in solid lipid nanoparticles and emulsion. *Soft Matter* **2011,** 7, (18), 8149-8157.
32. Coupland, J. N.; McClements, D. J., Lipid oxidation in food emulsions. *Trends in Food Science & Technology* **1996,** 7, (3), 83-91.

LIST OF TABLES

LIST OF FIGURES

NLCs and 10% NLCs samples upon exposure to atmospheric air. All the data points are an average of triplicate measurements ± standard deviation.

	Melting	**Solidification**

Sample	$T_{initiation}$ (ºC)	$T_{completion}$ (ºC)	$T_{initiation}$ (ºC)	$T_{completion}$ (ºC)
SLN	36.26 (0.04)[a]	37.79 (0.0)[a]	22.53 (0.0)[a]	19.75 (0.0)[a]
1%	35.82 (0.11)[b]	37.12 (0.02)[b]	22.38 (0.02)[b]	19.79 (0.26)[a]
10%	34.31 (0.08)[c]	36.39 (0.28)[c]	21.13 (0.0)[c]	18.4 (0.18)[b]

Table 1

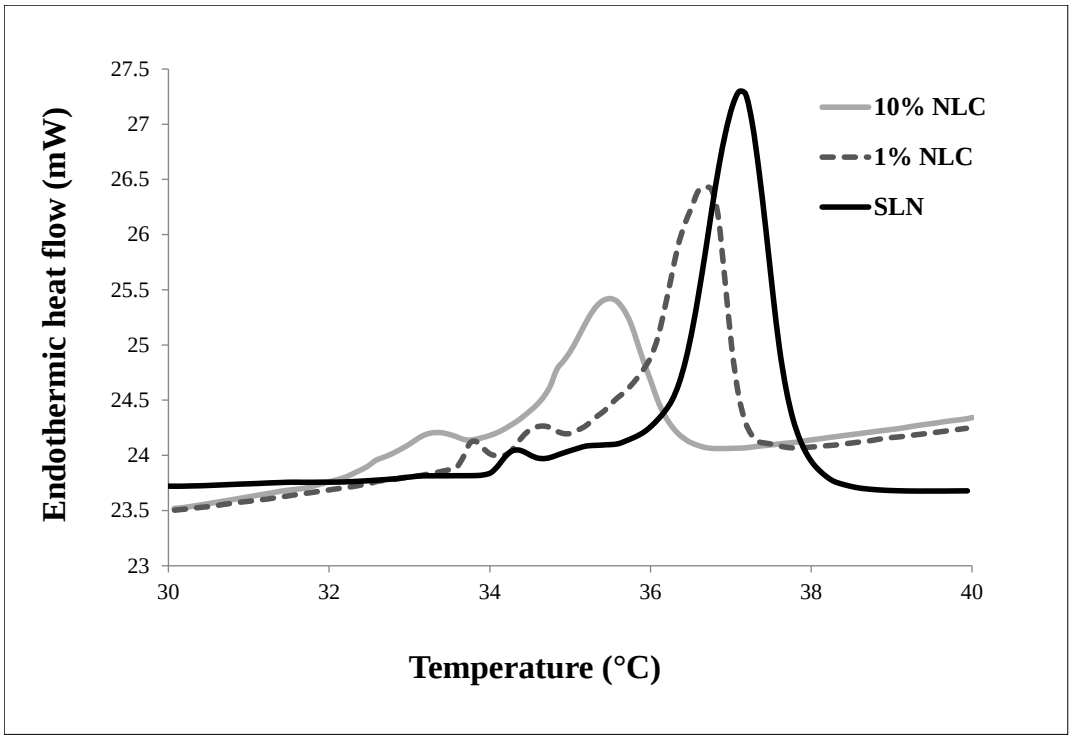
Endothermic heat flow (mW)
27.5
27
26.5
26
25.5
25
24.5
24
23.5
23
30
32
34
36
38
40
Temperature (°C)
10% NLC
1% NLC
SLN

(a)

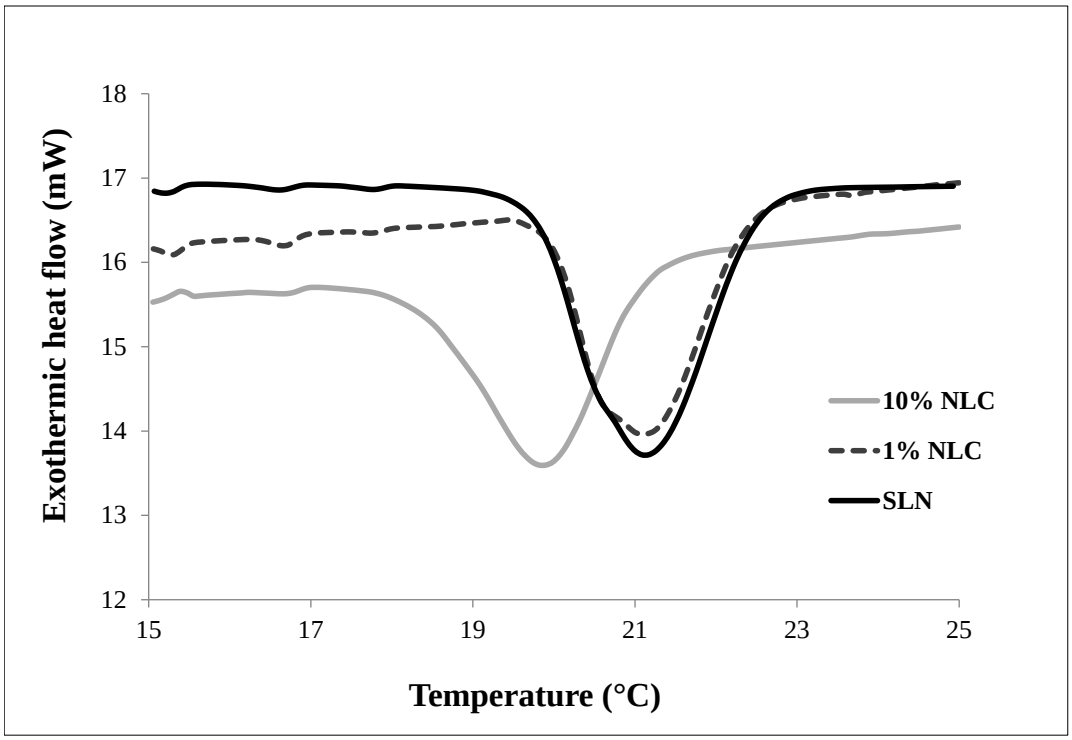
Exothermic heat flow (mW)
18
17
16
15
14
13
12
15
17
19
21
23
25
Temperature (°C)
10% NLC
1% NLC
SLN

(b)

Figure 1

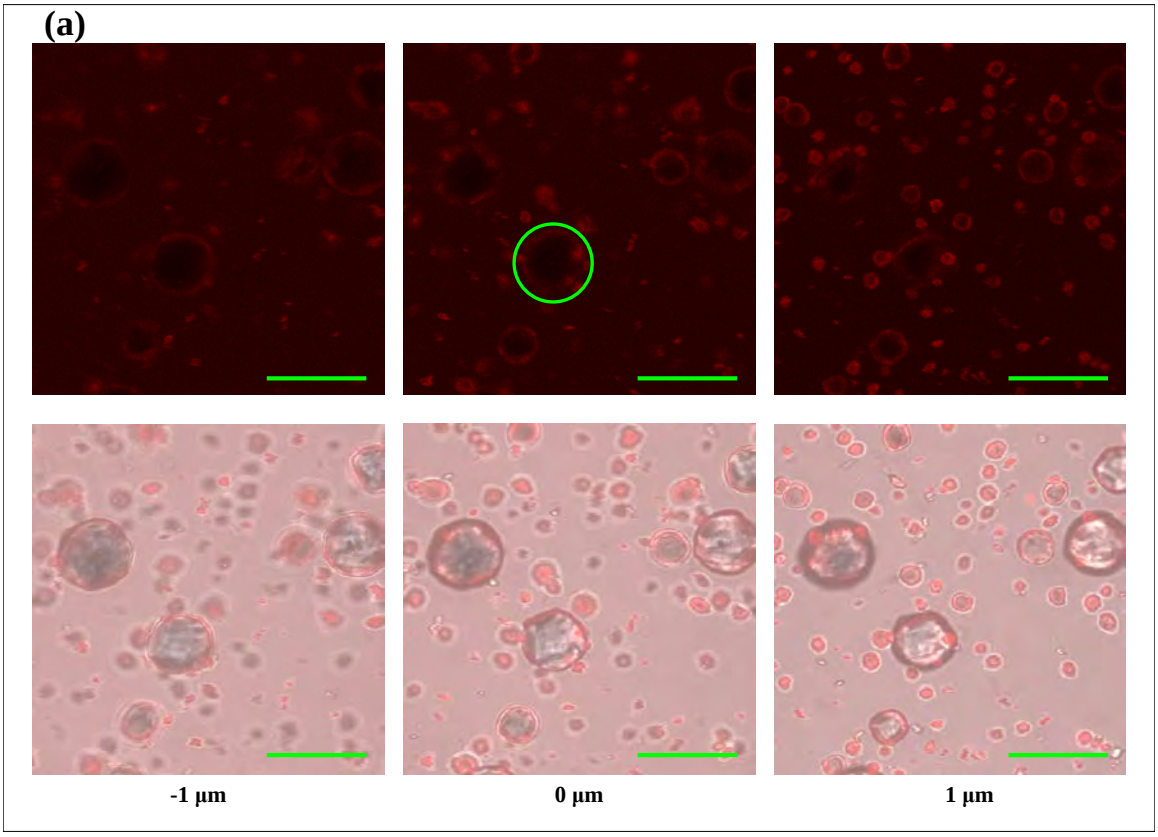
(a)
-1 µm
0 µm
1 µm

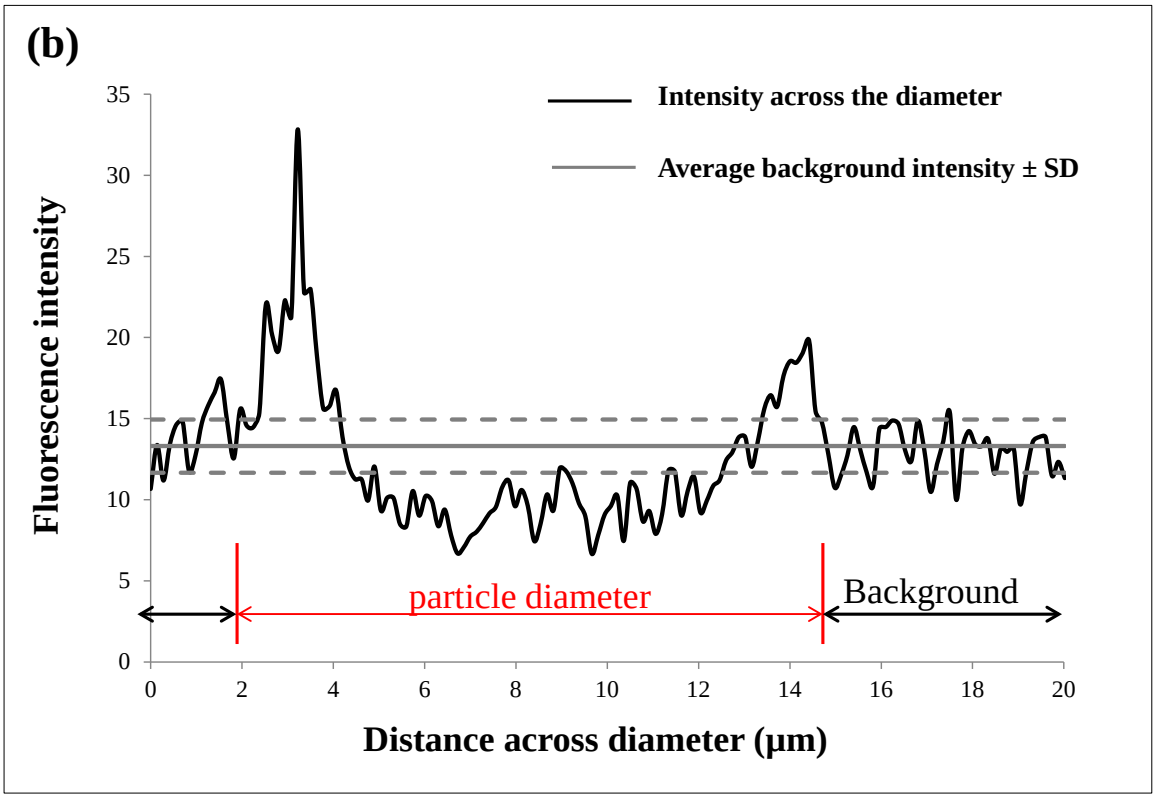
(b)
Intensity across the diameter
Average background intensity ± SD
Fluorescence intensity
35
30
25
20
15
10
5
0
0
2
4
6
8
10
12
14
16
18
20
particle diameter
Background
Distance across diameter (µm)

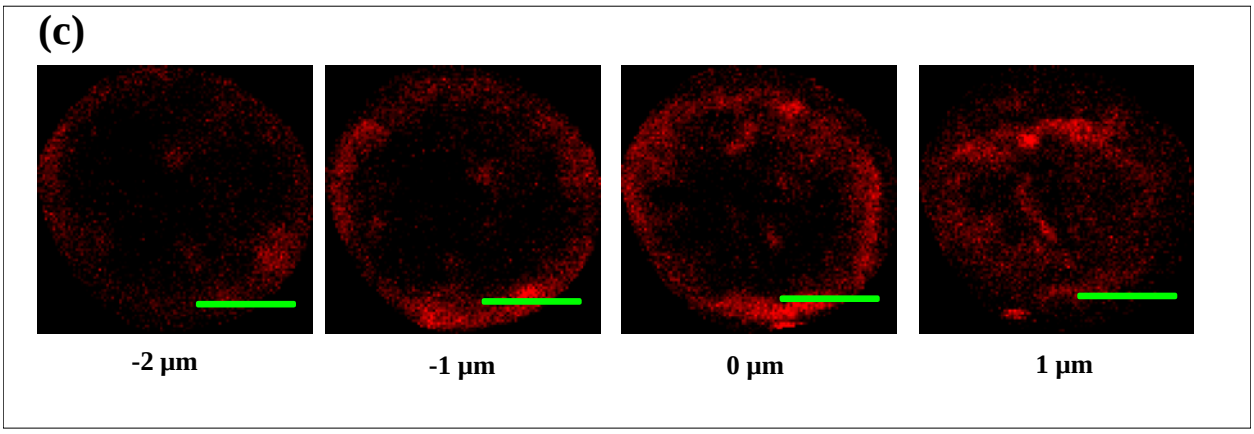

Figure 2

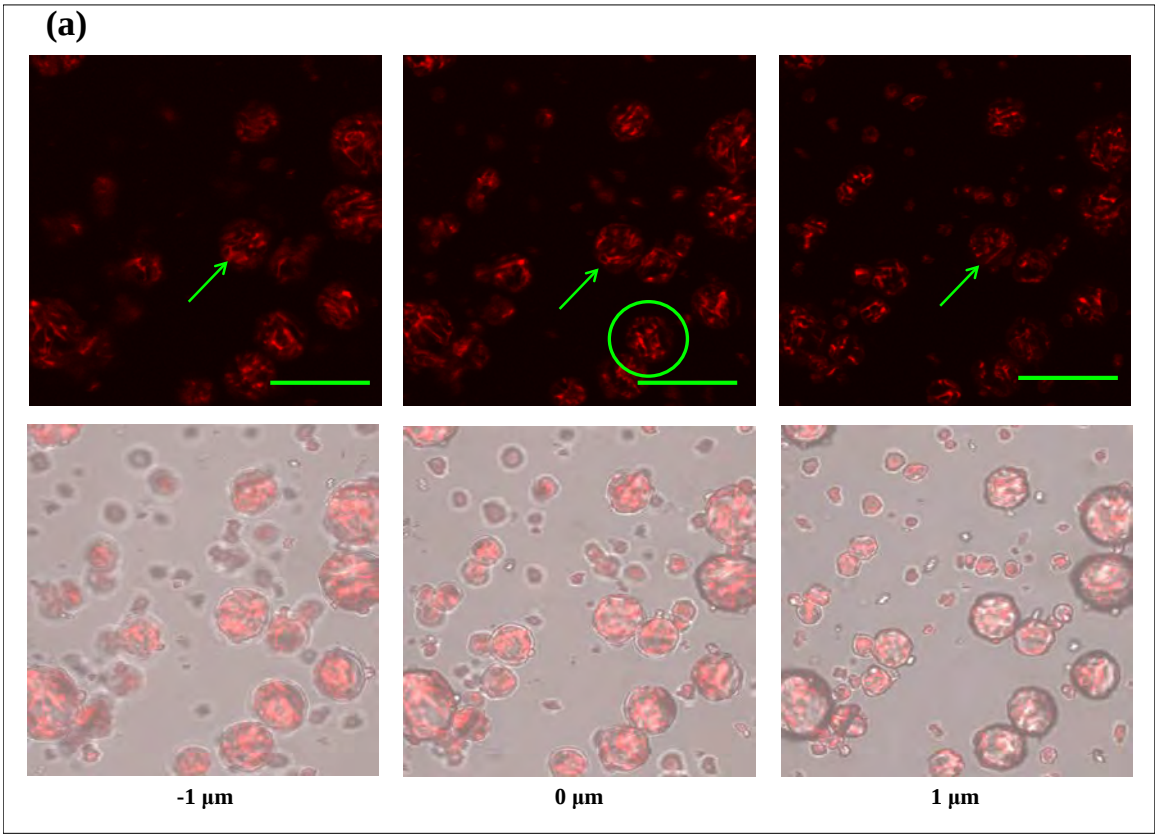
(a)
-1 µm
0 µm
1 µm

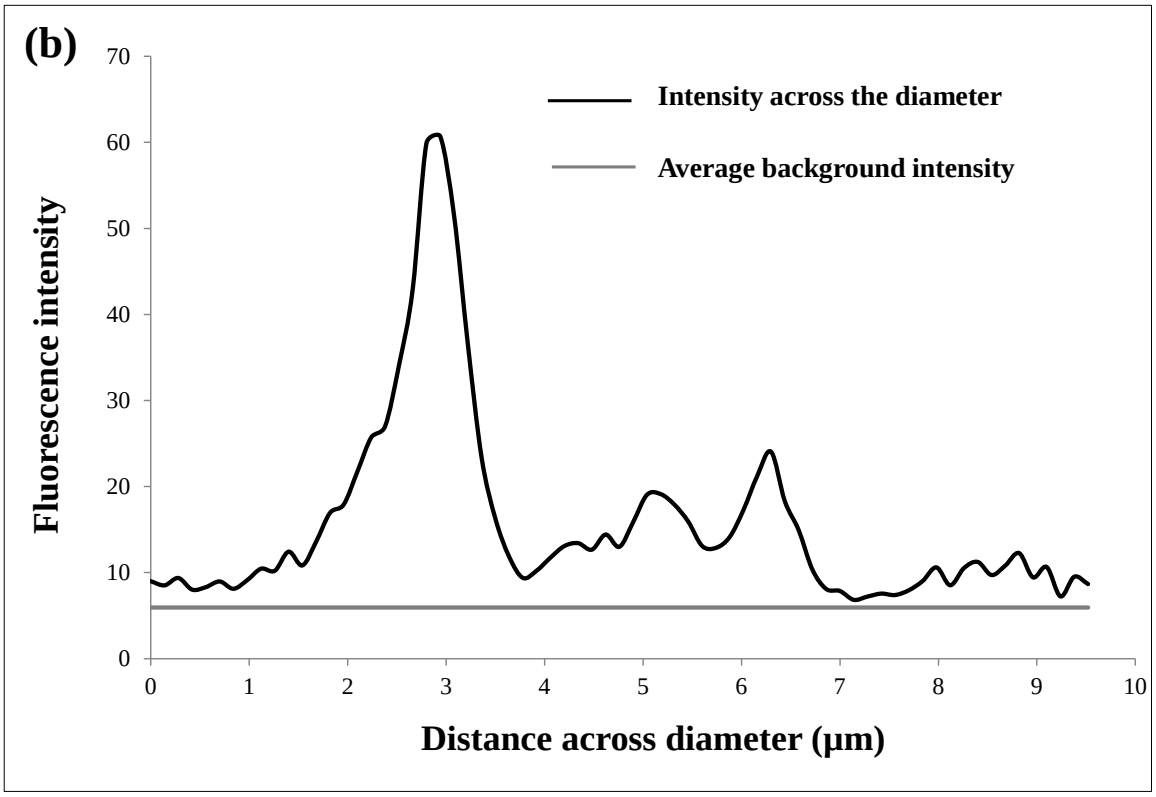
(b)
Intensity across the diameter
Average background intensity
Fluorescence intensity
Distance across diameter (µm)
0
10
20
30
40
50
60
70
0
1
2
3
4
5
6
7
8
9
10

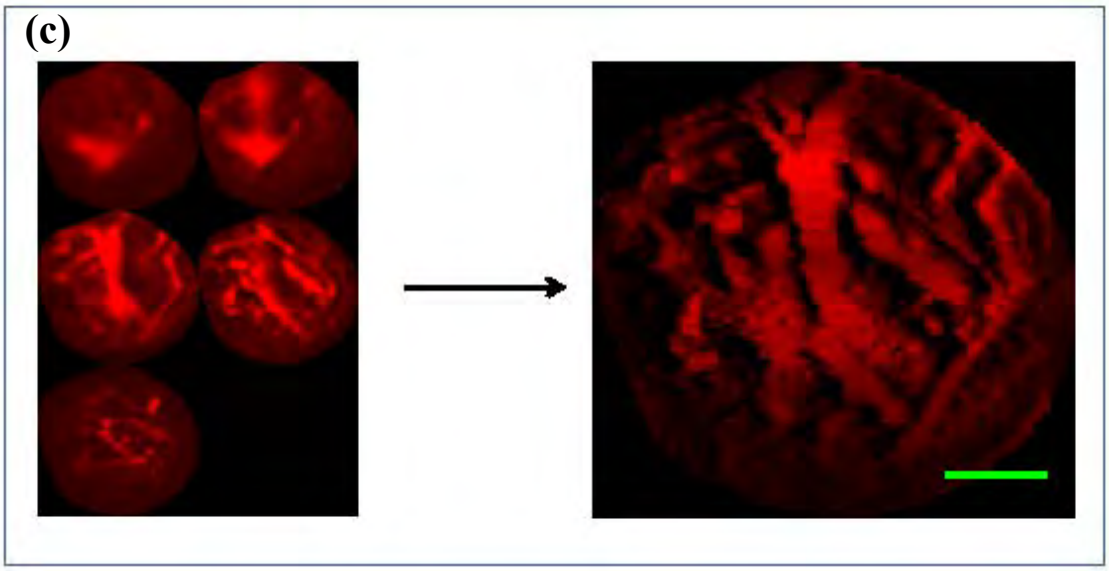

Figure 3

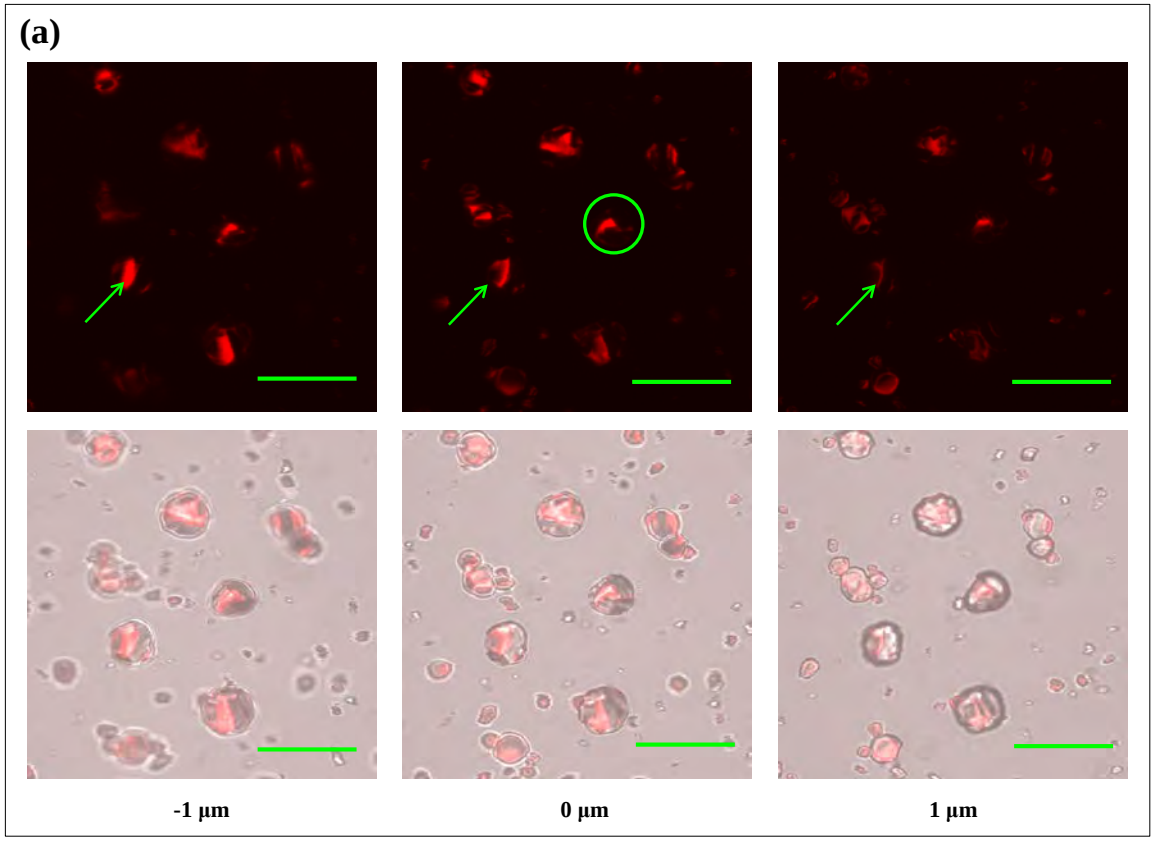
(a)
-1 µm
0 µm
1 µm

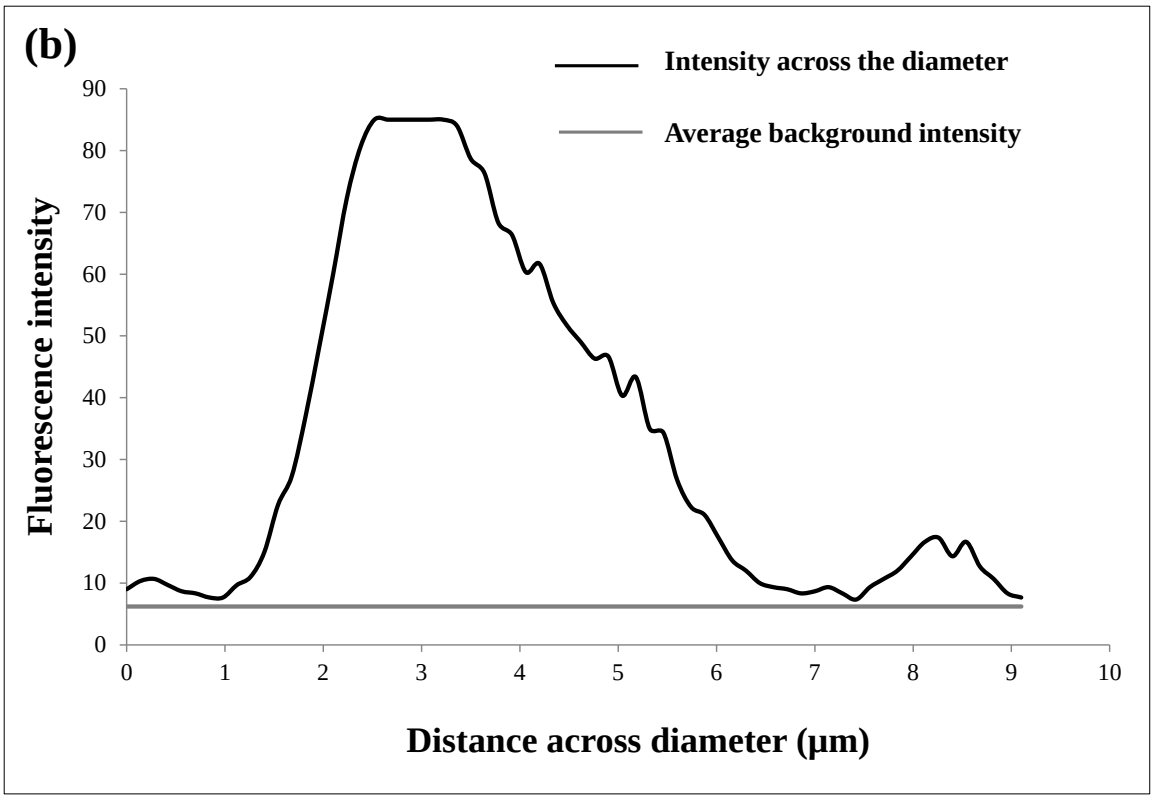
(b)
Intensity across the diameter
Average background intensity
Fluorescence intensity
0
10
20
30
40
50
60
70
80
90
0
1
2
3
4
5
6
7
8
9
10
Distance across diameter (µm)

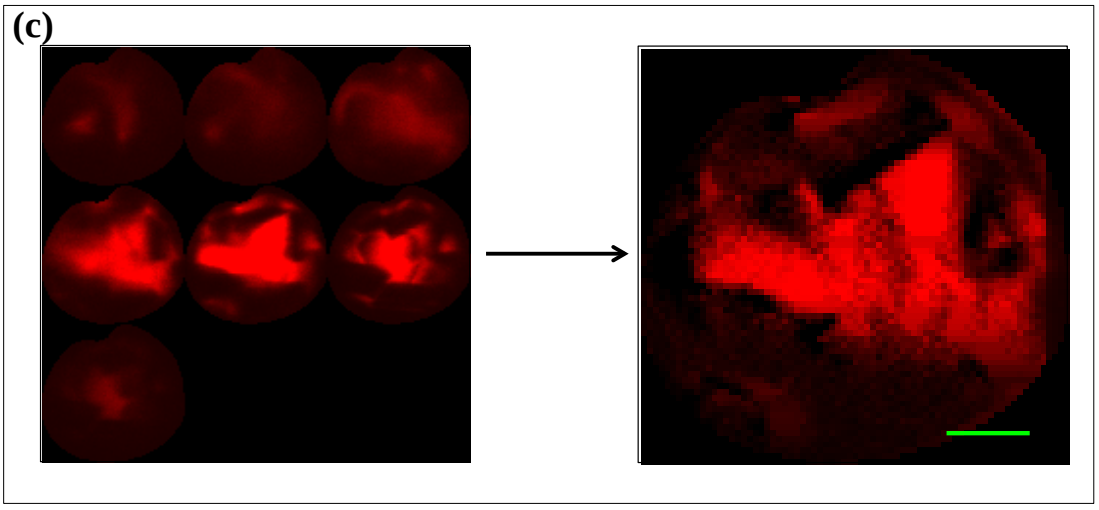

Figure 4

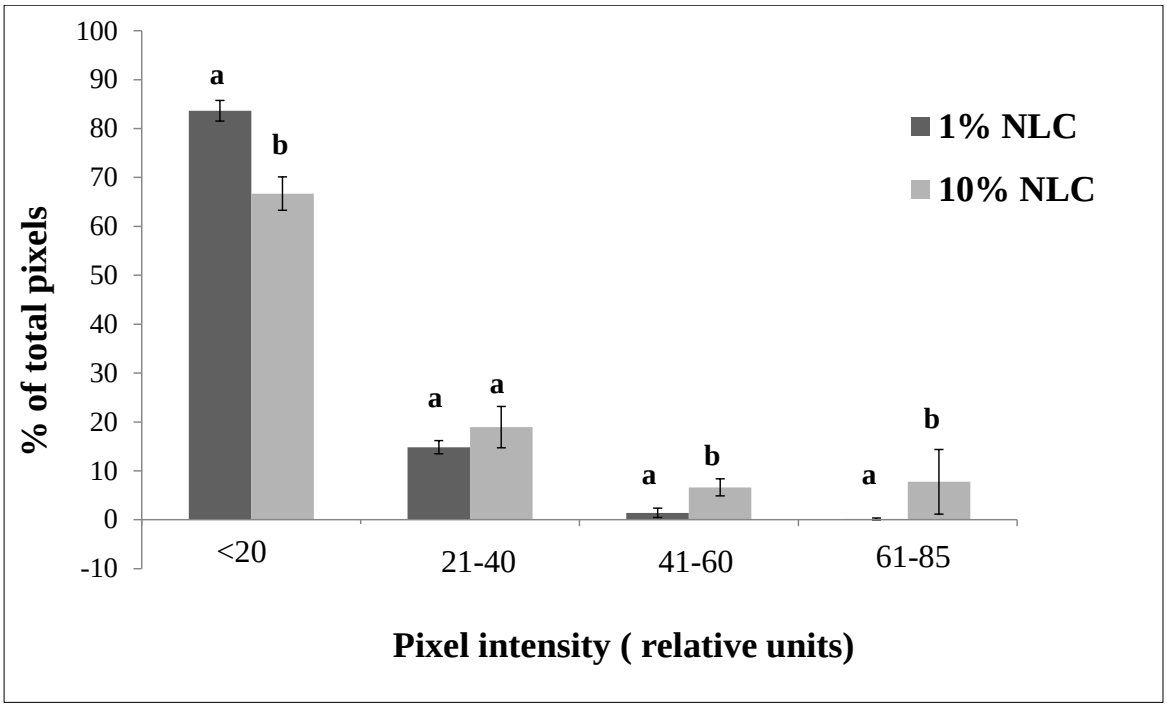
100
90
80
70
60
50
40
30
20
10
0
-10
% of total pixels
a
b
a
a
a
b
a
b
1% NLC
10% NLC
<20
21-40
41-60
61-85
Pixel intensity (relative units)

Figure 5

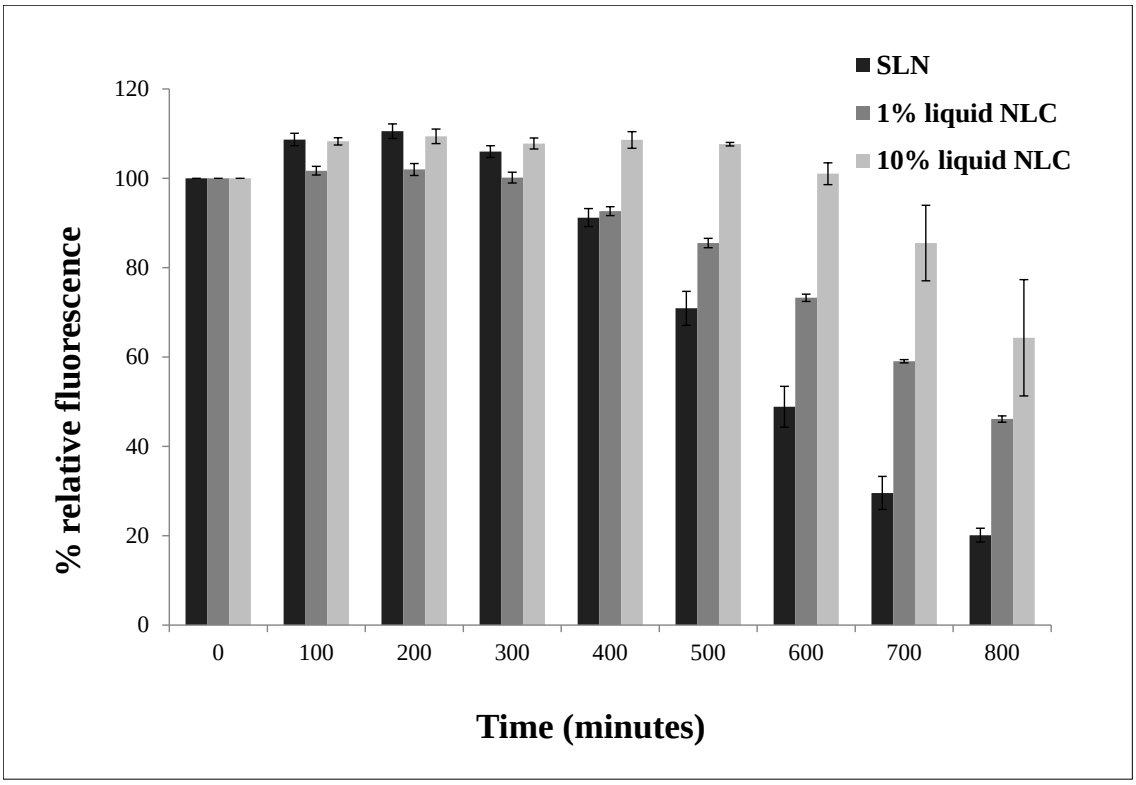
SLN
1% liquid NLC
10% liquid NLC
% relative fluorescence
120
100
80
60
40
20
0
0
100
200
300
400
500
600
700
800
Time (minutes)

Figure 6

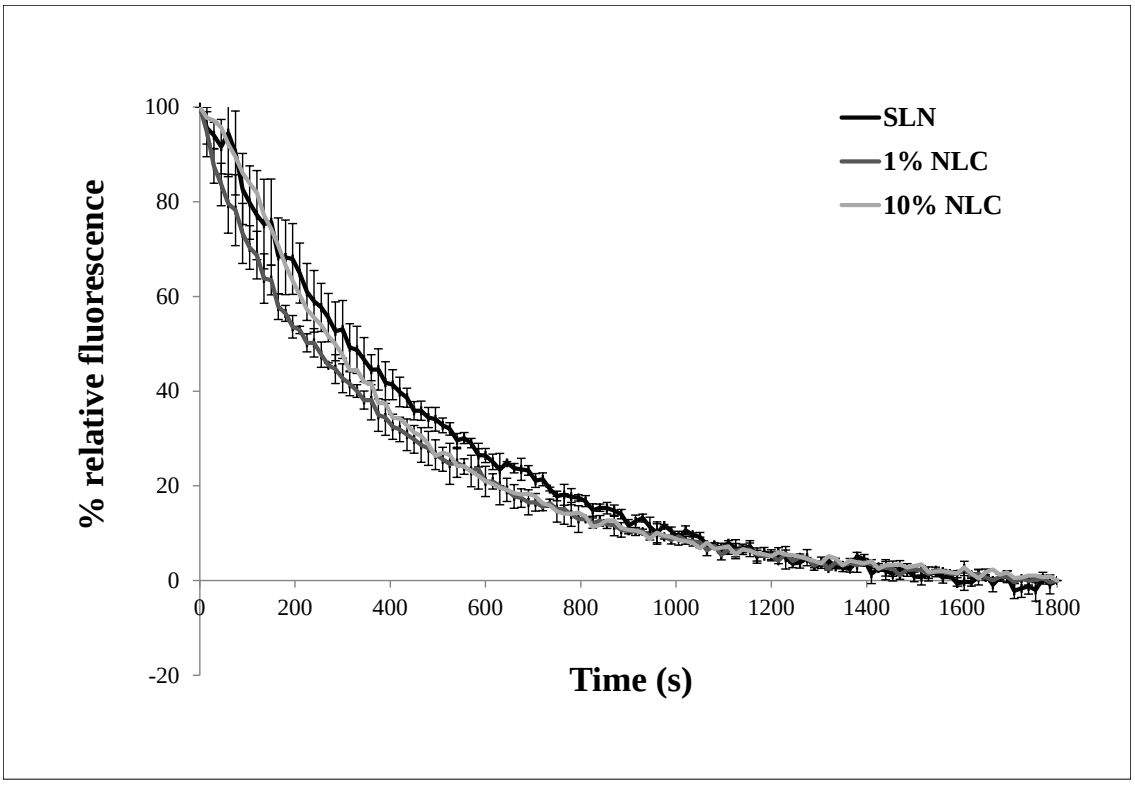
% relative fluorescence
100
80
60
40
20
0
-20
0
200
400
600
800
1000
1200
1400
1600
1800
Time (s)
SLN
1% NLC
10% NLC

Figure 7

Enhanced Antioxidant Properties of Interface and Reduced Mobility of Encapsulated Lipid Carriers to Limit Oxidation of Encapsulated Products in Emulsions and Particles

Objective II: Evaluate the influence of localized antioxidants and physical properties of the interface in limiting transport of free radicals

Key Results:

(i) Physical state of the emulsifier has significant influence on permeation of free radicals
(j) Localization of antioxidants at the interface is significantly more effective than their presence in the bulk phase
(k) Combination of engineering physical properties and controlling localization of antioxidants can be an effective approach to limit oxidation processes

Overall, these findings complement based on engineering interface complements the results of our previous report focused on engineering lipid core of the particles.

DETAILED REPORT:

Materials and Methods

Phospholipids 1,2-dipalmitoyl-sn-glycero-3-phosphocholine (DPPC) and 1,2-dilauroyl-sn-glycero-3-phosphocholine (DLPC) and cholesterol (ovine wool, >98%) were purchased from Avanti Lipids (Alabaster, AL). Dulbecco's phosphate-buffered saline (PBS) at pH 7.4 was purchased from Fisher Scientific (Pittsburgh, PA). The lipid peroxidation sensor BODIPY 665/676, fluorescent Texas Red 1,2-Dihexadecanoyl-sn-Glycero-3-Phosphoethanolamine, triethylammonium Salt (Texas Red DHPE), N-(Biotinoyl)-1,2-Dihexadecanoyl-sn-Glycero-3-Phosphoethanolamine, Triethylammonium Salt (Biotin DHPE) and NeutrAvidin biotin-binding protein were purchased from Invitrogen (Carlsbad, CA). 2,2'-Azobis(2-methylpropionamidine) dihydrochloride (AAPH), (±)-6-Hydroxy-2,5,7,8-tetramethylchromane-2-carboxylic acid (Trolox) and (±)-α-Tocopherol (vitamin E) were purchased from Sigma-Aldrich (St. Louis, MO).

Preparation of supported lipid bilayers. Lipids were suspended and stored in chloroform in the freezer (-20°C) until used. Small unilamellar vesicles (SUVs) were prepared using standard vesicle extrusion methods. Typically, a desired amount of lipid and BODIPY dye were mixed in a glass vial. The solvent was then evaporated under a stream of nitrogen and subsequently evacuated for at least 1 hour in a vacuum desiccator. The dried mixture was suspended in Millipore water and rehydrated for at least one hour at 4°C. The total lipid concentration was 2mg/mL and BODIPY was 0.5mol% of the total lipid. The desired amount of hydrated aqueous solution was then sonicated and passed through a Avanti Mini-Extruder (Avanti, Alabaster, AL) using 100nm polycarbonate membrane filters 21 times at room temperature for DLPC and at 50-55˚C for DPPC (well above the melting temperature). The lipid mixture was added to PBS in a 1:1 ratio to provide the necessary osmotic pressure to induce vesicle rupture. Next, a 40μL drop of this solution was added to a polystyrene petri dish and a no.1.5 glass coverslip (cleaned with piranha etch at room temperature for 30 minutes) was placed on top. The SUV solution was allowed to fuse for 20 minutes. To rinse away excess lipid, the dish was submerged in a large excess of water and the slide was removed and transferred to a new dish and again submerged in another large excess of water.

Double bilayer preparation. A stock solution of DLPC with 0.5mol% Biotin DHPE and 0.5mol% BODIPY 665/676 was prepared in chloroform and used to form a supported lipid bilayer using the above described experimental procedure. After rinsing, 60μL of 0.5mg/mL NeutrAvidin was added to the sample to provide an excess amount to bind the available Biotin DHPE contained in the supported membrane. The NeutrAvidin was allowed to incubate for 30 minutes then the sample was rinsed 4x in excess deionized water and placed in a new polystyrene dish. Deionized water remaining in the dish was replaced with PBS and 100μL of a 2mg/mL DLPC solution in Millipore water containing 0.5mol% Biotin DHPE and 0.5mol% TexasRed DHPE was

added. After incubation for 30 minutes, the sample was again rinsed 4x in excess deionized water and placed in a new polystyrene dish.

Ellipsometry. To prepare samples for ellipsometry, the glass coverslips used for fluorescence were replaced with piranha etched silicon substrates obtained from Ted Pella (Redding, CA). All imaging ellipsometry measurements were recorded on an Elli2000 imaging system from Nanofilm Technologie (Goëttingen, Germany) that employs a frequency-doubled Nd:YAG laser at 532nm and software-controllable motorized goniometers and polarizers. A custom-made wet cell was used to keep the sample submerged during analysis, goniometers were set to an angle of 53˚ with respect to the sample normal to keep the incident and reflected light orthogonal to the wet cell windows. A 10x objective was used to focus the laser on the sample and delta and psi values were measured by nulling the incident laser light on a 100x100pixel square region at the center of the detector/field of view (approximately 108x56μm). These measurements were repeated at five spots over the full area of the sample surface. Film thickness was calculated using a customized 3-slab model on manufacturer-supplied software. Briefly, ellipsometry makes use of the fact that elliptically polarized light reflected from a thin surface film is given a linear polarization. By measuring the complex phase shift of the reflected light relative to the incident light (delta and psi values), the height of the surface film can be calculated. For more information on determining thin film height from ellipsometric polarization measurements please see additional references[21, 24-26].

Radical generation. The coverslip supporting a lipid bilayer was maintained in a 35x10mm cell culture dish containing Millipore water. 1mL of Millipore water was replaced with AAPH dissolved in double-strength PBS to create a 20mM AAPH solution in the dish with pH7.4. The

AAPH decomposes to a cationic radical with a half-life of 10 hours, thus creating a steady source of free radicals. Imaging began immediately after introduction of the AAPH solution. To prevent free radicals from interacting with phospholipids directly and degrading the bilayer structure, only lipids with saturated hydrocarbon chains were selected in these experiments[27].

Fluorescence microscopy. Fluorescence images were recorded on an Olympus IX-series epifluorescence microscope (Center Valley, PA) with a filter set designed for the fluorophore Cy5 that also works well for BODIPY665/676. Exposure time was set to 1s and a 10x objective was used for all images. All experiments were conducted at ambient temperature (21-22˚C). For three hour experiments, images of BODIPY emission were recorded every 10 minutes; for sixteen hour experiments, images were recorded every 50 minutes. To account for sample-specific photobleaching, each time elapsed measurement was repeated without the radical generator AAPH and this decay rate was subtracted from the AAPH-induced fluorescence decay. The dynamic range of the recorded image stack was optimized by adjusting the maximum and minimum value to the highest and lowest intensity with a non-zero pixel count. To determine the change in BODIPY fluorescence as a function of time, the normalized fluorescence intensity of the entire field of view was calculated with ImageJ and plotted as a function of time. This data was fit to a monoexponential decay function of the form $y = y_0 + ae^{-bt}$ using Systat SigmaPlot software. Parameters were fit with the following constraints: $y_0 > 0$, $a > 0$ and $y_0 + a = 1$. The inclusion of a horizontal asymptote (y_0) is necessary as each image has a distribution of pixel intensities and thus does not uniformly go to zero.

Results and Discussion

Partitioning of fluorescent BODIPY 665/676

The fully formed supported lipid bilayer is extensively rinsed to remove any extraneous BODIPY dye. Since the selected dye has a strong hydrophobic character, it is not expected to partition into the aqueous environment and should remain stably localized within the lipid bilayer interior[28]. This is reflected in fluorescence measurements of supported lipid bilayers encapsulating BODIPY. The results show no significant change in BODIPY emission as a function of time (see supplemental information) in the absence of free radical generating AAPH. Because the molecular geometry of the probe is similar to other rod-shaped lipid probes such as diphenylhexatriene, the anticipated average position of BODIPY is between the two bilayer leaflets, at a distance of approximately 2nm below the hydrophobic-hydrophilic interface[29]. While the bilayer midpoint represent the time-averaged position, the fluorophore is expected to partition into two predominate orientations, parallel and orthogonal to the bilayer normal.

Verification of supported lipid membrane formation

To verify successful formation of a supported lipid membrane, two independent procedures are employed. First, the planarity of each sample is assessed by scratching the sample and imaging the resulting defect with the fluorescence microscope (see supplemental information). The ability to form a sharply focused image suggests that the fluorophores are arranged in a planar, two dimensional geometry. To obtain a more detailed characterization of sample geometry, imaging ellipsometry is used to measure the thickness of the supported phospholipid membrane. To interpret the delta and psi values measured by the ellipsometer

(see supplemental information) an accurate estimate of the refractive index for the various layers of the sample is required. The ambient water environment has an index of 1.33, the native oxide layer atop the silicon substrate is set to the software default value (1.4608) with an expected thickness of 2nm, and the silicon layer has a complex index of refraction of *4.1502 - 0.0449i.* For the phospholipid bilayer film, reported values span a range from 1.44 to 1.54; the median value of 1.49 is used here[21, 30]. Using this information, ellipsometric measurement reveals a thickness of 4.0 ± 0.3nm for a DLPC bilayer fused to a silicon substrate. This value is in good agreement with previous results obtained using ellipsometry and atomic force microscopy, which span a range from 3.0-4.3nm[21, 31].

Measurement of interaction of free radicals with DLPC supported bilayer

After validating the formation of supported bilayer, the next step was to characterize interaction of supported bilayers with peroxyl radicals. Figure 1 outlines the schematic design of lipid bilayer and its interaction with free radicals generated in the aqueous phase. Partitioning of peroxyl radicals into supported lipid bilayers and their subsequent reaction with peroxyl radical sensitive dye leads to loss in fluorescence intensity of the radical sensitive dye. Figure 2 shows the results for the DLPC supported lipid bilayer and its interaction with peroxyl radicals. Figure 2(a-b) illustrates the imaging measurements of DLPC membrane before and after treatment with AAPH. The results show significant decrease in fluorescence intensity in lipid bilayer as a result of interaction with peroxyl radicals. The normalized fluorescence intensity as a function of time for the DLPC lipid bilayer membrane is shown in Figure 2(c). The fluorescence emission decreases rapidly as a function of incubation time with AAPH and the normalized fluorescence decay fits well to a monoexponential function. This functional form suggests the dominating

behavior is first-order reaction kinetics, where reactive species permeate the membrane and chemically quench fluorescent molecules. For BODIPY quenching, the reaction equation is of the form $A + B \rightarrow A^*$ and the concentration of the fluorescent dye follows the relationship $A = A_0 e^{-rt}$ where A_0 is the initial concentration and r is a constant describing the rate of decay. From the curve fit, approximately 1.04 hours is required to induce a 1/*e* loss in the lipid probe fluorescence emission and the exponential rate constant is 2.68×10^{-4} s^{-1}. This is two orders of magnitude faster than reported values for the first-order decomposition of AAPH at pH7 (6.3×10^{-7} s^{-1}) indicating a strong chain reaction mechanism[32]. The pure DLPC supported membrane serves as the basis of comparison with the modified compositions.

Addition of cholesterol reduces the rate of interaction of peroxyl radicals with DLPC membrane

Figure 3 characterizes the change in normalized fluorescence intensity of a peroxyl radical sensitive dye in DLPC membranes with and without addition of cholesterol. The results show that introduction of 15mol% cholesterol (DLPC-CH) slowed the rate of fluorescence decay of lipid embedded peroxyl radical sensitive dye. The cholesterol-phospholipid ratio of 15:85 is sufficient to assess the effects of cholesterol on the membrane without significantly altering membrane structure or inducing lateral segregation[33]. Quantification of changes in normalized fluorescence intensity illustrates that the characteristic (1/*e*) decay time increased by a factor of 1.7 with the addition of cholesterol. Cholesterol at 15mol% only slightly reduces the lateral mobility of the membrane[34], its primary influence is to restrict the molecular orientation of the hydrocarbon chains causing the phospholipids to straighten and the bilayer to increase in height[35]. As a consequence of these changes in lipid bilayer, it is expected that the average distance of the fluorescent dye embedded in the lipid membrane with respect to water-

lipid interface.increases. This increase in distance between the interface and the location of peroxyl sensitive dye decreases the probability of interaction with free radicals as the free radicals must travel farther into the lipid membrane to react with the dye molecules. This decrease in interaction of peroxidation sensitive dye with radicals results in reduced rate of decay of fluorescence intensity as shown in Figure 3. This effect has been reported in previous studies as well[27, 36]. It is important to note that lipid peroxidation of cholesterol-phospholipid mixtures can cause molecular rearrangement and phase separation within a model membrane, however these changes occur over a period of several days and are not relevant at the timescale of the present study[37].

Changes in phase state of lipid membranes reduce the rate of interaction of radicals with supported lipid bilayers

Results in Fig. 3 also compares changes in normalized fluorescence intensity of a peroxyl radical sensitive dye as a function of physical state of lipid membranes. For evaluating the impact of physical state, interaction of radicals with the gel –phase dipalmitoyl-phophatidylcholine (DPPC) membrane is compared with the fluid phase DLPC membrane. The results of this comparison demonstrate the gel-phase lipid interface slowed the decay time by a factor of 1.9 as opposed to the 1.6-fold change in DLPC with cholesterol and a factor of 1.04 for the DLPC membrane. In this case, the slowed radical rate is likely a combination of both reduced lateral diffusion and greater separation between the sensor and aqueous phase where radicals are generated. In comparison with DLPC membrane, the lateral fluidity of DPPC is significantly reduced due to the increased intermolecular Van der Waal's interactions between the longer lipid tails (DPPC has 16 carbons, DLPC only 12)[38]. The decreased mobility

manifests as a decreased reaction rate as the collisional frequency between BODIPY and reactive species (both free radicals and chain reaction intermediates) drops. Just as in the cholesterol-doped sample, the longer phospholipid tail length also shifts the average fluorophore position deeper within the membrane structure and contributes to the reduced rate of fluorescence decay of the peroxyl sensitive dye [39].

Formation of a double bilayer membrane and interactions with peroxyl radicals

Figure 4(a) illustrates the schematic design of a double lipid bilayer membrane. The construction of a double bilayer system enables the investigation of layer-by-layer assembly of additional lipid structures as an antioxidation strategy. The process consists of three steps: first, DLPC vesicles containing BODIPY 665/676 and BODIPY-DHPE are fused to a glass substrate; second, neutravidin is allowed to bind the exposed biotin moieties on the supported bilayer; and third, DLPC vesicles with BODIPY-DHPE and TexasRed are ruptured under a strong osmotic gradient and allowed to bind the avidin surface layer. Similar to the characterization of a single bilayer membrane, two complementary charactierzation approaches are employed to verify successful formation of a double bilayer membrane. Fluorescence microscopy can characterize the uniformity of the spatial distribution of fluorescent dyes, i.e., the BODIPY in basal membrane and the TexasRed in the distal membrane. The results show that both BODIPY and TexasRed exhibit very homogeneous fluorescence (see supplemental information). A uniform fluorescence signature is emblematic of successful planar bilayer formation[40], suggesting efficient surface adhesion of lipid membrane, biotin-avidin-biotin linking and vesicle rupture/fusion.

With the same ellipsometry measurement procedure used for the single DLPC membrane, the measured thickness is 7.8 ± 0.5nm. As expected, this measurement is roughly

double the value for a single DLPC bilayer. Since the hydrophilic headgroups of phospholipids form strong hydrogen bonds with water molecules, determination of the exact refractive index of this region is difficult. Thus the thickness values reported here only include the hydrocarbon tail regions of the lipids. If the membrane-avidin-membrane structure is replaced by an effective medium with an index of refraction closer to that of water (i.e., 1.42)[41] the total film thickness becomes approximately 14nm. In this model, the 14nm height can be interpreted as a 6nm bilayer (comprising both phospholipid tail and headgroups) on top of a 2nm avidin layer on top of another 6nm bilayer. With only 0.5mol% biotin included in each membrane, the avidin is prevented from forming a tightly-packed crystal layer atop the membrane and only partially covers the surface (Fig. 4a). Since the index of refraction of protein is significantly different than water (1.50 and 1.33 respectively), the ellipsometric measurement reflects the mixed protein-water composition and is lower than previously published values for tightly packed monolayers (4-5nm)[42]. Both interpretations of the ellipsometry data show strong agreement with expectations for a linked double-bilayer configuration.

Results in Figure 4(b) compare changes in normalized fluorescence intensity of a peroxyl radical sensitive dye between the DLPC double bilayer configuration and the standard DLPC single bilayer sample. Depositing a second DLPC phospholipid bilayer on top does not appear to strongly influence the fluorescence quenching of BODIPY in the basal membrane, only a subtle increase in the characteristic decay time (a factor of 1.6 relative to the single DLPC membrane) is evident. The marginal decrease in the fluorescence decay rate of peroxyl radical sensitive dye (2.68 and 2.12×10^{-4} s^{-1} for single and double bilayer samples respectively) is predominantly attributed to increased spacing between the radical generation source (at the lipid-water interface of the protective membrane) and the peroxyl radical sensitive dye. As a result of this increased distance, the free radicals must travel a larger distance from the point of generation to the peroxidation sensor embedded in the basal lipid membrane[15]. The

probability that radicals will survive long enough to reach the peroxidation sensor is reduced in the case of double bilayer membranes and as a result the characteristic decay time for the peroxyl radical sensitive dye increases. It is important to note that since only 1 in 200 lipid molecules form the avidin-biotin linkage, it is expected that the presence of avidin does not significantly influence the mobility of the phospholipids in bilayers [23]. Overall, the subtle changes in the fluorescence decay time of peroxyl radical sensitive dye indicate that changing the physical lipid structure (mobility, molecular order and multilayer barriers) does not significantly influence the activity of free radicals in lipid structures.

Addition of antioxidants in aqueous and lipid phases

To address concerns of oxidation by aqueous-phase impurities, (such as metal ions, radical generating sources, etc.) one common approach is to add sacrificial water-soluble or amphipathic antioxidants in product formulations. These sacrificial antioxidants are expected to interact with oxidizing species to protect the encapsulated bioactive molecules or functional materials. In this study, lipid samples were prepared with either α-tocopherol or Trolox. Vitamin E (tocopherols or tocotrienols) is a naturally-occurring antioxidant that is thought to perform protective and signaling functions in biological membranes[43-45]. Due to its amphipathic nature, tocopherol has a high affinity for lipid structures[46] and it functions by binding and inactivating chemical intermediates generated during the lipid peroxidation chain reaction. Trolox is a chemical derivative of vitamin E that functions in a similar manner and is only soluble in water. For both of these chemical protection strategies, results in Figure 5 show that the monoexponential decay trend does not fit the entire experimental interval. Adding 12nM Trolox to the aqueous phase (immediately prior to the introduction of AAPH) causes a short lag phase

followed by an exponential decay rate that is very similar to the pure DLPC sample (2.68×10^{-4} and 2.41×10^{-4} s^{-1} for DLPC and Trolox respectively). The slower characteristic decay time of 1.65 hours (a factor of 1.6) is attributable to the induced lag phase. In this system, radicals are generated at a constant rate in solution by 10mM AAPH and eventually overwhelm the chemical antioxidant protection. When the antioxidation capacity of Trolox is exhausted, reactive ions are free to permeate the membrane. From previous studies, a limited amount of Trolox may partition into phospholipid membranes but with little anticipated effect on its antioxidant activity[47].

The most dramatic change in radical activity is observed with the addition of vitamin E. Here, α-tocopherol in chloroform is added to DLPC (also in chloroform) at a molar ratio of 1:10 antioxidant-to-phospholipid at the beginning of the standardized sample preparation procedure. The resulting tocopherol molar concentration is equal in mass to the amount of Trolox in the previous sample. From the plot in Figure 5(c), the measured BODIPY fluorescence emission resembles a reaction-diffusion system[48]. This suggests the radical scavenging activity of tocopherol embedded at the interface emulates a diffusional barrier that impedes radical transport from the aqueous phase into the lipid interface. This behavior is divergent from previous samples where the decay rate was determined solely by first order reaction kinetics. Here, the characteristic decay time exceeds that of a single DLPC bilayer by a factor of 10.4, requiring 10.8 hours for the BODIPY emission to drop by 1/*e*. Reaction-diffusion systems are characterized by non-linear partial differential equations whose solutions are highly complex and not very elucidative for the present study. However, if the antioxidant is treated as a temporary diffusion barrier or lag phase, then the monoexponential decay portion of the curve has a rate constant very similar to the samples with enhanced molecular order; $b = 1.45\times10^{-4}$, 1.43×10^{-4}, 1.60×10^{-4} s^{-1} for α-tocopherol, DPPC and DLPC-CH samples respectively. In fact, prior studies have show that vitamin E has the effect of increasing order in phospholipid membranes in a similar manner to cholesterol and gel phase lipids[49, 50].

Conclusions

In this study the role of physical and chemical properties of lipid interface in modulating free radical mediated oxidation reactions is quantitatively evaluated. The physical properties of lipid interface are engineered based on composition (gel phase lipids vs. fluid phase lipids and addition of cholesterol to lipid membranes) and formation of a double bilayer membrane structure based on biotin-avidin-biotin layer-by-layer assembly. Influence of the chemical properties of the lipid interface is also assessed by direct addition of antioxidant molecules to the lipid membranes and the aqueous phase. Quantification of interactions of peroxyl radicals with lipid membranes is based on the relative fluorescence decay of peroxyl radical sensitive dye embedded in the lipid membranes.

The results presented here demonstrate that localization of chemical antioxidants at the lipid interface is an order of magnitude more effective in suppressing permeation of free radicals in membranes than increasing lipid ordering, adding cholesterol, attaching an additional lipid membrane or introducing chemical antioxidants to the bulk aqueous phase. Lipid peroxidation typically begins when free radicals are generated in the aqueous phase where oxygen, iron and other radical-generating impurities reside. Reactive species must then diffuse across the water-lipid interface in order to break down lipid-encapsulated compounds. Since most radicals are short-lived, only those generated near the interface have the necessary lifetime to survive transit into the membrane. Thus localizing protectants at the interface allows antioxidants to interact with nascent reactive species and possibly prevent the lipid peroxidation chain reaction[51].

This localization phenomenon also arises in other studies, where lipid chain length and hydrophobicity of antioxidants are shown to significantly influence antioxidant activity[52-57]. It is likely that the molecular structures with enhanced activity correspond to the closest

partitioning of the antioxidant to the interface where it may interfere with chain reaction initiation and scavenge free radicals directly before they can breakdown encapsulated species and create reactive intermediates. Thus, when designing lipid-based encapsulations to maximize resistance to radical breakdown, the ideal strategy is to localize chemical protectants at the water/lipid interface.

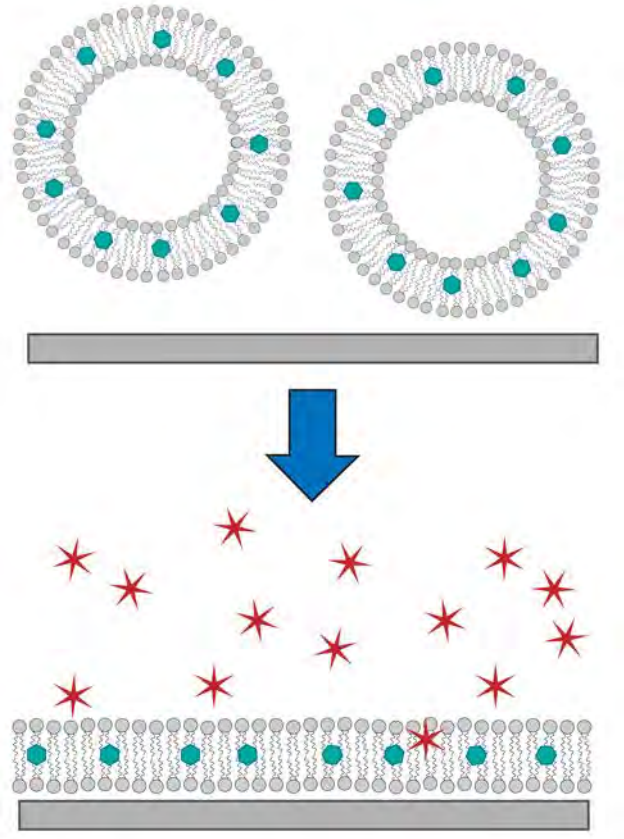

Figure 1. Illustration of supported lipid bilayer formation via vesicle fusion. Small unilamellar vesicles composed of phosphatidylcholine (*light gray*) and 0.5mol% BODIPY 665/676 (*green*) rupture and adsorb to a glass substrate (*dark gray*). After rinsing away excess lipid, AAPH is

added to generate free radicals (*red*) which penetrate the planar supported bilayer and react with the fluorescent lipid peroxidation sensor.

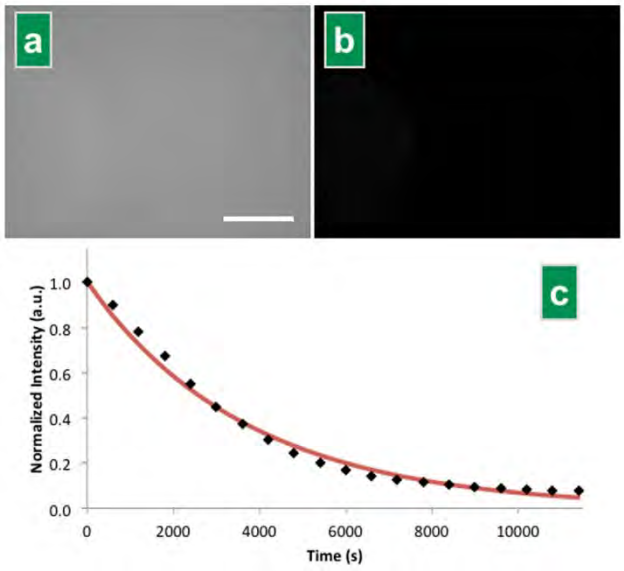

Figure 2. Fluorescence microscopy measurements of DLPC supported membrane. The BODIPY fluorescence emission under a 10x objective is shown (*a*) before AAPH addition and (*b*) after three hour incubation. Inset scale bar represents 100μm. (c) The normalized BODIPY fluorescence emission as a function of time.

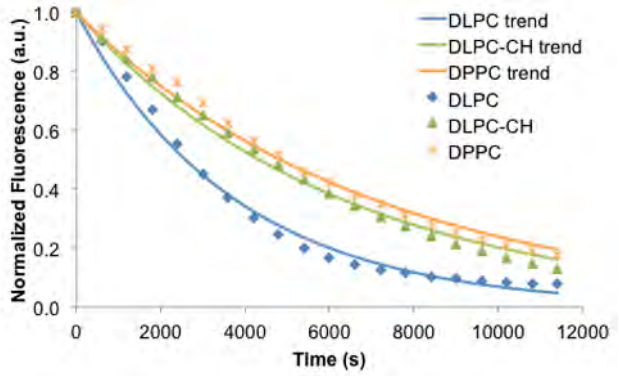

Figure 3. Physical protectants against free radical degradation. Raw data points are shown for dimyristoyl-phosphatidylcholine (*DLPC*), DLPC with 15mol% cholesterol (*DLPC-CH*) and dipalmitoyl-phosphatidylcholine (*DPPC*) along with the results of the nonlinear regression.

Table 1 – Results of nonlinear regression of changes in the normalized fluorescence intensity as a function of time in lipid membranes with compositional modifications of the lipid interface

Sample	**y_0**	**error**	**a**	**error**	**b (s^{-1})**	**Error**	**R^2**	**1/e (hr)**	**Norm. 1/e**
DLPC	2.68E-04	0.0240	1.00	0.0261	2.68E-04	2.04E-05	0.9900	1.04	1.0
DLPC-CH	1.45E-13	0.0435	1.00	0.0373	1.60E-04	1.51E-05	0.9931	1.74	1.7
DPPC	9.91E-14	0.0605	1.00	0.0525	1.43E-04	1.03E-05	0.9907	1.94	1.9

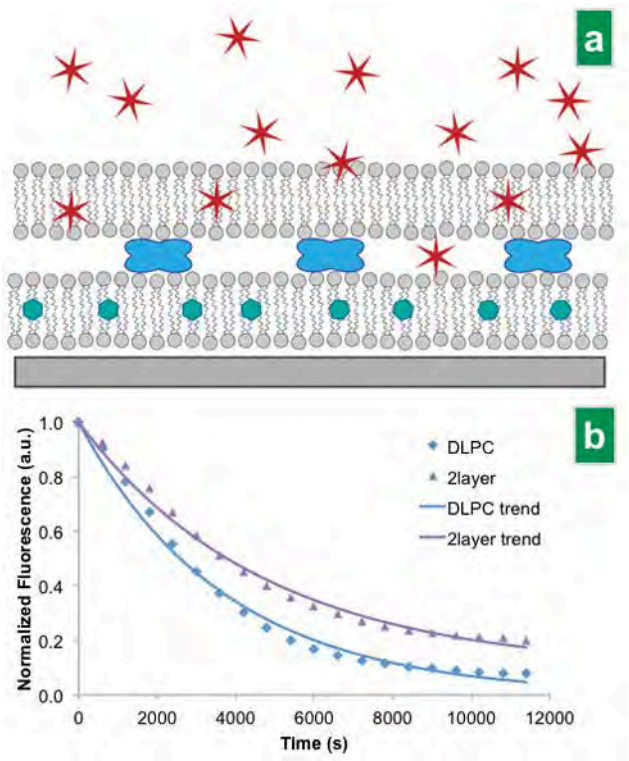

Figure 4. Schematic and fluorescence decay of double bilayer sample. (a) Here an additional DLPC membrane is constructed on top of a base DLPC membrane with 0.5mol% Biotin-DHPE. First, avidin (*blue*) is allowed to attach to the proximal supported membrane then DLPC vesicles with Biotin are allowed to bind and rupture to form a second bilayer as cover. Free radicals (*red*) generated above the protective top membrane diffuse across the lipid bilayer and interact with the lipid sensor embedded in the bottom membrane. (b) BODIPY fluorescence decay in the sample with an additional protective membrane (*2layer*) compared against the DLPC control (*DLPC*).

Table 2 –Results of nonlinear regression of changes in the normalized fluorescence intensity as a function of time in lipid membranes with physical modifications of the lipid interface

Sample	**y_0**	**error**	**a**	**error**	**b (s^{-1})**	**Error**	**R^2**	**1/e**	**Norm.**

								(hr)	**1/e**
DLPC	2.68E-04	0.0240	1.00	0.0261	2.68E-04	2.04E-05	0.9900	1.04	1.0
2layer	0.0932	0.0282	0.907	0.0255	2.12E-04	1.75E-05	0.9914	1.70	1.6

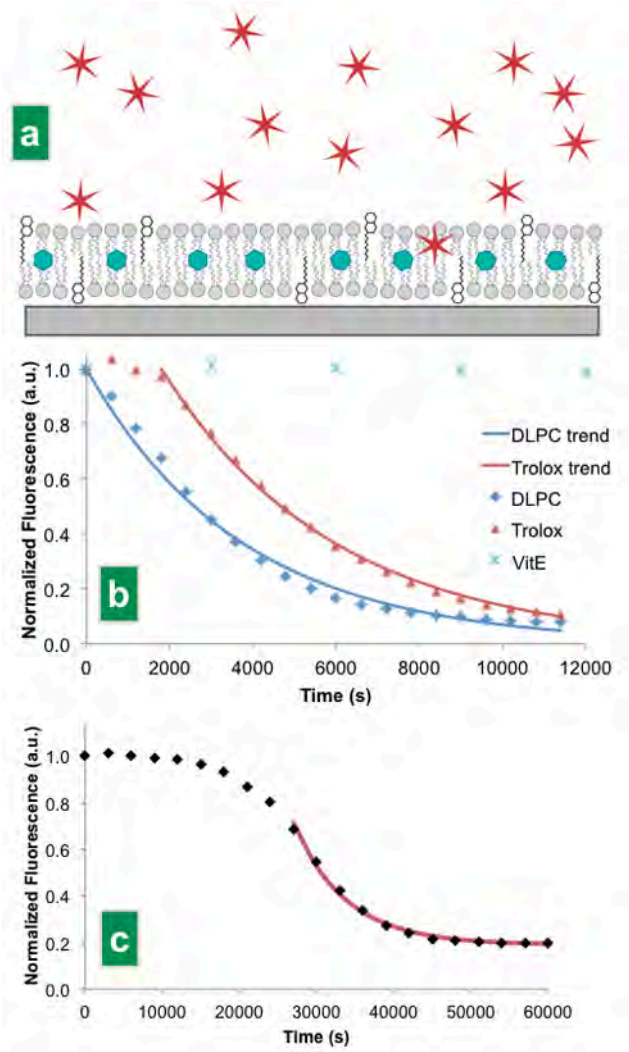

Figure 5. Chemical protectants against free radical degradation. (a) Schematic of α-tocopherol (*black and white*) incorporation into a supported phospholipid membrane. (b) BODIPY fluorescence emission for samples with Trolox in the aqueous phase (Trolox), α-tocopherol in the membrane (vitE) and the DLPC comparison standard. All curves are plotted on the same axes. (c) Long timescale emission of BODIPY in a DLPC membrane with incorporated α-tocopherol (vitE).

Table 3 – Results of the nonlinear regression of changes in the normalized fluorescence intensity as a function of time in lipid membranes with chemical protectants added to the aqueous or lipid phase

Sample	**y_0**	**error**	**a**	**error**	**b (s^{-1})**	**Error**	**R^2**	**1/e (hr)**	**Norm. 1/e**
DLPC	2.68E-04	0.0240	1.00	0.0261	2.68E-04	2.04E-05	0.9900	1.04	1.0
Vitamin E	0.1908	0.0236	0.809	0.0540	1.45E-04	1.75E-05	0.9281	10.79	10.4
Trolox	1.98E-12	0.0192	1.00	0.0159	2.41E-04	1.21E-05	0.9979	1.65	1.6

Objective IIII: Antioxidant activity of emulsifiers can significantly improve oxidative stability of encapsulated bioactives

Key Results:

(d) Selection of emulsifiers with antioxidant properties is an effective approach to improve oxidative stability of encapsulated bioactives

(e) This approach may have significant cost benefits as compared to exogenous addition of antioxidants

(f) This approach also indicates that localization of antioxidants at the interface is also an effective approach as it increases the localized concentration of the antioxidant

DETAILED REPORT

2. Materials and methods

2.1. Materials

Tween 20, bile salts, sodium azide, 2,2'-azobis-2-methylpropanimidamide dihydrochloride (AAPH), organic canola oil, ferric chloride, 2-thiobarbituric acid (TBA), trichloroacetic acid (TCA), propyl gallate, 2,4,6-tris(2-pyridyl)-s-triazine (TPTZ), and curcumin from *Curcuma longa* (Turmeric) were obtained from Sigma-Aldrich (St Louis, MO). Glacial acetic acid, sodium acetate, hydrochloric acid, dibasic sodium phosphate, sodium ethylenediamine tetraacetate (EDTA) and acetone were purchased from Fisher Scientific. Ultrapure water (16MΩ-cm) was obtained from in-house water filtration system. Low melting lecithin (LML) (ALCOLEC®PC 75) was a gift from American Lecithin Inc. (Oxford, CT). A peroxyl radical sensitive dye, BODIPY®665/676 dye was purchased from Invitrogen Incorporated (Carlsbad, CA).

2.2. Ferric reducing ability of antioxidant (FRAP) assay to measure antioxidant activity of Tween 20 and lecithin

Antioxidant activity was measured based on ferric reducing ability of antioxidant compounds (FRAP assay) as described by Benzie and Strain (Benzie and Strain, 1996). Reagents needed for this assay included 300 mM acetate buffer (pH 3.60), 10 mM TPTZ in 40 mM HCl, and 20 mM $FeCl_3$. Working FRAP reagent was prepared by mixing 25 mL acetate buffer, 2.50 mL TPTZ solution, and 2.50 mL $FeCl_3$ solution. 900 µL working FRAP solution was mixed with 50 µL of 2 mM emulsifier solution and 90 µL ultrapure water. Absorbance of this mixture was measured immediately at 593 nm and normalized against a blank that was

prepared by mixing 900 µL FRAP reagent solution and 140 µL ultrapure water (without emulsifier). Antioxidant activity of Tween 20 and lecithin was compared to a known antioxidant standard, trolox. To obtain the trolox equivalent values for Tween 20 and lecithin, absorbance values (FRAP assay measurement) as a function of trolox concentration (0-60 µM) were measured and a standard curve was generated. Trolox equivalent values for Tween 20 and lecithin were determined based on this standard curve.

2.3. UV induced oxidation of lecithin

Lecithin was oxidized by UV treatment (intensity 1.60 mW/cm^2). UV lamp was pre-heated for 30 minutes, and the incident UV intensity was measured at the base of a lamp using a radiometer (Blak-ray ultraviolet meter, Ultra-violet Products Inc., San Gabriel, CA). 20 mM lecithin dissolved in ultrapure water was exposed to UV light for 2 hours with continuous stirring.

2.4. Oxidation reduction potential (ORP) assay

Changes in ORP (induced by UV induced oxidation process) of lecithin solution upon exposure to UV light were measured and compared with control sample that was exposed to ambient air and light. ORP measurements (mV) of both treated and control samples were recorded every 20 minutes using the ORP Tester (Oakton Instruments, Vernon Hills, IL) at room temperature.

2.5. Thiobarbituric acid reactive substances (TBARS) assay

UV induced lecithin oxidation was also characterized using the standard TBARS assay. Using this assay, concentration of thiobarbituric acid reactive substances produced as a result of oxidation of lecithin was measured using the procedure described by Alamed and others (Alamed et al., 2009). Briefly, a buffer solution containing 50 mM dibasic sodium phosphate, 0.10% EDTA, and 0.10% propyl gallate was prepared and kept cold (4-8 °C). A 30% TCA solution and a 0.02 M TBA solution was prepared and kept cold as well. 1 mL of 20 mM lecithin or oxidized lecithin solution, 8 mL cold buffer solution and 2 mL TCA solution were added to a test tube and centrifuged at 2000 g for 5 minutes in a centrifuge. 2 mL aliquot from the supernatant layer was mixed with 2 mL TBA solution. The samples were incubated in a boiling water bath for 15 minutes followed by a cooling step in which the samples were cooled using an ice water bath for 1 minute and then transferred to a refrigerator to cool for 30 minutes. Absorbance values of the samples were measured at 532 nm.

2.5. Emulsion preparation

In order to prepare Tween 20 emulsion, 20 mM Tween 20 (2.46 g/100 mL) was dissolved in ultrapure water. A stock dye solution was prepared by dissolving 5 mg peroxyl radical sensitive dye in 1 mL chloroform. A working dye solution was prepared by ten-fold

dilution of this stock solution using chloroform. The working dye solution was added to canola oil to achieve a final dye concentration of 25 μg/g in oil (the final volume of chloroform is about 0.0001% in oil). Coarse emulsions were prepared by dispersing 4 g of this oil in Tween 20 solution using a hand-held disperser (Ultra-Turrax model T25, IKA Works, Wilmington, NC) set at 9500 rpm for two minutes. The coarse emulsion was subsequently passed five times through a single stage homogenizer (Niro Soavi, Parma, Italy) operating at approximately 600 bar. 0.10% sodium azide was added to emulsion samples to prevent microbial growth and the emulsion samples were stored at 4 °C until further use.

Lecithin stabilized emulsion was prepared using the same approach as outlined above for Tween 20 emulsion. Material composition of lecithin emulsion was 1.46 g (20 mM) lecithin, 0.50 g (0.50% w/v) bile salts (co-emulsifier) and 4 g of canola oil containing 25 μg/g of peroxyl radical sensitive dye in 100 mL ultrapure water. The pH was adjusted to 6.50 for both Tween 20 and lecithin emulsions. The oxidized lecithin emulsion was prepared using the same approach as described for the lecithin emulsion.

2.6. Particle size measurements

Hydrodynamic diameter of emulsion droplets was measured using a particle size analyzer (Model: Malvern Nano Series, Malvern Instruments, Inc., Westborough, MA). The settings for the analyzer were- material type: oil, particle refractive index = 1.45, dispersant type: water, dispersant refractive index= 1.33, temperature: 25 °C. Particle size measurements were analyzed based on the number average particle size distribution.

2.7. Fluorescence imaging of encapsulated BODIPY dye and curcumin in emulsions

Fluorescence images were obtained to demonstrate that the BODIPY dye was uniformly distributed in Tween 20 and lecithin emulsion droplets. It was difficult to visualize and measure the distribution of the dye in Tween 20 and lecithin emulsions due to their small particle size (around 120nm) based on their fluorescence intensity. To overcome this limitation, coarse emulsion with the same proportions of oil and aqueous phase was prepared using a hand-held disperser. Confocal microscopy was conducted using a Zeiss LSM 510 Meta confocal microscope. Confocal imaging of Tween 20 and lecithin emulsion droplets was obtained using a 63× oil objective with a numerical aperture (NA) of 1.4. The images of samples encapsulating the BODIPY dye (as described above) were obtained using a 633 nm laser excitation. The emission signal was detected using a Meta detector. The Meta spectrometric detector integrated the fluorescence emission signal between the wavelengths of 660 and 710 nm. Similar to the above approach, the fluorescence imaging data was also acquired for the curcumin encapsulated in oil in water emulsions using the coarse emulsion stabilized by Tween

20 and lecithin emulsifiers respectively. For imaging curcumin, the emulsion samples were excited using a 488 nm laser excitation and the fluorescence emission from the encapsulated curcumin were acquired using a band pass emission filter from 515-560 nm. These imaging parameters to image the endogenous fluorescence of curcumin are based on the results of the prior studies(Kunwar et al., 2006; Sahu et al., 2008).

2.8. Measurements of peroxyl radical permeation from the aqueous to the lipid phase of emulsions

AAPH was selected as a peroxyl radical generator in the aqueous phase of emulsions. AAPH solution was prepared by dissolving 0.10 g AAPH in 10 mL ultrapure water. 1 mL emulsion was mixed with 1 mL AAPH solution to achieve a final concentration of 20 mM AAPH in the emulsion. Immediately after addition of AAPH, the samples were placed in a 96 well plate along with the controls (samples of emulsion mixed with equal volume of ultrapure water). Changes in fluorescence intensity of a peroxyl radical sensitive dye (BODIPY®665/676) were measured at a regular time interval of 20 minutes for a total time of 16 hours using a plate-reader (Spectramax M5, Molecular Devices, Carlsbad, CA). The excitation and emission wavelengths for fluorescence measurements were 620 nm and 675 nm respectively. The relative fluorescence intensity was calculated using the following equation:

$$Relative\ fluorescence\ intensity = \frac{I_{t\ AAPH}/I_{0\ AAPH}}{I_{t\ control}/I_{0\ control}} \times 100$$

where $I_{t\ AAPH}$ = fluorescence intensity of treatment emulsion after 't' minutes of exposure to AAPH, $I_{0\ AAPH}$ = fluorescence intensity of treatment emulsion immediately after addition of AAPH, $I_{t\ control}$ = fluorescence intensity of control emulsion after time 't' minutes, $I_{0\ control}$ = fluorescence intensity of control emulsion at time t = 0 minute. The changes in fluorescence intensity were fit to an exponential model of the form $y = ae^{-\left(\frac{x}{b}\right)^c}$ using Matlab CFTool 2012. A non-linear regression model with "Trust Region" algorithm was used for fitting the data.

2.9. Curcumin stability in emulsions

Tween 20 and lecithin emulsions encapsulating curcumin were prepared using the same experimental approach as described for the emulsion samples encapsulating a radical sensitive dye. Concentrations of emulsifiers and oil were increased two fold as compared to the previous emulsion formulations (for measurements of radical permeation) to improve encapsulation efficiency of curcumin in selected emulsions. 1.60 mg curcumin was added to 8 g oil to achieve a final concentration of 200 µg/g oil. Concentration of curcumin was selected based on the solubility limit of curcumin in oil. To determine the solubility limit, curcumin-oil mixture with a

varying concentration of curcumin (50-500 µg/g oil) was vigorously mixed and centrifuged at 14000 g for 10 minutes to precipitate un-dissolved curcumin. Based on these measurements, the maximum solubility limit of curcumin was determined to be approximately 300 µg/g oil. For stability experiments, a final concentration of 200 µg of curcumin/g oil was selected as it is well within the solubility range (approximately 66% of the maximum solubility limit) of curcumin in the oil phase. Curcumin containing emulsions were prepared using the method described earlier.

Oxidative stability of encapsulated curcumin was measured by characterizing changes in absorbance of curcumin as a function of incubation time. Emulsions containing encapsulated curcumin were incubated with and without 20 mM AAPH at 22 °C in dark for 72 hours. To measure curcumin concentration, emulsions were disrupted by adding 1 mL acetone to 400 µL emulsion. The mixture was centrifuged at 14000 g for 10 min. 1mL of the supernatant was placed in a cuvette and the absorbance was measured at 425 nm using a UV-Visible spectrophotometer (GENESYS 10S Series, Thermo Scientific). A blank sample was prepared using 1 mL acetone and 400 µL ultrapure water.

3. Results

3.1. Particle size measurements

Figure 1 and **Table 1** compare the particle size distributions and the mean particle diameter for Tween 20, lecithin and oxidized lecithin stabilized emulsions, respectively. Comparison among emulsion samples shows significant overlap in the particle size distributions for the emulsions stabilized using Tween 20, lecithin and oxidized lecithin. The mean particle diameter of the selected emulsions ranged between 100-150 nm. These results demonstrate that the selected emulsions had similar particle size distributions. Stability of emulsion samples was also evaluated based on visual inspection during storage (2 weeks). Based on visual evaluation, emulsion samples were stable without any visible phase separation for at least 2 weeks.

3.2. Antioxidant activity of Tween 20 and lecithin

Antioxidant activity of Tween 20 and lecithin emulsifiers was measured using the FRAP assay. The FRAP assay provides quantitative assessment of the ability of a compound to reduce metal ions. In this assay, reduction of ferric-tripyridyltriazine complex to the ferrous form was monitored by measuring an increase in absorbance at 593 nm (intense blue color is formed) (Benzie and Strain, 1996). The corrected absorbance and trolox equivalent values for Tween 20 and lecithin were measured based on the FRAP assay as described in the materials and methods section. Based on these measurements, the Trolox equivalent values for Tween 20 and lecithin were 0.03 ± 0.00 and 2.57 ± 0.10 µmol/g, respectively. These measurements

demonstrate that antioxidant activity of lecithin is significantly higher (approximately 100 fold higher) than that of Tween 20.

3.3. Peroxyl radical permeation measurements using Tween 20 and lecithin stabilized emulsions

After characterizing the antioxidant properties of Tween 20 and lecithin emulsifiers, the next step was to compare the efficacy of selected emulsifiers in limiting permeation of free radicals from the aqueous phase to the oil phase of emulsions. Permeation of free radicals (peroxyl radicals) from the aqueous phase to the oil phase of emulsions was measured based on changes in fluorescence intensity of peroxyl radical sensitive dye encapsulated in the oil phase of emulsions. This approach has been successfully used in our prior studies to measure the influence of lipid core design and the interfacial composition on the rate of permeation of peroxyl radicals across emulsions, nanoparticles and lipid bi-layers (Bricarello et al., 2012; Tikekar and Nitin, 2011, 2012).

Prior to real time measurement of interactions of free radicals with the encapsulated dye, spatial distribution of peroxyl radical sensitive BODIPY dye encapsulated within oil droplets was characterized using fluorescence imaging of Tween 20 and lecithin coarse emulsion droplets (**Figure 2(a)**). **Figure 2(b)** shows the normalized fluorescence intensity profiles across the diameter of selected droplets from lecithin and Tween 20 emulsions. The mean fluorescence intensity of the dye in the oil phase was approximately 1000 fold higher than the background fluorescence in the aqueous phase. Based on the visual evaluation and the fluorescence intensity line scans of selected droplets, it is evident that the dye was uniformly distributed in the oil phase of emulsions for both the emulsions with no significant partitioning of the dye (based on the fluorescence intensity line scan) in the aqueous phase of emulsions. This imaging data demonstrates that the selected dye is hydrophobic with no significant solubility in the aqueous phase and the emulsifier does not influence the distribution of the dye. The results of these imaging measurements are in agreement with the results from our prior study (Tikekar and Nitin, 2011).

In addition to hydrophobicity, the selected BODIPY dye has high specificity to react with peroxyl radicals and upon reaction with peroxyl radicals, fluorescence intensity of the dye is quenched (Tikekar and Nitin, 2011). Peroxyl free radicals in the aqueous phase were generated using AAPH. Due to relatively long half-life (approximately 175 hours) of APPH in aqueous solution (Zimowska et al., 1997), the rate of generation of peroxyl radicals can be maintained

constant for an extended duration of time. In addition to our prior studies (Tikekar and Nitin, 2011, 2012), other investigators have also used AAPH to induce oxidation in emulsions(Azuma et al., 2009; Kubouchi et al., 2002; Watanabe et al., 2010). **Figure 3** characterizes the relative decrease in fluorescence intensity of peroxyl radical sensitive dye encapsulated in the oil phase of Tween 20 and lecithin emulsions with AAPH treatment. Fluorescence intensity of encapsulated dye in emulsions decreased as a function of time with AAPH treatment. The results show that the rate of decrease in fluorescence intensity in lecithin emulsion was significantly lower than that in Tween 20 emulsion. In lecithin emulsion, the relative fluorescence intensity of encapsulated peroxyl radical sensitive dye was maintained constant (close to 100% level) for an extended time (approximately 600 minutes) prior to a decrease in fluorescence intensity. However, in Tween 20 emulsion the relative fluorescence intensity of encapsulated peroxyl radical sensitive dye decreased exponentially without any extended period with constant relative fluorescence intensity. To quantify differences in the decay of relative fluorescence intensity between lecithin and Tween-20 emulsions, the experimental data was fitted to a generalized exponential function of the form $y = ae^{-\left(\frac{x}{b}\right)^c}$, where a is the initial intensity of fluorescence, b is the constant describing the rate of decay, and c is the shape parameter. The results of the curve fitting analyses are shown in **Table 2**. Based on this analysis, decay in fluorescence intensity of the encapsulated BODIPY dye followed a first order kinetics in Tween 20 emulsions and a non-linear kinetics in lecithin emulsion with a shape factor >1. These results are in agreement with the results of a study by Watanabe et al. (Watanabe et al., 2010). In this study, the authors demonstrated that the oxidation of encapsulated oil in emulsion follows a non-linear kinetics. Quantitative comparison of the kinetic measurements show that the time required for an exponential decay (1/e) in fluorescence intensity is approximately 2 fold higher in lecithin emulsion (~17.7 hours) as compared to Tween 20 emulsion (8.1 hours). These results suggest that interfacial barrier properties of lecithin emulsions reduce the rate of permeation of peroxyl radicals across the emulsion interface as compared to Tween 20 emulsions. These differences in the rate of permeation of free radicals can be attributed to higher antioxidant activity of lecithin (demonstrated earlier using the FRAP assay) as compared to Tween 20. It is important to note that other experimental parameters such as pH, temperature, concentration of emulsifier were maintained constant between the lecithin and Tween 20 emulsions. Furthermore, the size of emulsion droplets was also similar between these samples (**Figure 1**). In order to validate that the differences in the rate of permeation of peroxyl radical were indeed due to antioxidant activity of lecithin, the peroxyl radical permeation rates were compared between emulsions stabilized by lecithin and oxidized lecithin respectively.

3.4. UV induced oxidation of lecithin

Lecithin was oxidized using UV radiation. Oxidation of lecithin was characterized using two complementary analytical approaches. During the UV treatment, change in ORP (oxidation reduction potential) of lecithin solution was measured using an ORP meter as described in the materials and methods section. This approach provides a rapid measurement of UV induced oxidation of lecithin solution. **Table 3** shows ORP values for lecithin solution prior to exposure (control) and after exposure (2 hours) to ambient and to UV light respectively. A significant ($p<0.05$) increase in the ORP value (approximately 2 fold increase) of lecithin solution upon UV exposure indicates oxidation of lecithin solution (Cui et al., 2009; Liao et al., 2007). To complement the ORP measurements, UV induced oxidation of lecithin was also characterized using the TBARS assay. TBARS is a well-established spectrophotometric approach to measure oxidation of lipids (Mcdonald and Hultin, 1987). The results in **Table 3** show that the relative concentration of TBARS in UV-oxidized lecithin was significantly higher as compared to the control lecithin. Combined together, these results demonstrated that exposure of lecithin solution to UV resulted in oxidation of lecithin.

3.5. Peroxyl radical permeation in emulsions stabilized by lecithin and oxidized lecithin respectively

Figure 4 compares changes in the relative fluorescence intensity of peroxyl radical sensitive dye encapsulated in the oil phase of lecithin and oxidized lecithin stabilized emulsions respectively. The results show that the rate of decay in fluorescence intensity of encapsulated dye upon exposure to AAPH was higher in emulsion stabilized by oxidized lecithin as compared to emulsion stabilized by native lecithin ($p<0.05$). These results clearly demonstrate that UV induced oxidation of lecithin reduced the barrier properties of native lecithin molecules to limit permeation of peroxyl radicals from the aqueous to the oil phase of emulsion. Based on the curve fit analysis, an average of 17.7 and 13.1 hours are required to induce an exponential loss in fluorescence intensity of encapsulated dye in lecithin and oxidized lecithin emulsions, respectively. The curve fitting analysis also shows that the shape factor (c) for the oxidized lecithin stabilized emulsion (c value of 2.3) was significantly ($p<0.05$) reduced as compared to the shape factor for the native lecithin emulsion (c value of 4.4). This indicates a decrease in the lag period during which fluorescence intensity remained close to 100% and an increase in the rate of fluorescence decay in emulsion stabilized by oxidized lecithin. It is important to note that emulsions stabilized with oxidized lecithin had similar particle size distribution as compared to native lecithin. These results provide direct evidence that antioxidant activity of emulsifier has a

significant impact on the barrier properties of emulsion interface in limiting permeation of free radicals.

3.6. Stability of curcumin in Tween 20 and lecithin emulsions

Impact of antioxidant properties of emulsifiers on stability of encapsulated curcumin (a model bioactive susceptible to oxidation) was evaluated. In order to characterize the spatial distribution of curcumin within oil droplets, fluorescence images of Tween 20 and lecithin coarse emulsion droplets were obtained (Figure 5). Based on these imaging measurements, it is evident that curcumin was uniformly distributed in the oil phase of emulsions for both the selected emulsifiers.

Results in **Figure 6a** compare stability of curcumin in AAPH treated and control Tween 20 emulsions. The results show that over 80% of the encapsulated curcumin degraded in AAPH treated Tween 20 emulsion after 72 hours of incubation. In contrast, the control Tween 20 emulsion (without AAPH treatment) lost only 13% of the encapsulated curcumin during the same incubation time. Results in **Figure 6b** compare stability of curcumin in AAPH treated and control lecithin emulsions. During the first 24 hours of incubation, no significant degradation of encapsulated curcumin was observed in AAPH treated lecithin emulsion ($p>0.05$). This result is in contrast to the results obtained for the Tween 20 stabilized emulsions, in which approximately 42% of the encapsulated curcumin degraded under the same set of experimental conditions. These differences in the rate of degradation of curcumin between lecithin and Tween 20 stabilized emulsions follow a similar trend as the differences in the rate of permeation of free radicals in these emulsions (**Figure 3**). Similar to the results of radical permeation measurements, lecithin stabilized emulsions show an initial lag period during which there was no significant loss in curcumin concentration. After 72 hours, approximately 40% of the encapsulated curcumin was degraded in lecithin emulsion treated with AAPH, while approximately 80% of the encapsulated curcumin was degraded in Tween 20 stabilized emulsions under the same set of experimental conditions. These results demonstrate that lecithin stabilized emulsion was more effective in limiting oxidative degradation of encapsulated curcumin as compared to Tween 20 emulsion upon exposure to AAPH. It is important to note that AAPH treatment of emulsion samples simulates an accelerated oxidative stability analysis of encapsulated bioactives. The time required for inducing oxidation in emulsions using the AAPH approach in this study is similar to the results of a previous study (Watanabe et al., 2010). These results validate that antioxidant properties of emulsion interfaces can significantly influence oxidative degradation of encapsulated bioactives.

4. Discussion

Based on real time fluorescence spectroscopy measurements, permeation of free radicals across the emulsion interface was measured. This approach provides a direct measurement of barrier properties of the emulsifiers (Tikekar et al., 2011; Tikekar and Nitin, 2011) in encapsulation formulations. These measurements are independent of susceptibility of diverse bioactive compounds to oxidation processes. Thus, the results obtained from these measurements can evaluate barrier properties of the encapsulation matrix against free radical permeation. Furthermore, this approach can be extended to perform high throughput screening of multiple formulations.

The results of this study demonstrate that emulsifiers with antioxidant properties can reduce permeation of free radicals across the emulsion interface and enhance oxidative stability of encapsulated bioactive compound. These findings are in agreement with the results of prior studies (Astete et al., 2011; Hunneche et al., 2008; Nakamura et al., 1992; Osborn-Barnes and Akoh, 2003; Tong et al., 2000; Yuji et al., 2007), although in many of the prior studies (Osborn-Barnes and Akoh, 2003; Tong et al., 2000) it was not clearly established if the differences in oxidative stability of lipids or encapsulated bioactives were indeed due to the antioxidant properties of emulsifiers. To address these limitations, emulsifier compounds with similar molecular weight, but distinct antioxidant properties were selected. In addition, free radical permeation rates between UV-oxidized lecithin and native lecithin stabilized emulsions were also compared. These measurements demonstrate that antioxidant properties of emulsifiers can significantly influence permeation of free radicals across the emulsion interface.

Correlation between radical permeation measurements (**Figure 3**) and oxidative stability of encapsulated curcumin (**Figure 6**) illustrates that the experimental approach based on radical permeation measurements has the sensitivity to detect oxidative changes in bioactive compounds. Further research is required to extend this measurement approach to predict long-term storage stability of encapsulated bioactive compounds under diverse environmental conditions. This predictive approach can have a significant impact on reducing the time required for shelf life testing across diverse industries as well as selection of optimized formulation to extend the shelf life of bioactives.

5. Conclusions

This study demonstrates a novel experimental approach to measure oxidative barrier properties of emulsion interface. This experimental approach can complement the conventional measurements based on formation of conjugated dienes and volatile compounds. The results of

this study have demonstrated that antioxidant activity of emulsifiers (Tween 20 and lecithin) can significantly influence permeation of free radicals across the interface of oil-in-water emulsion and the rate of oxidation of bioactive encapsulant. Lecithin showed significantly higher antioxidant activity than Tween 20 and oxidized lecithin. Consequently, the rate of permeation of peroxyl radicals was significantly lower in lecithin stabilized emulsions as compared to Tween 20 and oxidized lecithin stabilized emulsions. Encapsulated curcumin was more stable in lecithin stabilized emulsions as compared to curcumin in Tween 20 stabilized emulsions. The results of this study demonstrate that higher antioxidant activity of emulsifier can significantly lower the rate of radical permeation and consequently reduce the rate of oxidation of encapsulated material in oil-in-water emulsion systems.

Acknowledgements

This research was supported by funding from ACS-PRF (award # 51459-DNI5); NSF-CAPPS and UC-Davis. Authors also acknowledge assistance from UC-Davis food science teaching laboratory for fluorescence spectroscopy measurements.

References

Alamed, J., Chaiyasit, W., McClements, D.J., Decker, E.A., 2009. Relationships between Free Radical Scavenging and Antioxidant Activity in Foods. Journal of Agricultural and Food Chemistry 57, 2969-2976.

Anand, P., Kunnumakkara, A.B., Newman, R.A., Aggarwal, B.B., 2007. Bioavailability of curcumin: Problems and promises. Molecular Pharmaceutics 4, 807-818.

Astete, C.E., Dolliver, D., Whaley, M., Khachatryan, L., Sabliov, C.M., 2011. Antioxidant Poly(lactic-co-glycolic) Acid Nanoparticles Made with alpha-Tocopherol-Ascorbic Acid Surfactant. Acs Nano 5, 9313-9325.

Azuma, G., Kimura, N., Hosokawa, M., Miyashita, K., 2009. Effect of Droplet Size on the Oxidative Stability of Soybean Oil TAG and Fish Oil TAG in Oil-in-Water Emulsion. Journal of Oleo Science 58, 329-338.

Benzie, I.F.F., Strain, J.J., 1996. The ferric reducing ability of plasma (FRAP) as a measure of "antioxidant power": The FRAP assay. Analytical Biochemistry 239, 70-76.

Berton, C., Ropers, M.H., Viau, M., Genot, C., 2011. Contribution of the Interfacial Layer to the Protection of Emulsified Lipids against Oxidation. Journal of Agricultural and Food Chemistry 59, 5052-5061.

Bouyer, E., Mekhloufi, G., Rosilio, V., Grossiord, J.L., Agnely, F., 2012. Proteins, polysaccharides, and their complexes used as stabilizers for emulsions: Alternatives to synthetic surfactants in the pharmaceutical field? International Journal of Pharmaceutics 436, 359-378.
Bricarello, D.A., Prada, M.J., Nitin, N., 2012. Physical and chemical modifications of lipid structures to inhibit permeation of free radicals in a supported lipid membrane model. Soft Matter 8, 11144-11151.
Cui, X.D., Shang, Y.C., Shi, Z.X., Xin, H.W., Cao, W., 2009. Physicochemical properties and bactericidal efficiency of neutral and acidic electrolyzed water under different storage conditions. Journal of Food Engineering 91, 582-586.
Evans, E.I., 1935. Antioxidant properties of vegetable lecithin. Industrial and Engineering Chemistry 27, 329-331.
Feigenbaum, J., 1946. ANTIOXIDANT EFFECT OF COMMERCIAL LECITHIN IN FORTIFIED MARGARINE. Nature 157, 770-771.
Frankel, E.N., Huang, S.W., Kanner, J., German, J.B., 1994. Interfacial Phenomena in the Evaluation of Antioxidants - Bulk Oils Vs Emulsions. Journal of Agricultural and Food Chemistry 42, 1054-1059.
Haahr, A.M., Jacobsen, C., 2008. Emulsifier type, metal chelation and pH affect oxidative stability of n-3-enriched emulsions. Eur J Lipid Sci Tech 110, 949-961.
Huang, S.W., Frankel, E.N., Schwarz, K., Aeschbach, R., German, J.B., 1996. Antioxidant activity of carnosic acid and methyl carnosate in bulk oils and oil-in-water emulsions. J Agr Food Chem 44, 2951-2956.
Hunneche, C.S., Lund, M.N., Skibsted, L.H., Nielsen, J., 2008. Antioxidant activity of a combinatorial library of emulsifier - Antioxidant bioconjugates. Journal of Agricultural and Food Chemistry 56, 9258-9268.
Joseph, S., Bunjes, H., 2012. Preparation of Nanoemulsions and Solid Lipid Nanoparticles by Premix Membrane Emulsification. Journal of Pharmaceutical Sciences 101, 2479-2489.
Judde, A., Villeneuve, P., Rossignol-Castera, A., Le Guillou, A., 2003. Antioxidant effect of soy lecithins on vegetable oil stability and their synergism with tocopherols. Journal of the American Oil Chemists Society 80, 1209-1215.
Kargar, M., Spyropoulos, F., Norton, I.T., 2011. The effect of interfacial microstructure on the lipid oxidation stability of oil-in-water emulsions. Journal of Colloid and Interface Science 357, 527-533.
Kerwin, B.A., 2008. Polysorbates 20 and 80 used in the formulation of protein biotherapeutics: Structure and degradation pathways. Journal of Pharmaceutical Sciences 97, 2924-2935.

Kubouchi, H., Kai, H., Miyashita, K., Matsuda, K., 2002. Effects of emulsifiers on the oxidative stability of soybean oil TAG in emulsions. Journal of the American Oil Chemists Society 79, 567-570.
Kunwar, A., Barik, A., Pandey, R., Priyadarsini, K.I., 2006. Transport of liposomal and albumin loaded curcumin to living cells: An absorption and fluorescence spectroscopic study. Biochimica Et Biophysica Acta-General Subjects 1760, 1513-1520.
Liao, L.B., Chen, W.M., Xiao, X.M., 2007. The generation and inactivation mechanism of oxidation-reduction potential of electrolyzed oxidizing water. Journal of Food Engineering 78, 1326-1332.
Lin, C.C., Lin, H.Y., Chen, H.C., Yu, M.W., Lee, M.H., 2009. Stability and characterisation of phospholipid-based curcumin-encapsulated microemulsions. Food Chemistry 116, 923-928.
Lomova, M.V., Sukhorukov, G.B., Antipina, M.N., 2010. Antioxidant Coating of Micronsize Droplets for Prevention of Lipid Peroxidation in Oil-in-Water Emulsion. Acs Applied Materials & Interfaces 2, 3669-3676.
McClements, D.J., Decker, E.A., 2000. Lipid oxidation in oil-in-water emulsions: Impact of molecular environment on chemical reactions in heterogeneous food systems. J Food Sci 65, 1270-1282.
Mcdonald, R.E., Hultin, H.O., 1987. Some Characteristics of the Enzymatic Lipid-Peroxidation System in the Microsomal Fraction of Flounder Skeletal-Muscle. Journal of Food Science 52, 15-&.
Mei, L.Y., McClements, D.J., Decker, E.A., 1999. Lipid oxidation in emulsions as affected by charge status of antioxidants and emulsion droplets. J Agr Food Chem 47, 2267-2273.
Nakamura, S., Kato, A., Kobayashi, K., 1992. Enhanced Antioxidative Effect of Ovalbumin Due to Covalent Binding of Polysaccharides. Journal of Agricultural and Food Chemistry 40, 2033-2037.
Onoue, S., Uchida, A., Kuriyama, K., Nakamura, T., Seto, Y., Kato, M., Hatanaka, J., Tanaka, T., Miyoshi, H., Yamada, S., 2012. Novel solid self-emulsifying drug delivery system of coenzyme Q(10) with improved photochemical and pharmacokinetic behaviors. European Journal of Pharmaceutical Sciences 46, 492-499.
Osborn-Barnes, H.T., Akoh, C.C., 2003. Effects of alpha-tocopherol, beta-carotene, and soy isoflavones on lipid oxidation of structured lipid-based emulsions. Journal of Agricultural and Food Chemistry 51, 6856-6860.

Sahu, A., Kasoju, N., Bora, U., 2008. Fluorescence Study of the Curcumin-Casein Micelle Complexation and Its Application as a Drug Nanocarrier to Cancer Cells. Biomacromolecules 9, 2905-2912.
Shaw, L.A., McClements, D.J., Decker, E.A., 2007. Spray-dried multilayered emulsions as a delivery method for omega-3 fatty acids into food systems. J Agr Food Chem 55, 3112-3119.
Sorensen, A.D.M., Haahr, A.M., Becker, E.M., Skibsted, L.H., Bergenstahl, B., Nilsson, L., Jacobsen, C., 2008. Interactions between iron, phenolic compounds, emulsifiers, and pH in omega-3-enriched oil-in-water emulsions. Journal of Agricultural and Food Chemistry 56, 1740-1750.
Tapal, A., Tiku, P.K., Complexation of curcumin with soy protein isolate and its implications on solubility and stability of curcumin. Food Chemistry 130, 960-965.
Tapal, A., Tiku, P.K., 2012. Complexation of curcumin with soy protein isolate and its implications on solubility and stability of curcumin. Food Chemistry 130, 960-965.
Tikekar, R.V., Johnson, A., Nitin, N., 2011. Fluorescence imaging and spectroscopy for real-time, in-situ characterization of interactions of free radicals with oil-in-water emulsions. Food Res Int 44, 139-145.
Tikekar, R.V., Nitin, N., 2011. Effect of physical state (solid vs. liquid) of lipid core on the rate of transport of oxygen and free radicals in solid lipid nanoparticles and emulsion. Soft Matter 7, 8149-8157.
Tikekar, R.V., Nitin, N., 2012. Distribution of encapsulated materials in colloidal particles and its impact on oxidative stability of encapsulated materials. Langmuir : the ACS journal of surfaces and colloids 28, 9233-9243.
Tong, L.M., Sasaki, S., McClements, D.J., Decker, E.A., 2000. Mechanisms of the antioxidant activity of a high molecular weight fraction of whey. Journal of Agricultural and Food Chemistry 48, 1473-1478.
Wang, X.Y., Jiang, Y., Wang, Y.W., Huang, M.T., Ho, C.T., Huang, Q.R., 2008. Enhancing anti-inflammation activity of curcumin through O/W nanoemulsions. Food Chemistry 108, 419-424.
Waraho, T., McClements, D.J., Decker, E.A., 2011. Mechanisms of lipid oxidation in food dispersions. Trends in Food Science & Technology 22, 3-13.
Watanabe, Y., Nakanishi, H., Goto, N., Otsuka, K., Kimura, T., Adachi, S., 2010. Antioxidative Properties of Ascorbic Acid and Acyl Ascorbates in ML/W Emulsion. Journal of the American Oil Chemists Society 87, 1475-1480.

Yuji, H., Weiss, J., Villeneuve, P., Lopez Giraldo, L.J., Figueroa-Espinoza, M.C., Decker, E.A., 2007. Ability of surface-active antioxidants to inhibit lipid oxidation in oil-in-water emulsion. Journal of Agricultural and Food Chemistry 55, 11052-11056.
Zimowska, W., Motyl, T., Skierski, J., Balasinska, B., Ploszaj, T., Orzechowski, A., Filipecki, M., 1997. Apoptosis and Bcl-2 protein changes in L1210 leukaemic cells exposed to oxidative stress. Apoptosis 2, 529-539.

LIST OF TABLES

LIST OF FIGURES

Table 1

Emulsion	Number based average diameter(μm)
Tween 20	0.11 ± 0.05
Lecithin	0.13 ± 0.07
Oxidized lecithin	0.15 ± 0.02

Table 2

Values in the parentheses represent 95% confidence interval. * For Tween 20 emulsion, the data was fitted to a mono-exponential decay.

Emulsions	a	b	c	R^2	1/e (h)
Lecithin	102.4(101.7-103)	1061(1045-1077)	4.4 (4.16- 4.77)	0.99	17.7
Tween 20	109.5(107-112)	488.5(470.1-506.9)	N/A*	0.99	8.14
Oxidized lecithin	100.2(99.38-101.1)	785.6(779.3-791.8)	2.3 (2.32- 2.49)	1.00	13.1

Solution	ORP (mV)		TBARS Absorbance Values at 532 nm
	0 min	120 min	
Lecithin Control (Not exposed to UV, only exposed to air)	186 ± 4.00	214 ± 2.08	0.01 ± 0.001
Lecithin Exposed to UV radiation*	189 ± 2.65	401 ± 5.50	0.30 ± 0.051

Table 3

* At 0 min, no UV treatment applied. Oxidized lecithin is in the form of native lecithin and represent the initial ORP value of lecithin solution.

Figure 1

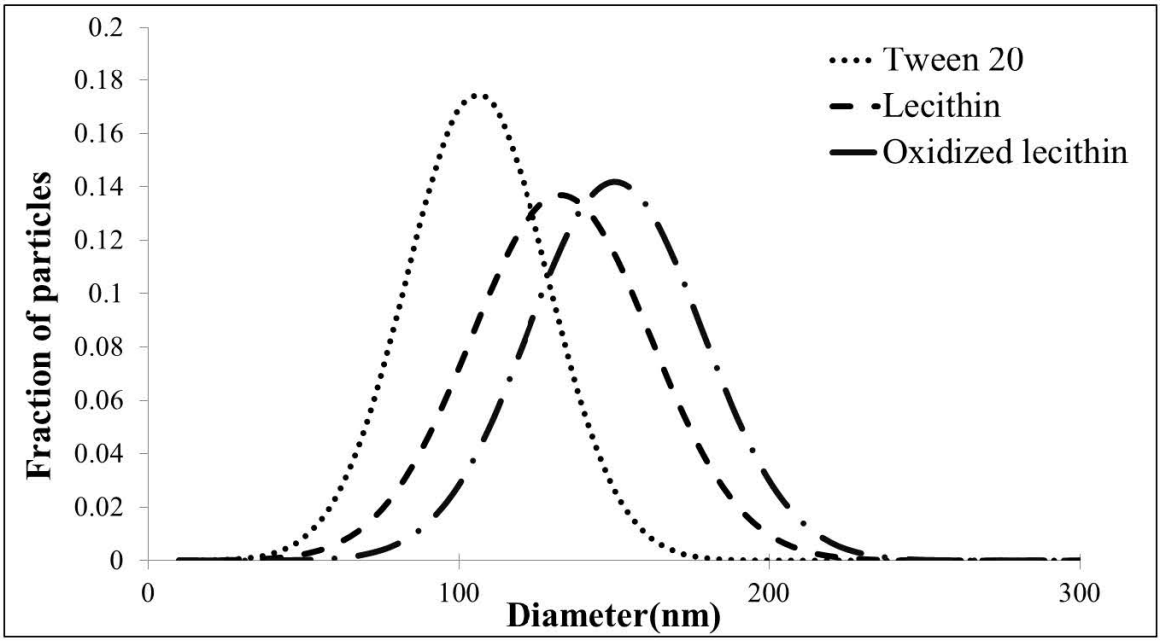
0.2
0.18
0.16
0.14
0.12
0.1
0.08
0.06
0.04
0.02
0
Fraction of particles
0
100
200
300
Diameter(nm)
Tween 20
Lecithin
Oxidized lecithin

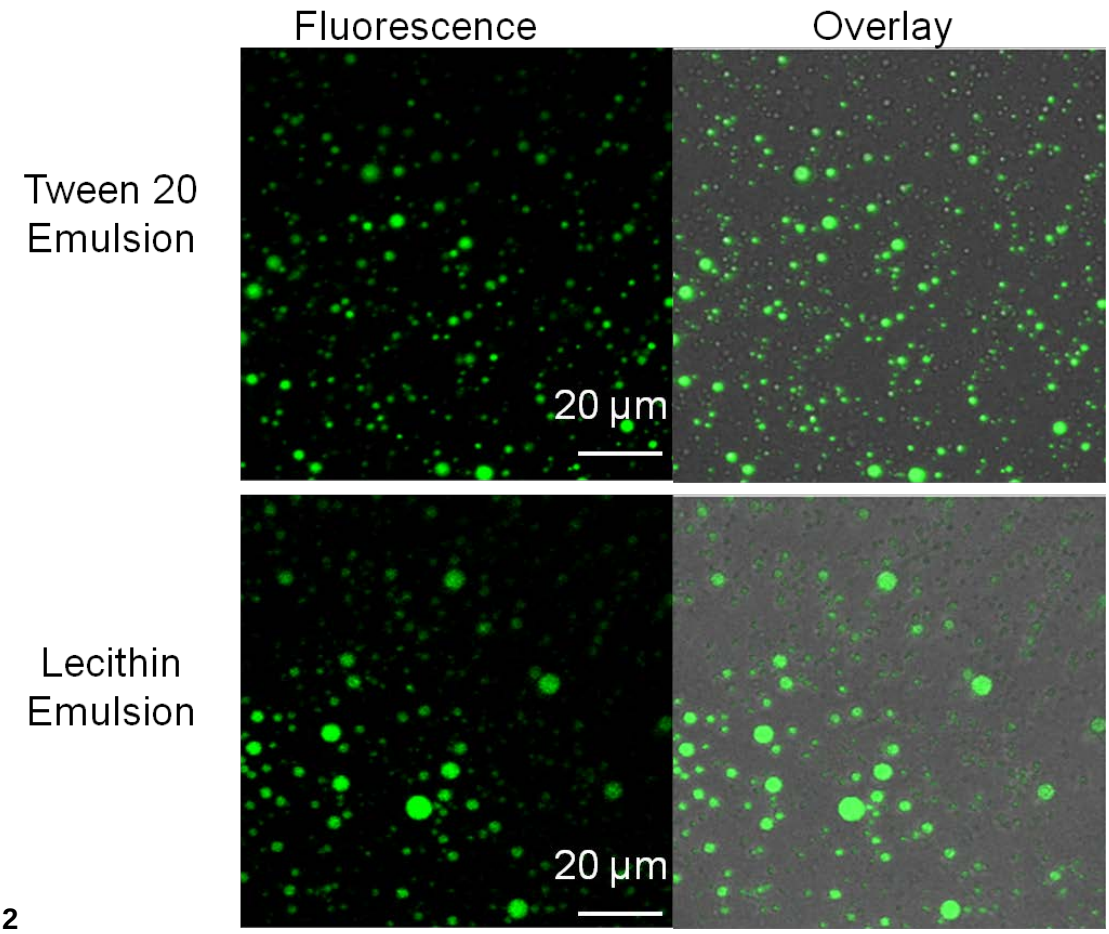
Fluorescence
Overlay
Tween 20
Emulsion
20 µm
Lecithin
Emulsion
20 µm

Figure 2

(a)

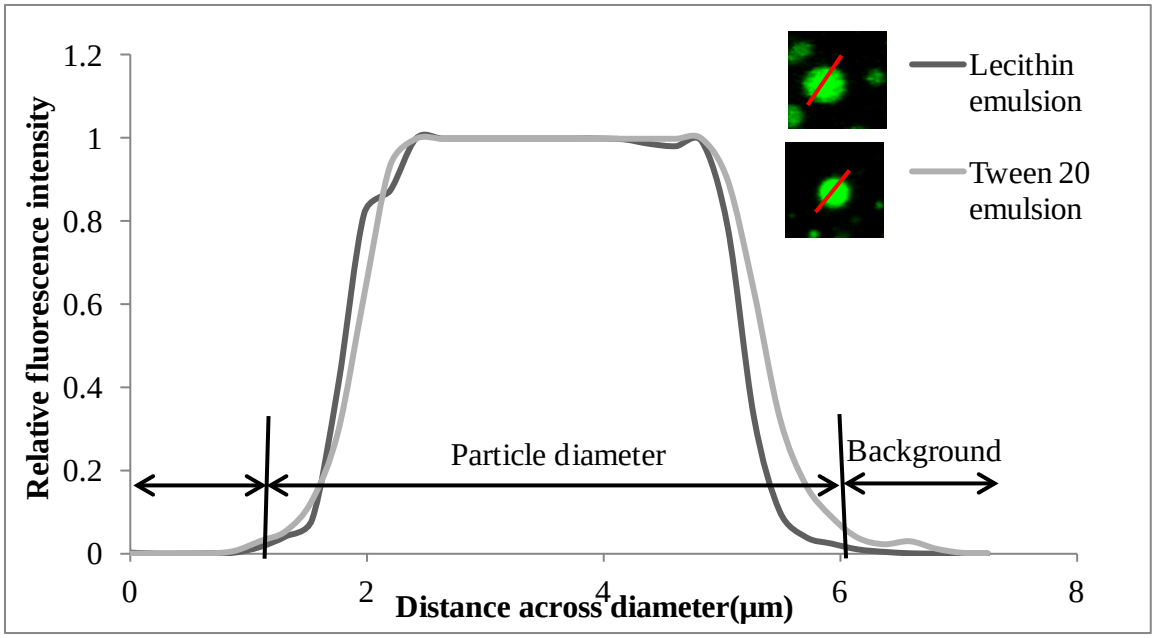
1.2
1
0.8
0.6
0.4
0.2
0
Relative fluorescence intensity
0
2
4
6
8
Distance across diameter(μm)
Particle diameter
Background
Lecithin emulsion
Tween 20 emulsion

(b)

Figure 3

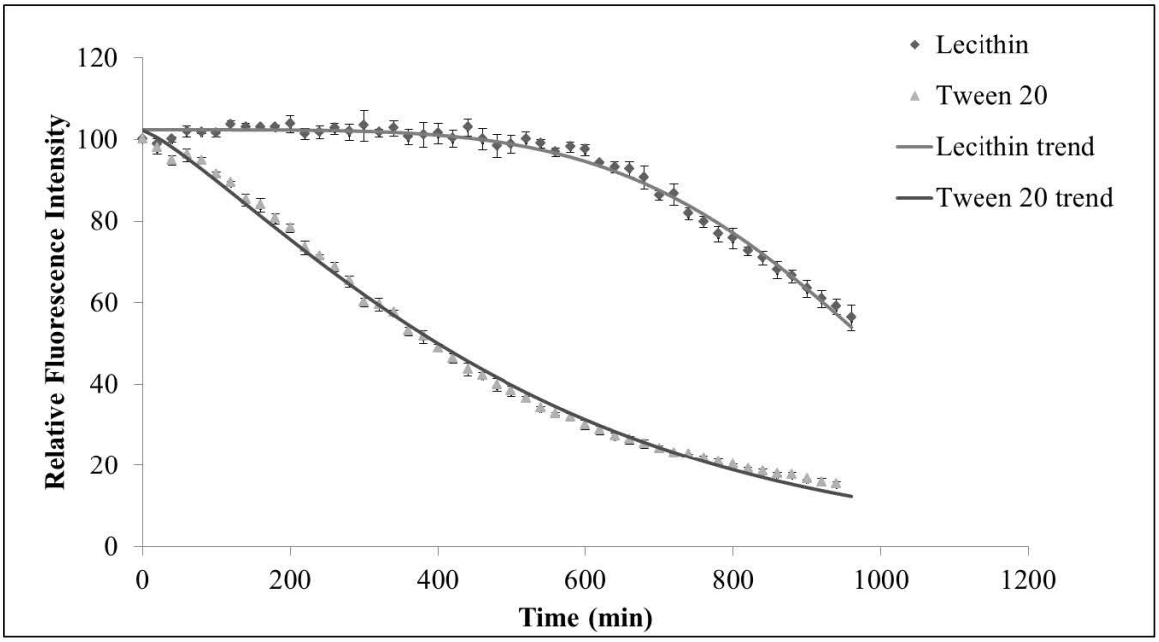
Lecithin
Tween 20
Lecithin trend
Tween 20 trend
Relative Fluorescence Intensity
120
100
80
60
40
20
0
0
200
400
600
800
1000
1200
Time (min)

Figure 4

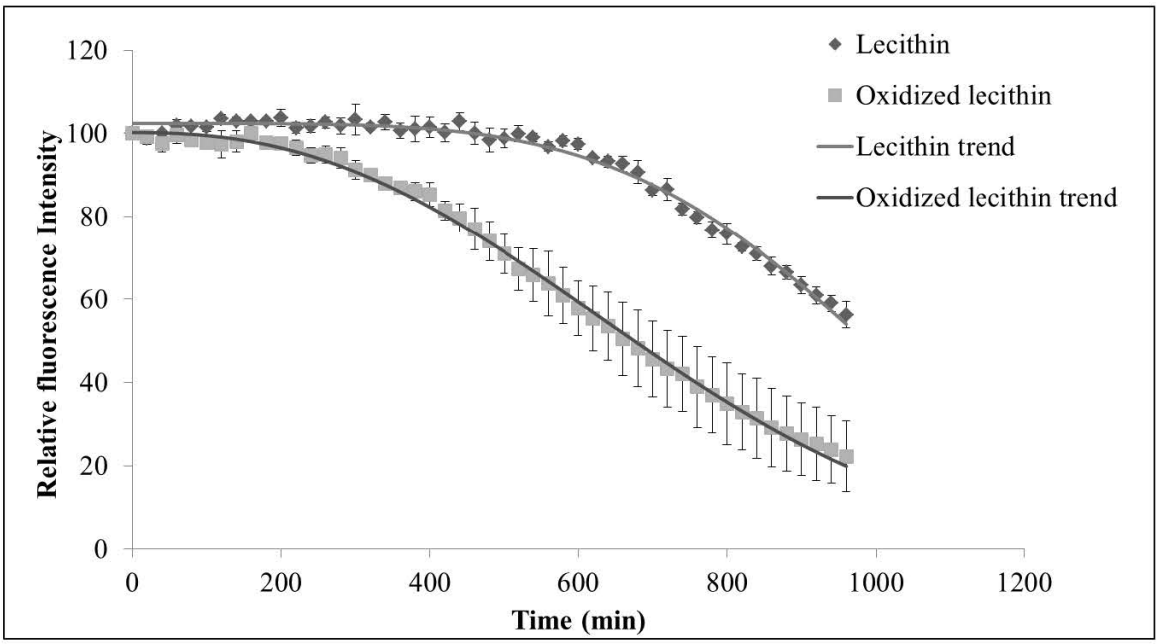

Figure 5

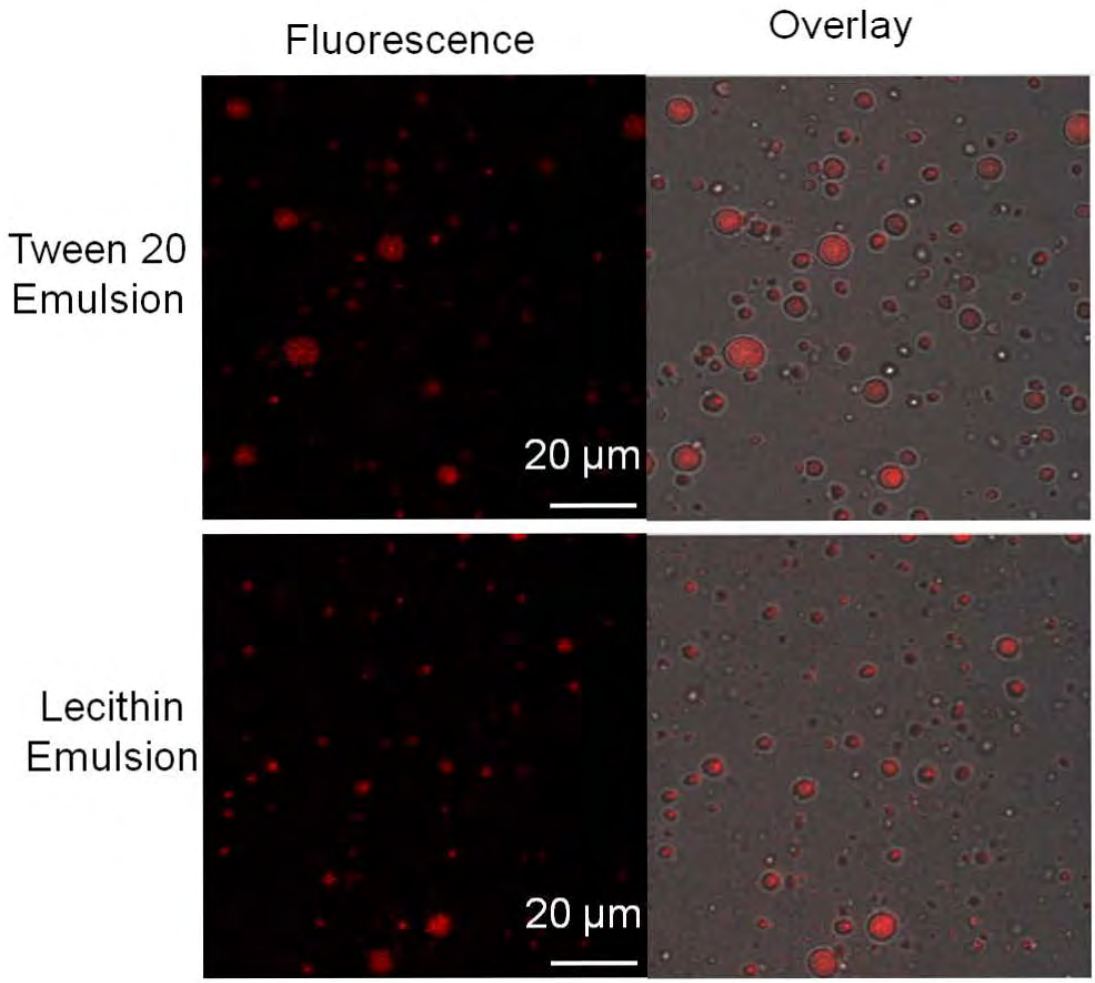
Fluorescence
Overlay
Tween 20
Emulsion
20 µm
Lecithin
Emulsion
20 µm

Figure 6

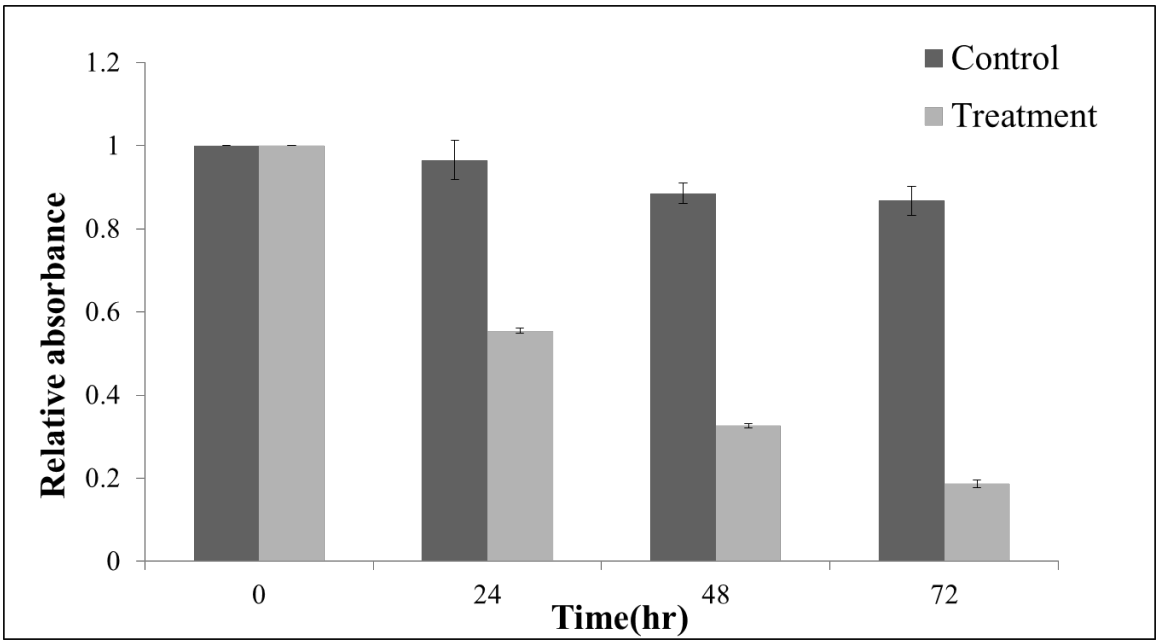
Control
Treatment
Relative absorbance
1.2
1
0.8
0.6
0.4
0.2
0
0
24
48
72
Time(hr)

(a)

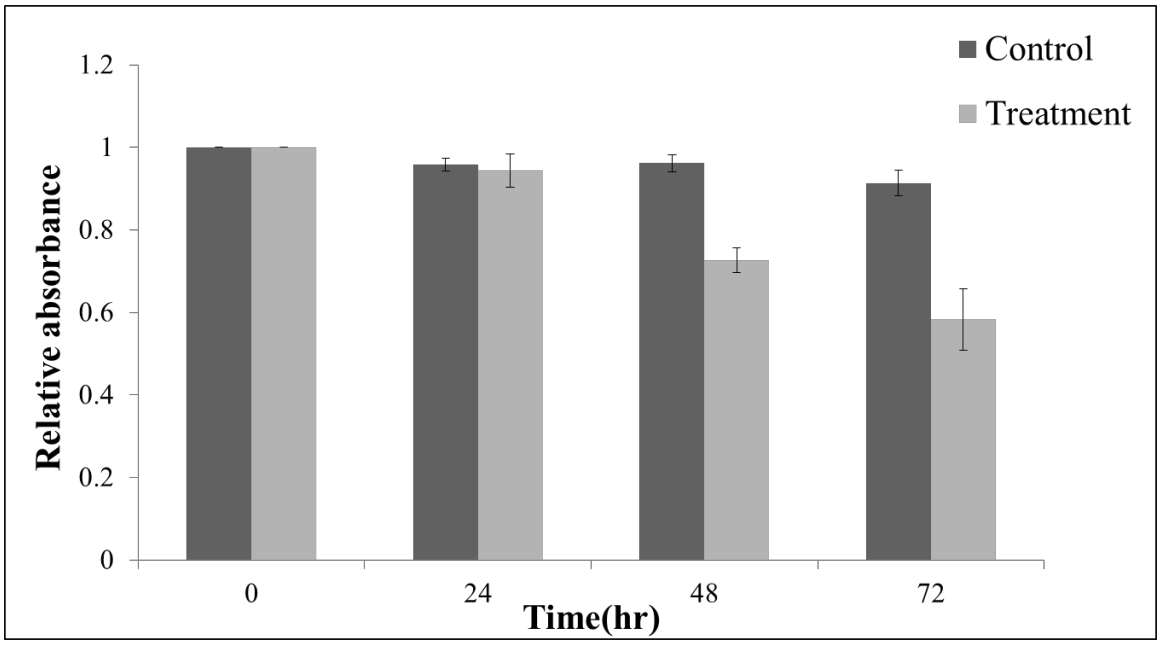
Control
Treatment
Relative absorbance
1.2
1
0.8
0.6
0.4
0.2
0
0
24
48
72
Time(hr)

(b)

Objective IV: Role of protein core design in influencing oxidation of encapsulated bioactives.

Key Results:

- **Zein particles provide a significantly improved barrier to oxidation as compared to emulsions**
- **The rate of oxygen diffusion in zein particles is not significantly higher than the emulsion core itself, indicating the porosity of the protein core was sufficient for oxygen diffusion**
- **The rate of radical permeation in zein particles was significantly slower than the emulsion lipid core**

DETAILED REPORT

MATERIALS AND METHODS

Materials

Casein sodium salt, from bovine milk, sodium azide, 2,2'-azobis-2-methylpropanimidamide dihydrochloride (AAPH), organic canola oil, tris (4,7-diphenyl-1,10-phenanthroline) ruthenium(II) bis (hexafluorophosphate) complex for measuring oxygen transport across nanoparticle or emulsion barriers and curcumin from *Curcuma longa* (Turmeric) were obtained from Sigma-Aldrich (St Louis, MO). Ethanol, dimethyl sulfoxide (DMSO) and acetone were purchased from Fisher Scientific (Pittsburgh, PA). Ultrapure water (16MΩ-cm) was obtained from in-house water filtration system. A peroxyl radical sensitive dye, BODIPY®665/676 dye was purchased from Invitrogen Incorporated (Carlsbad, CA).

Synthesis of Zein nanoparticles for measurement of oxygen and peroryl radical transport

4 g of casein was dissolved in 200 mL of distilled water. 1 g of zein protein powder was solubilized in 50 mL of 80% ethanol. To this ethanolic solution of zein, either 300 µL of BODIPY 665/676 dye prepared in acetone (0.5 mg/mL) or Ruthenium based oxygen sensitive dye prepared in DMSO (1 mg/mL) was mixed. The zein solution was added to the casein solution drop-wise (5 mL/minute) under vigorous stirring (4000 rpm) followed by coarse homogenization using hand held disperser operating at 9000 rpm for 2 minutes (Ultra-Turrax model T25, IKA Works, Wilmington, NC). The coarse dispersion was subsequently passed eight times through a single stage homogenizer operating at 800 bar. The resultant solution was heated at 60 °C for

45 minutes to evaporate ethanol and facilitate nanoparticle formation. The nanoparticle solution was centrifuged at 10,000 rpm for 1 hour to precipitate coarse particles and agglomerates. The nanoparticle solution was added with 0.5% sodium azide and stored at 4 °C until further use.

Preparation of casein emulsions for measurement of oxygen and peroxyl radical transport

4 g of casein was dissolved in 200 mL of distilled water. 8 g of canola oil was solubilized with either 200 µL of BODIPY 665/676 dye prepared in acetone (0.5 mg/mL) or Ruthenium based oxygen sensitive dye prepared in DMSO (1 mg/mL). Emulsion premix was formed using hand held disperser operating at 9000 rpm for 2 minutes (Ultra-Turrax model T25, IKA Works, Wilmington, NC). This premix was passed through a single stage homogenizer operating at 800 bar five times to obtain stable emulsion. The emulsion was incorporated wit 0.5% sodium azide and stored at 4 °C until further use.

Size Characterization of nanoparticles and emulsion

The hydrodynamic sizes of zein nanoparticles and casein emulsions were measured using a particle size analyzer (Model: Malvern Nano Series, Malvern Instruments, Inc., Westborough, MA). The settings for the analyzer were- material type: protein, particle refractive index=1.45, for zein nanoparciles and oil, particle refractive index = 1.45, for casein emulsions, dispersant type: water, dispersant refractive index= 1.33, temperature: 25 °C. Particle size measurements were analyzed based on the number average particle size distribution.

Morphological analysis

Morphology and surface appearance of zein nanoparticles were examined using a Transmission Electron Microscope (SEM). A drop (6 µL) of zein nanoparticle samples were added onto a carbon coated TEM grid (400 mesh, Ted Pella, Redding CA) and incubated at room temperature for 10 min. After 10 min, the excess liquid was wicked away using a piece of filter paper, and 8 µL of 1% sodium phosphotungstate was added to the TEM grid and wicked away immediately to negative stain the sample. The TEM grid was allowed to dry in air for an additional 10 min prior to imaging. TEM images of the samples were viewed and acquired using a Philips CM120 Biotwin TEM, (FEI Company, Hillsboro, OR, USA) at 80kV for low magnification, and 100kV at 200,000X magnification in order obtain image of one particle. All TEM work was performed in the Electron Microscopy Laboratory in the Department of Medical Pathology and Laboratory Medicine at the University of California, Davis.

Fluorescence imaging of encapsulated BODIPY dye in zein nanoparticles

Fluorescence images were obtained to demonstrate that the BODIPY dye was uniformly distributed in zein nanopartilces. It was difficult to visualize and measure the distribution of the dye in zein nanoparticles due to their small droplet size (around 100 nm) based on their fluorescence intensity. To overcome this limitation, coarse emulsion with the same proportions of oil and aqueous phase was prepared using a hand-held disperser. Confocal microscopy was conducted using a Zeiss LSM 510 Meta confocal microscope. Confocal imaging of zein nanoparticles was obtained using a 63× oil objective with a numerical aperture (NA) of 1.4. The images of samples encapsulating the BODIPY dye (as described above) were obtained using a 633 nm laser excitation. The emission signal was detected using a Meta detector. The Meta spectrometric detector integrated the fluorescence emission signal between the wavelengths of 660 and 710 nm.

Measurement of peroxyl radical transport

Peroxyl radicals were generated in the aqueous phase of zein nanoparticles and casein emulsion using AAPH. 40 mM AAPH was dissolved in ultrapure water. 1 mL of nanoparticles or emulsion sample was then mixed with 1 mL of AAPH solution to achieve a final concentration of 20 mM AAPH. Immediately after addition of AAPH, the samples were placed in the plate-reader (Spectramax M5, Molecular Devices, Carlsbad CA) and fluorescence intensity was measured at a regular time interval of 20 minutes for a total time period of 20 hours. Nanoparticles and emulsion samples mixed with equal volume of ultrapure water were used as controls. The excitation and emission wavelengths for fluorescence measurements were 620 nm and 675 nm, respectively. The relative fluorescence intensity was calculated using Eq. (3)-

$$\boldsymbol{Relative\ fluorescence\ intensity} = \frac{\frac{\boldsymbol{I_{t\ AAPH}}}{\boldsymbol{I_{0\ AAPH}}}}{\frac{\boldsymbol{I_{t\ control}}}{\boldsymbol{I_{0\ control}}}} \times \mathbf{100} \qquad (\mathbf{3})$$

Where, $I_{t\ AAPH}$= Fluorescence intensity of sample after 't' minutes of exposure to AAPH, $I_{0\ AAPH}$= Fluorescence intensity of sample immediately after addition of AAPH, $I_{t\ control}$= Fluorescence intensity of control sample after time 't' minutes, $I_{0\ control}$= Fluorescence intensity of control sample at time t=0 minute. The data was normalized with respect to the relative fluorescence of control samples in order to account for changes in fluorescence intensity induced by evaporation during the course of measurement (~20 hours). The changes in fluorescence

intensity were fit to an exponential model of the form $y = ae^{-\left(\frac{x}{b}\right)^c}$ using Matlab CFTool 2012. A non-linear regression model with "Trust Region" algorithm was used for fitting the data.

Measurement of oxygen transport

After homogenization, nanoparticles and emulsion samples were transferred to three aluminum foil wrapped plastic bottles (5 mL each) and purged with nitrogen for three hours to remove traces of air. Efficient removal of oxygen provides a large dynamic range to measure changes in fluorescence upon exposure to oxygen. After purging, the samples were exposed to atmosphere by pipetting 200 µL of sample/well in a 96 well black costar plate optimized for fluorescence measurement. Nanoparticles and emulsion samples were exposed to ambient air within a plate reader. Loss in fluorescence intensity as a result of exposure to atmospheric oxygen was measured using a plate-reader (Model: M5, Molecular Devices, Carlsbad CA). The excitation and emission settings for the plate- reader were 485 nm and 615 nm respectively. The plate-reader was set at 23 °C for both nanoparticles and emulsion samples. Changes in fluorescence intensity as a function of time were recorded at a regular interval of 15 s for 10 minutes. The relative fluorescence intensity was calculated using the following equation-

$$\boldsymbol{Relative\ fluorescence\ intensity} = \frac{(\boldsymbol{I_t} - \boldsymbol{I_\infty})}{(\boldsymbol{I_0} - \boldsymbol{I_\infty})} \times \mathbf{100} \qquad (\mathbf{4})$$

Where, I_t= Fluorescence intensity at time 't' s after exposure to atmospheric oxygen I_∞= Fluorescence intensity at equilibrium oxygen concentration, I_0= Fluorescence intensity in the absence of oxygen (nitrogen purged sample at t= 0 s).

Measurement of diffusion coefficient for oxygen

The effective diffusion coefficient was calculated based on the following equations (Kaptan et al., 1989). Based on the Fick's second law of diffusion for a spherical geometry, the ratio of concentration (C_t/C_0) is given by-

$$\frac{\boldsymbol{C_t}}{\boldsymbol{C_0}} = \mathbf{1} + \frac{\boldsymbol{2a}}{\boldsymbol{\pi r}} \sum_{\boldsymbol{n=1}}^{\boldsymbol{\infty}} \frac{\boldsymbol{(-1)^n}}{\boldsymbol{n}} \times \boldsymbol{sin}\frac{\boldsymbol{n\pi r}}{\boldsymbol{\alpha}} \mathbf{exp}\left(-\frac{\boldsymbol{Dn^2\pi^2 t}}{\boldsymbol{\alpha^2}}\right) \qquad (5)$$

Where α is the radius of sphere; D, the effective diffusion coefficient and C_0 and C_t are concentration of oxygen at time t=0 and t seconds respectively; *r* corresponds to radial distance

at which *C* is measured. Upon integration of equation-5 over volume *dV,* the resulting equation becomes-

$$\frac{M_t}{M_\infty} = 1 - \frac{6}{\pi^2}\sum_{n=1}^{\infty}\frac{1}{n^2}\exp\left(-\frac{Dn^2\pi^2 t}{\alpha^2}\right) \quad (6)$$

Where, *M* represents the total flux at any given time in a spherical geometry and can be calculated using following expression-

$$M = \int C dV \quad (7)$$

Equation 6 was further simplified using a concept of $t_{1/2}$, (time required to uptake 50% of the equilibrium concentration of oxygen). The resulting equation after truncation of second order terms simplifies to-

$$t_{1/2} = 0.0717\alpha^2/D \quad \textbf{(8)}$$

To calculate M_t/M_∞, Stern-Volmer equation was used.

$$\frac{I_0}{I_t} - 1 = [O_2] \quad (9)$$

Thus M_t and M_∞ can be obtained as-

$$M_t = \left(\frac{I_0}{I_t} - 1\right) \text{ and } M_\infty = \left(\frac{I_0}{I_\infty} - 1\right)$$

Therefore, $\frac{M_t}{M_\infty} = \frac{(I_0 - I_t)I_\infty}{(I_0 - I_\infty)I_t}$ (10)

Where, I_o=Fluorescence intensity under nitrogen, I_t=Fluorescence intensity after t seconds of exposure to air, and I_∞= Fluorescence intensity of air purged control sample.

This ratio (equation 10) was plotted as a function of time, and $t_{1/2}$ was calculated by mathematical interpolation. An average effective diffusion coefficient was calculated for each of the emulsions based on the average $t_{1/2}$ value and the measured diameter of emulsion droplets. In this analysis, following assumptions were made - (1) the effective diffusion coefficient is constant; (2) the aggregate data of fluorescence measurement using a plate reader represents the fluorescence quenching trend within an individual droplet. This assumption was validated based on imaging measurements of changes in fluorescence of individual emulsion droplets

upon exposure to oxygen and (3) the diffusion through a droplet is not affected by presence of surrounding droplets i.e. there is no inter-droplet interactions due to low concentration of oil (2.5 %).

Porosity measurement

Porosity was calculated according to $= 1 - \frac{\rho_b}{\rho_p}$, where P is the porosity, ρ_b is the bulk density of zein and ρ_p is the particle density.

Curcumin stability in zein nanoparticles and casein emulsions

Zein nanoparticels and casein emulsions encapsulating curcumin were prepared using the same experimental approach as described for the samples encapsulating a radical sensitive dye. Curcumin was added to ethanol or oil to achieve a final concentration of 6.9 mg/ mL ethanol or 200 µg/g oil. Concentration of curcumin was selected based on the solubility limit of curcumin in ethanol and oil. Oxidative stability of encapsulated curcumin was measured by characterizing changes in absorbance of curcumin as a function of incubation time. Emulsions containing encapsulated curcumin were incubated with and without 10 mM AAPH at 22 °C in dark for 24 hours. To measure curcumin concentration, emulsions were disrupted by adding 1 mL acetone to 200 µL zein nanoparticles or casein emulsion. The mixture was centrifuged at 14000 g for 10 min. 1mL of the supernatant was placed in a cuvette and the absorbance was measured at 425 nm using a UV-Visible spectrophotometer (GENESYS 10S Series, Thermo Scientific). A blank sample was prepared using 1 mL acetone and 200 µL ultrapure water.

RESULTS AND DISCUSSION

Particle size measurements and morphology

Table 1 shows the mean particle diameter for zein nanoparticles and casein emulsion. The average particle size for zein nanoparticles (104.9 nm) was smaller than that for casein emulsion (204 nm). **Figure 1** shows the TEM images of zein nanoparticles at two separate magnifications. Imaging results suggested that zein nanoparticles were uniformly spherical in shape and did not agglomerate after synthesis. Stability of zein nanoparticles and emulsion samples was also evaluated during storage (2 weeks). The average particle size of zein nanoparticles and casein emulsion did not change after 2 weeks (data not shown) indicating that these encapsulation systems were stable.

Peroxyl radical permeation across zein nanoparticles and casein emulsion

The efficacy of zein nanoparticles and emulsions in limiting oxidation processes was compared by measuring the permeation of free radicals from the aqueous phase to the core of zein nanoparticles and emulsions. Permeation of peroxyl radicals from the aqueous phase to the oil phase of emulsions was measured based on changes in fluorescence intensity of peroxyl radical sensitive dye encapsulated in the organic phase of zein nanoparticles and emulsions. This approach has been successfully used in our prior studies to measure the influence of lipid core design and the interfacial composition on the rate of permeation of peroxyl radicals across emulsions, nanoparticles and lipid bi-layers. The selected BODIPY dye is highly hydrophobic and has high specificity to react with peroxyl radicals and upon reaction with peroxyl radicals, fluorescence intensity of the dye is quenched.

Prior to real time measurement of interactions of free radicals with the encapsulated dye, spatial distribution of peroxyl radical sensitive BODIPY dye encapsulated within the core of zein nanoparticles was characterized using fluorescence imaging of zein nanoparticles (**Figure 2). I**t is evident that the dye was uniformly distributed in the core of zein nanoparticles with no significant partitioning of the dye in the aqueous phase of emulsions. This imaging data demonstrates that the selected dye is hydrophobic with no significant solubility in the aqueous phase.

Peroxyl free radicals in the aqueous phase were generated using AAPH. Due to relatively long half-life (approximately 175 hours) of APPH in aqueous solution (Zimowska et al., 1997), the rate of generation of peroxyl radicals can be maintained constant for an extended duration of time. **Figure 3(a)** and **3(b)** show the rate of fluorescence decay of BODIPY 665/676 dye (peroxyl radical sensitive dye) upon exposure to 10 mM (**Figure 3(a)**) and 20 mM (**Figure 3(b)**) AAPH dissolved in the aqueous phase. At 10 mM AAPH level, there was a significant difference in the percentage fluorescence decay between zein nanoparticles and casein emulsion. After 20 hours of incubation, the relative fluorescence intensity for zein nanoparticles was close to 100%, while for casein emulsion the relative fluorescence decreased to approximately 35%. At 20 mM AAPH level, the relative fluorescence of zein nanoparticles remained close to 100% for 540 minutes after which the fluorescence decreased steadily to 31% after 20 hours of incubation. However, casein emulsion showed a steady decline in relative fluorescence and the value was approximately 2% after 20 hours of incubation. To quantify differences in the decay of relative fluorescence intensity between zein nanoparticles and casein emulsions, the experimental data was fitted to a generalized exponential function of the form $y = ae^{-\left(\frac{x}{b}\right)^c}$, where a is the initial intensity of fluorescence, b is the constant describing the

rate of decay, and c is the shape parameter. The results of the curve fitting analyses are shown in **Table 2**. Quantitative comparison of the kinetic measurements show that the time required for an exponential decay (1/e) in fluorescence intensity is approximately 2 fold higher in zein nanoparticles (~18.43 hours) as compared to casein emulsion (~8.24 hours). Together these results showed that at a given rate of peroxyl radical generation, the rate of fluorescence loss in zein nanoparticles was significantly lower than that in casein emulsion. These results indicate that zein nanoparticles possess significantly higher barrier properties than casein emulsion. Since both casein emulsion and zein nanoparticles are surface covered with casein particles, the higher barrier property of zein nanoparticles could be attributed to difference in the core structure of zein nanoparticles and emulsion droplets. In zein nanoparticles, the core consisted of precipitated zein polymers that can form significantly compact and tight structure. The compactness of structure in these particles is evident from significantly low particle size as compared to casein emulsion droplets. On the other hand, the core of casein emulsion consisted of liquid lipid with significantly higher mobility than precipitated zein and therefore significantly increases the rate of free radical transport. It has been reported that zein finds many potential applications in food industries as an antioxidant. The antioxidant properties of zein can also be responsible to slow down the rate of permeation of peroxyl radicals. Based on the free radical transport measurements, it is possible that zein nanoparticles can significantly enhance the oxidative stability of encapsulated materials as compared to emulsion based encapsulation system. It is important to note that other experimental parameters such as pH, temperature, concentration of emulsifier were maintained constant between zein nanoparticles and casein emulsions.

Oxygen transport across zein nanoparticles and casein emulsion

Figure 4 shows the rate of loss of fluorescence for oxygen sensitive dye encapsulated within nitrogen purged zein nanoparticles and casein emulsion upon exposure to atmospheric oxygen. Based on these plots it is evident that in both the samples the fluorescence decreased rapidly and after 15 minutes of exposure to atmospheric oxygen the relative fluorescence had reached 0% indicating that oxygen concentration inside the encapsulation system was in equilibrium with that in the aqueous phase and atmosphere. The fluorescence decay rate was marginally but significantly ($p<0.05$) lower for zein nanoparticles than casein emulsion. The diffusion coefficients for oxygen transport across the interface of zein nanoparticles and casein emulsion were calculated using the approach discussed in materials and methods section. The average diffusion coefficient for oxygen transport in zein nanoparticles and casein emulsion

were 3.48×10^{-19} m^2/s and 2.22×10^{-18} m^2/s, respectively. The results are similar to the diffusion coefficients of oxygen in SDS emulsion (1.16×10^{-18} m^2/s) and whey protein emulsion (1.4×10^{-19} m^2/s). However, this difference did not have a meaningful impact since in both the samples oxygen transport was very rapid and equilibrium conditions reached in approximately 15 minutes. These results suggest that neither zein nanoparticles nor casein emulsion were capable of significantly reducing the oxygen transport rate across the interface.

It is well known that nanoparticle preparation by solvent evaporation is a complex process in which the organic solvent generates pores in the structure during its evaporation. This may lead to changes in the structure of nanoparticles significant enough to affect their physical properties. The porosity of zein nanoparticles was calculated to be 0.78 using the method discussed in materials and methods section. Great value of porosity indicates the porous nature of zein nanoparticles formed in this study and the porous structure of zein nanoparticles can significantly affect the rate of oxygen transport. It may explain the large diffusion coefficient for oxygen transport in zein nanoparticles.

Stability of curcumin in zein nanoparticles and casein emulsions

Impact of structural differences between colloidal particles and emulsions on stability of encapsulated curcumin (a model bioactive susceptible to oxidation) was evaluated. Results in **Figure 5(a)** compare stability of curcumin in 10 mM AAPH treated and control casein emulsions. The results show that about 78% of the encapsulated curcumin degraded in AAPH treated casein emulsion after 20 hours of incubation. In contrast, there is no significant curcumin degradation in the control casein emulsion (without AAPH treatment) during the same incubation time. Results in **Figure 5(b)** compare stability of curcumin in AAPH treated and control zein nanoparticles. During the 20 hours of incubation, no significant degradation of encapsulated curcumin was observed in AAPH treated zein nanoparticles ($p>0.05$). These differences in the rate of degradation of curcumin between zein nanoparticles and casein emulsions follow a similar trend as the differences in the rate of permeation of free radicals in these emulsions (**Figure 3(a)**). These results demonstrate that zein nanoparticles were more effective in limiting oxidative degradation of encapsulated curcumin as compared to casein emulsion upon exposure to AAPH. It is important to note that AAPH treatment of samples simulates an accelerated oxidative stability analysis of encapsulated bioactives. The time required for inducing oxidation in emulsions using the AAPH approach in this study is similar to the results of a previous study (Watanabe et al., 2010). These results validate that structural

differences between colloidal particles and emulsions can significantly influence oxidative degradation of encapsulated bioactives.

Table 1

Samples	Number based average diameter(nm)
Zein nanoparticles	104.9 ± 0.115
Casein emulsion	204.0 ± 7.00

Samples	a	b	c	R^2	1/e (h)

Table 2

Casein emulsion	102.5(100.1-104.9)	494.5(483.8-505.3)	2.315 (2.151- 2.48)	0.99	8.24
Zein nanoparticles	98.77(97.69-99.85)	1106(1095-1117)	4.618 (4.301- 4.936)	0.99	18.43

Values in the parentheses represent 95% confidence interval.

Figure 1

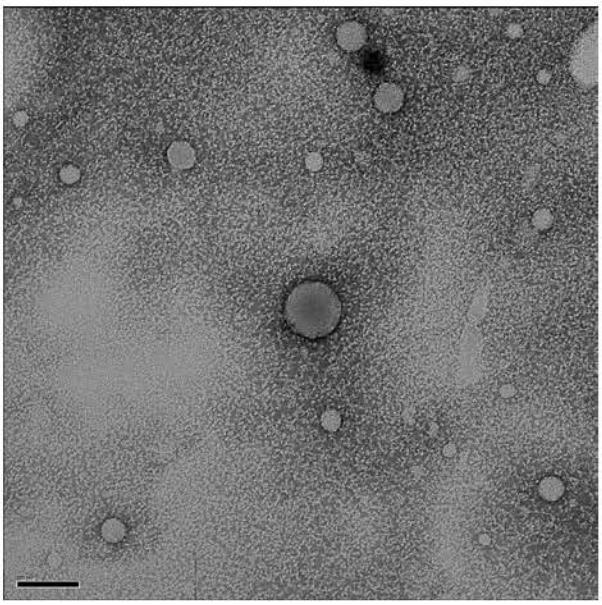

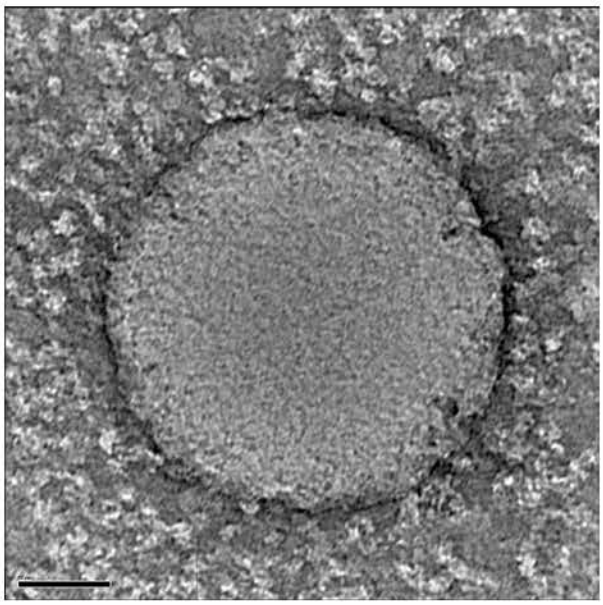

Figure 2

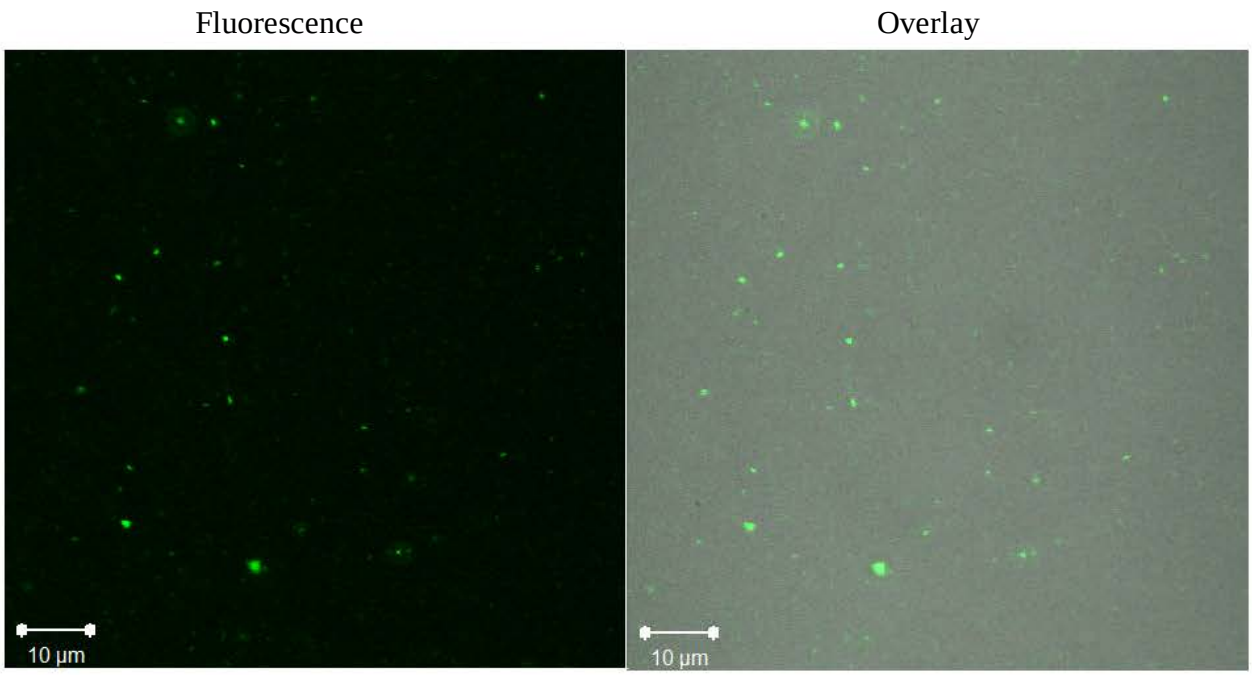

Figure 3

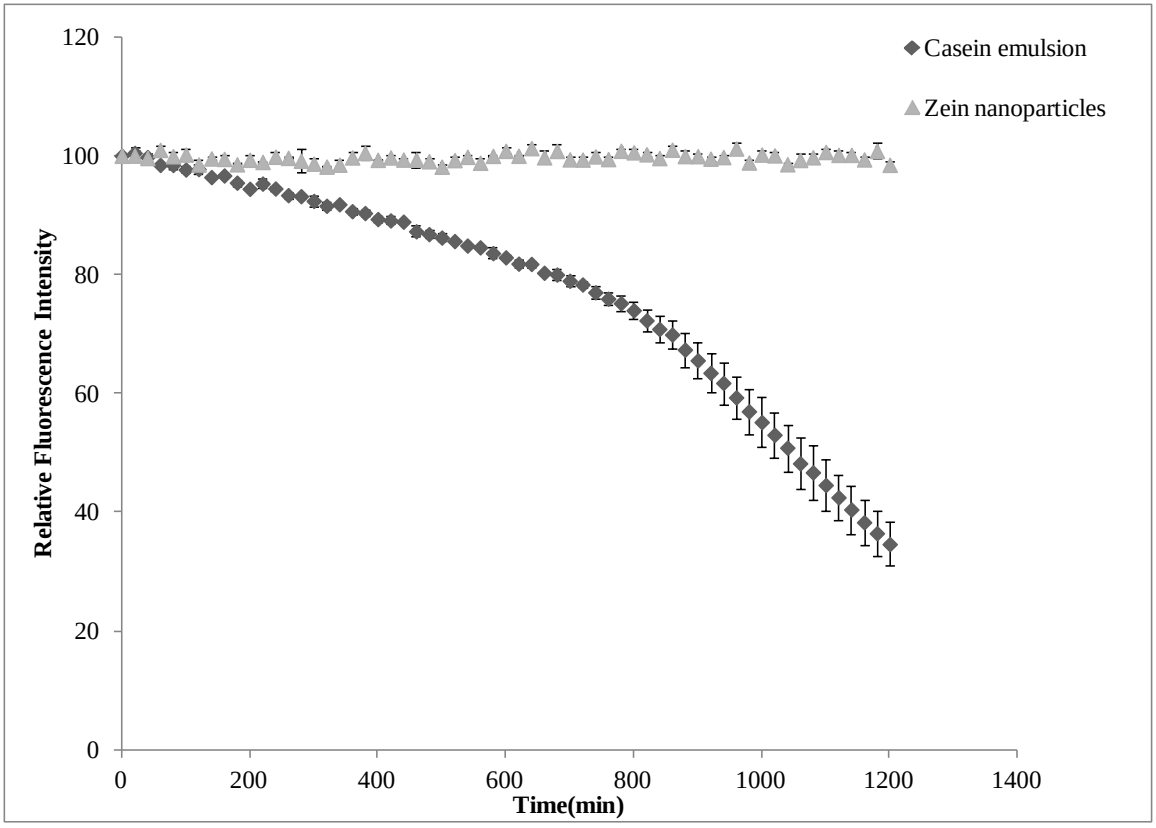
120
100
80
60
40
20
0
0
200
400
600
800
1000
1200
1400
Relative Fluorescence Intensity
Time(min)
Casein emulsion
Zein nanoparticles

(a)

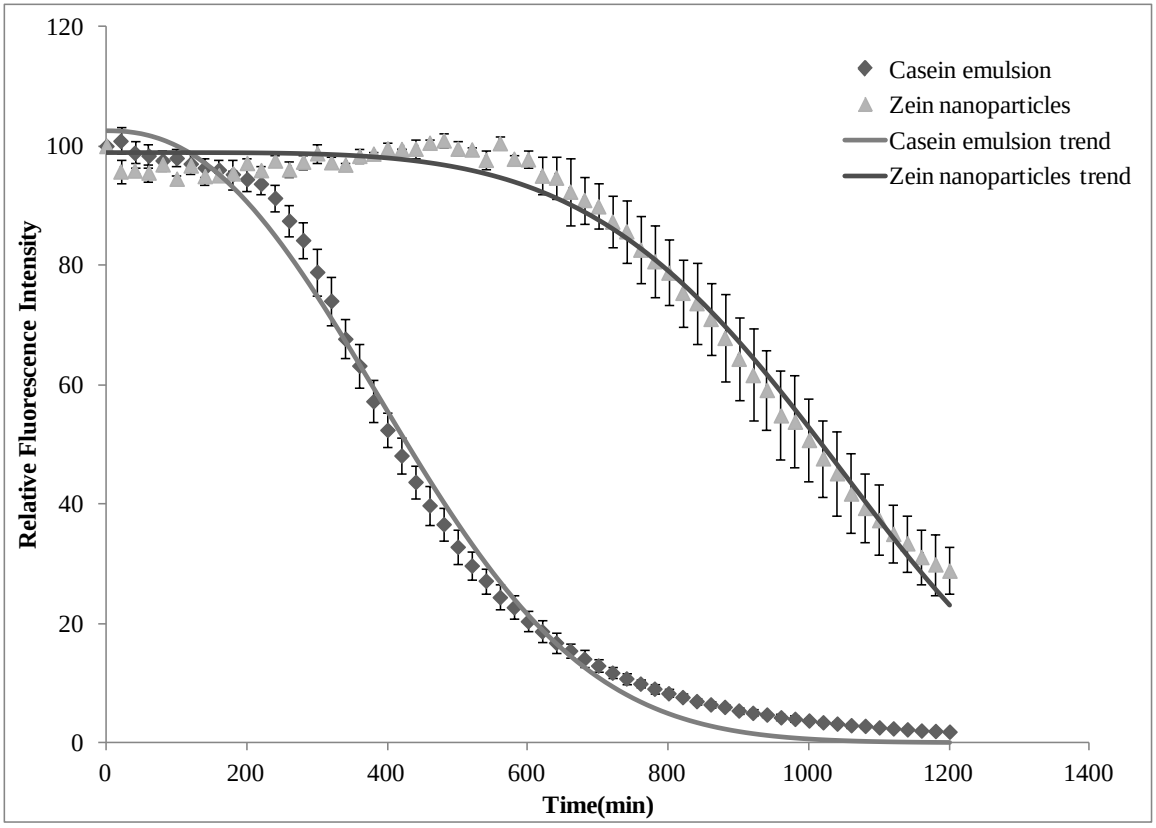
120
100
80
60
40
20
0
Relative Fluorescence Intensity
0
200
400
600
800
1000
1200
1400
Time(min)
Casein emulsion
Zein nanoparticles
Casein emulsion trend
Zein nanoparticles trend

(b)

Figure 4

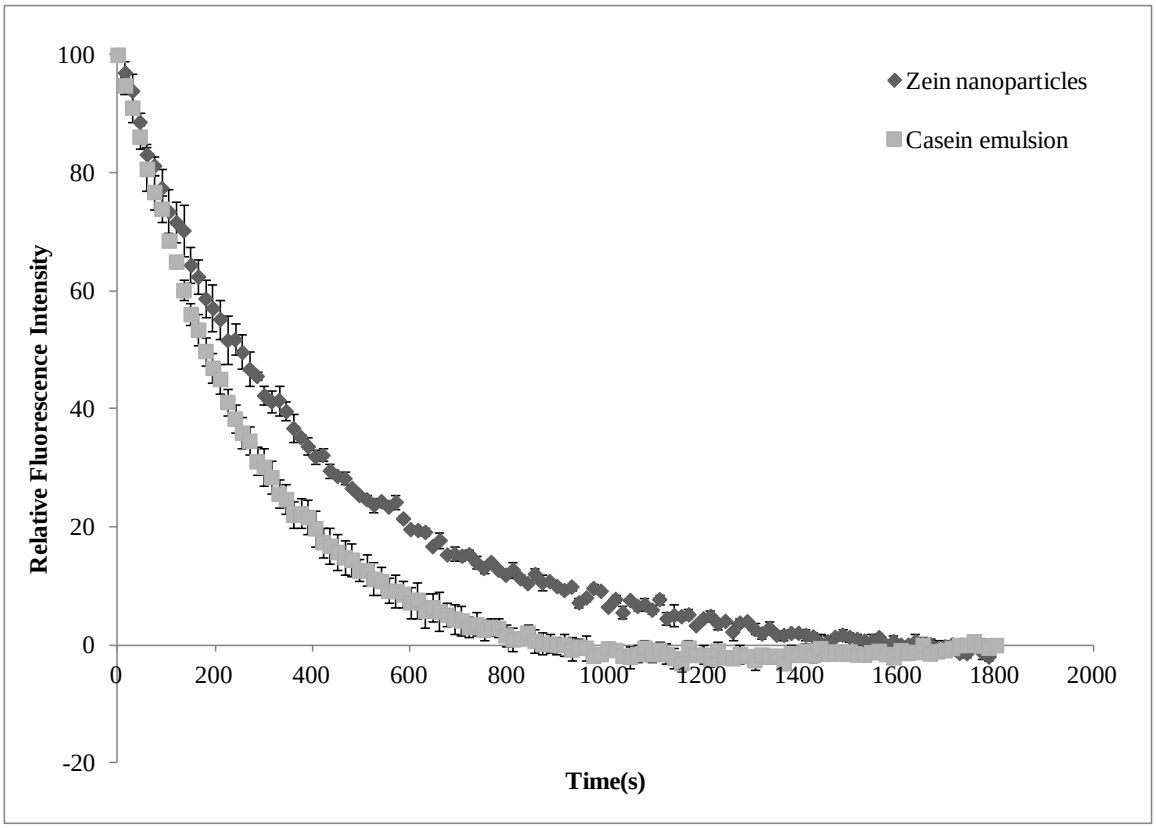
100
80
60
40
20
0
-20
0
200
400
600
800
1000
1200
1400
1600
1800
2000
Relative Fluorescence Intensity
Time(s)
Zein nanoparticles
Casein emulsion

Figure 5

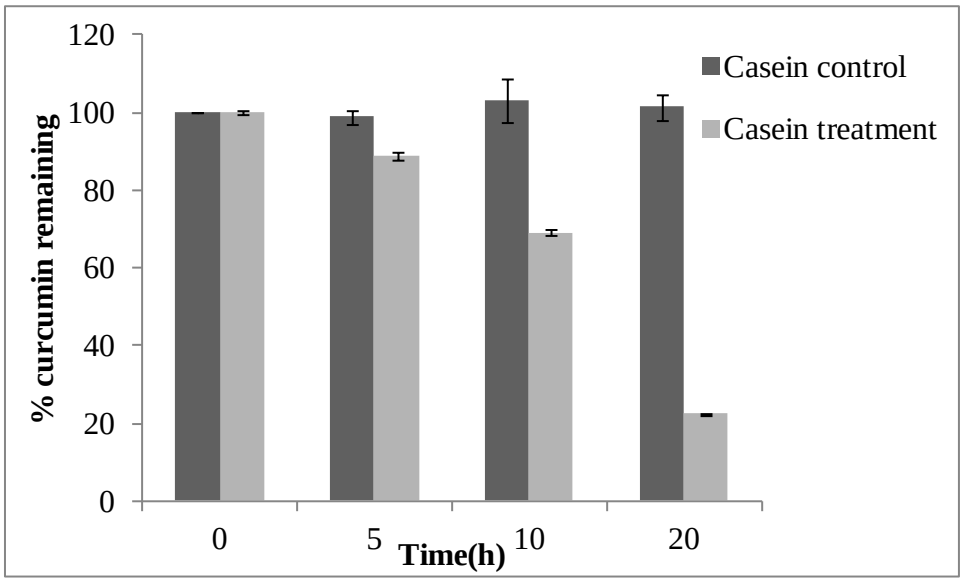
120
100
80
60
40
20
0
% curcumin remaining
0
5
10
20
Time(h)
Casein control
Casein treatment

(a)

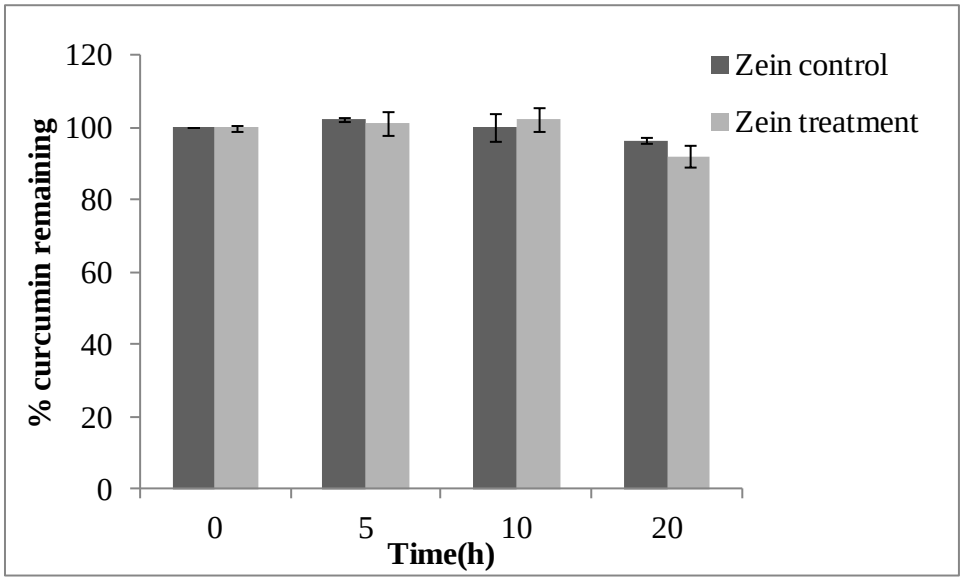
120
100
80
60
40
20
0
% curcumin remaining
0
5
10
20
Time(h)
Zein control
Zein treatment

(b)